The Mass Assembly History of Field Galaxies

Thesis by

Kevin Bundy

In Partial Fulfillment of the Requirements

for the Degree of

Doctor of Philosophy

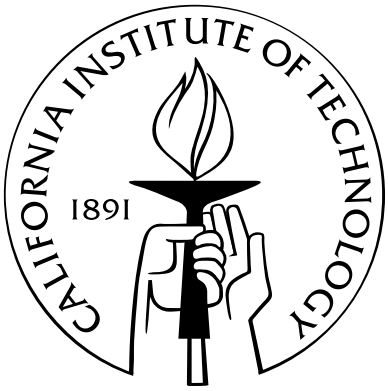

California Institute of Technology

Pasadena, California

2006

(Submitted February 23)

To my grandfather,

who taught me the joy of exploring how things work.

Acknowledgements

Astronomers and jazz musicians share more in common than you might think. Obviously, the late-night hours are similar, as is the pay, and practicing one's scales is probably equal in enjoyment to reducing data (maybe). Most importantly, in both pursuits, the final results owe a lot to one's teachers, fellow performers, and the occasional participation of key audience members.

During my thesis work, I have had the great fortune of learning from one of the masters, a Sonny Rollins of astronomy, if you will. Richard Ellis has inspired me with his mastery of so many topics and the enthusiasm he brings to pursuing them (a typical observing night with Richard has the excitement of running a race and being an air traffic controller, both at the same time). I continue to learn from him, whether we are discussing new scientific ideas, the best ways to implement them, or if anyone ever expects the "Spanish Inquisition."

When it comes to the older "cats" on stage that have taught me the ropes, I want to especially thank Chris Conselice. Chris is well on his way to becoming a Herbie Hancock in the astronomy world and I am grateful for his scientific support and good humor during many long observing runs at Palomar. I will thankfully not have to hear any more of his renditions of the Beach Boy's *Barbara Ann*, but I do hope Chris calls me when he figures out how to put Palomar in space. I would also like to thank Tommaso Treu for his laser-sharp insight and support, Jarle Brinchmann for key advice early on, and Jason Rhodes for help on weighty topics. Masataka Fukugita taught me the value of paying close attention to details and I am thankful for the opportunity I have had to learn from him. I also want to thank James Taylor for very useful if sometimes rounded discussions that, no matter the starting point, always end up at halo models for some reason.

There are many folks backstage that have helped make this work possible. Judy McClain has superhuman multitasking powers and is probably, as many of us suspect, a goddess. Likewise, Patrick Shopbell, a deity in his own right, has often provided computer magic. Among the people at Palomar, I am grateful to Rick Burruss for his knowledge of WIRC and the idiosyncrasies of the 200 inch and to Karl Dunscombe and Jean Mueller who were always kind about having to close the dome for such varied reasons as fog, rain, sleet, snow, wind, and yes, ash. I will also miss the home-cooked meals and juicy gossip served up by Dipali and Rose.

My friends and family in the audience have offered loving support and comic relief, making sure to clap after every solo. I am thankful for friends like Josh, Dave, and Stan and already miss our ritual lunches at Ernie's. Celia and her wonderful music (she's a true musician) carried me through the first years of grad school, and to the Berkeley crew consisting of Shaun, Dave, Robert, and Nate (honorary member), thanks for the "poker" games, for not setting my stuff on fire, and for supporting my Palomar K-band and Keck (PKaK) observations. To Alexie, I am simply thankful to have found you in this world and I love you with all my heart.

Finally, I want to thank the financial and spiritual backers of this work. Frank Gaspar hooked me on astronomy at an early age and took me to Joshua Tree for stargazing that still inspires me. Jack Bishop would usually meet me out there among the galaxies—I am incredibly grateful for his guidance, support, and inspiration on all levels. My immediate family has also been wonderfully supportive. My grandmother was always proud and never failed to ask about my work. The same goes for David, JoAnne, Mike, Ryan, Jason and Danny (Danny's only 5 years old, but recently informed me there were now 10 known planets). And of course, I am grateful for the solid foundation and love provided by my parents. They have always encouraged me in science despite their English-teaching backgrounds and remain my biggest supporters and closest confidants.

Thank you all so much,
Kevin

Abstract

The work presented in this thesis utilizes the combination of near-IR photometry and spectroscopic redshifts to estimate the stellar masses of distant field galaxies in order to characterize their assembly history since $z \sim 1$. The primary data set for this analysis comes from an extensive near-IR survey of DEEP2 Galaxy Redshift Survey fields conducted at the 200 inch Hale Telescope at Palomar Observatory. The resulting sample is the largest to date, covering more than 1.5 square degrees to a median depth of $K_s \approx 20.5$ (Vega) and containing over 12,000 galaxies detected in the K_s-band with spectroscopic redshifts in the range $0.2 < z < 1.5$. A new Bayesian code has been developed to estimate stellar masses for this sample. The code fits observed $BRIK$ colors to an array of models in order to constrain the M_*/L_{K_s} ratio which is then scaled to the measured K_s-band luminosity, providing a mass estimate for each galaxy in the sample that is accurate to a factor of $\sim$2.

Utilizing these estimates, galaxy stellar mass functions were constructed from the survey and analyzed as a function of redshift over the range sampled by the data. Incompleteness in both the K_s-band and R-band was carefully determined and accounted for by considering fainter samples supplemented with photometric redshifts. Appropriate weighting was applied to the mass functions to account for redshift target selection and success rates, and cosmic variance was estimated by comparing results of various subsamples of the full data set. After accounting for these effects, the observed galaxy stellar mass function exhibits little evolution in the mass range probed by the survey ($M_* \gtrsim 10^{10}\mathrm{M}_\odot$). Within the precision set by cosmic variance ($\sim$1.5), the measured abundance of galaxies at a given mass in this range remains constant over the interval $0.4 < z < 1.4$, indicating that the stellar content

of intermediate to high mass galaxies has largely assembled by $z \sim 1$.

Significant evolution since $z \sim 1$ in the make-up and characteristics of the galaxy population does take place, however. This evolution is apparent in the stellar mass functions of specific populations partitioned by restframe $(U-B)$ color, [OII]-derived star formation rate, and morphology. At the highest redshifts probed, the galaxy population is bimodal, with red, passive spheroidals dominating the high-mass end of the mass function and blue, late-type galaxies with ongoing star formation dominating at lower masses. As a function of time, red early-types—already established at the highest masses at $z \sim 1$—increase in abundance as star formation shifts to late-type galaxies with lower masses. This pattern is interpreted in the context of "downsizing" and a new mechanism is proposed that is capable of quenching star formation in massive systems and driving their morphological transformation into systems with spheroidal configurations.

Two new diagnostics are introduced to help quantify this downsizing behavior with a view to providing quantitative measures that will help constrain various proposals for the physical nature of this mechanism. The transition mass, M_{tr}, is defined as that stellar mass at which the abundance of red, early-type galaxies equals that of blue, late-type galaxies. When the population is partitioned by restframe $(U-B)$ color, M_{tr} evolves from $10^{11}\mathrm{M}_{\odot}$ at $z \approx 1.2$ to $3 \times 10^{10}\mathrm{M}_{\odot}$ at $z \approx 0.5$, which is similar to the value measured at $z \approx 0.1$ by SDSS. The behavior of M_{tr} is robust to other ways of partitioning the galaxy population such as [OII] star formation rate and morphological type. The second diagnostic, the quenching mass (M_Q), is a more physically useful measure and traces the stellar mass scale above which star formation in galaxies is suppressed. Like the transition mass, M_Q also decreases by a factor of $\sim$5 over the redshift range of the sample but is measured to have a higher value than M_{tr} by a factor of $\sim$3 and is therefore more robust to effects from incompleteness. The evolution of M_Q indicates that the quenching mechanism responsible for downsizing becomes more efficient in galaxies with lower masses as a function of cosmic time.

To further investigate the nature of this mechanism, the environmental dependence of M_Q is analyzed using the projected 3^{rd}-nearest-neighbor statistic as an estimate of

local density. For the majority of the sample near the median density, no environmental dependence is observed. Only in the most extreme environments—comparable to group scales for this survey—is a weak trend apparent. Here, downsizing appears to be slightly accelerated in the highest density regions as compared to those with the lowest measured density. This weak environmental dependence suggests that for most galaxies the quenching mechanism is primarily driven by internal processes.

A physical explanation for the behavior of the quenching mechanism is presented through a discussion of galaxy formation models based on the ΛCDM hierarchical framework. Additional motivation for this comparison is presented in two ongoing studies. The first is a separate near-IR analysis of galaxy pairs which quantifies the stellar mass accreted in galaxy mergers since $z \sim 1$. It demonstrates that while optical diagnostics may overestimate the merger fraction, the mass assembly rate increases at early times, as predicted in the ΛCDM framework. An extension of this work is planned with the aim of characterizing the mass function of merging systems. The second ongoing study is an investigation of the stellar-to-dark-matter ratios of disk galaxies at $z \sim 1$, which supports the expectation from hierarchical models that baryons and dark matter halos assemble together. Future work with higher quality data will help verify this prediction.

Assuming the ΛCDM scenario is correct, the observations of galaxy evolution presented here support new theoretical work that suggests that quenching is caused by merger-driven AGN feedback. This process appears to be a promising solution to a variety of problems in galaxy formation models and is explored as a possible explanation for the observations of downsizing discussed in this work, although recent semi-analytic models incorporating AGN feedback are still unable to reproduce the evolution of M_Q. The quantitative results presented here will help refine such models. In addition, preliminary tests of the inferred connection between AGN feedback and galaxy evolution are also presented and future observations that can help illuminate the physical details of this feedback mechanism are discussed.

Contents

List of Tables

List of Figures

Chapter 1

Introduction

The history of galaxy evolution is a story that can be told in two ways. The work presented in this thesis contributes to one of these narratives, which begins with the birth of galaxies in the early universe and tells the history of their evolution to the present day. Before describing some key questions still unanswered in this story and how the present work addresses them, it is helpful to consider the second perspective, namely the history of our understanding of galaxies. As an introduction, this historical perspective is valuable for two reasons. First, unlike our current scientific description, the history of the subject—at least to the present day—is much less likely to change. And second, this history illuminates broad patterns of progress that help orient our current picture and provide insight into the future of the subject.

1.1 A Historical Perspective on Galaxy Evolution

Although the modern understanding of galaxy formation and evolution is only about 30 years old, the subject has a history that stretches back several centuries. From the beginning, the subject, like many other scientific pursuits, has found its way forward under the sometimes opposing pressures of theoretical insight and new observations driven by advancing technologies. Arguably, it was theoretical deduction that launched the study of external galaxies about 150 years after Kepler's work on planetary orbits. In 1755, Immanuel Kant, before moving on to problems of a different scale, described a prescient cosmology in *Universal History and Theory of the*

Heavens (Kant orig. 1755), first identifying a model describing the Milky Way as a disk of stars with the sun located in the plane and then making the leap to predicting the existence and appearance of other such systems:

> If a system of fixed stars which are related in their positions to the common plane as we have delineated the Milky Way to be, be so far removed from us that the individual stars of which it consists are no longer sensibly distinguishable even by the telescope ... then this world will appear under a small angle as a patch of space whose figure will be circular if its plane is presented directly to the eye, and elliptical if it is seen from the side or obliquely.[1]

Kant's ideas were supported by William Herschel, often considered the first extra-galactic astronomer because of his visual sky survey and "Book of Sweeps" in which he cataloged thousands of sources with particular interest in so-called "nebulae" that he believed were located beyond the galaxy. Whether these nebulae were the same as Kant's "Island Universes" was not seriously tested until the early 20^{th} century when a number of new observations were originally understood to discount the theory. Catalogs of hundreds of thousands of spiral nebulae demonstrated how their distribution avoided the plane of the Milky Way, which suggested that the nebulae were physically associated with our galaxy. The spiral appearance of many of these nebulae supported the recent work on collapsing clouds of gas by Jeans, and the development of spectroscopy confirmed that many of the nebulae consisted of heated gas in emission. On the other hand, similar measurements showed the spectra of some nebulae like M31 to be star-like, and novae—understood to be associated with exploding stars—were observed in the spiral arms of others (see the review by Smith 1982).

The controversy culminated in the "Great Debate" between Harlow Shapley and Heber Curtis in 1920, with Shapley using his maps of globular cluster Cepheid vari-

[1]We are lucky that Kant wrote on this subject early in his career and before adopting a style that led to such sentences as, "the conception of right does not take into consideration the matter of the matter of the act of will in so far as the end which any one may have in view in willing it is concerned."

ables to argue for a "Big Galaxy" picture of the Milky Way with no need for island universes. Cepheid variables soon solved the problem, but in favor of Curtis, with the detection of Cepheids at extragalactic distances in NGC 6822, as announced by Hubble at the American Astronomical Society meeting in 1925 (see Hubble 1925).

With the establishment of "nebulae" as extragalactic objects, attention focused on using them as tracers of the large-scale mass distribution and evolution of the universe. The goal was to determine which cosmological "world model" correctly described how the universe was expanding. Caught in the flow of this expansion, galaxies could be used to trace its evolution, but early on it was appreciated that variations in the intrinsic luminosity of galaxies would make their utility as distance markers challenging (e.g., Sandage 1961). It was therefore necessary to understand and model the luminosity evolution of galaxies. Aided by newly available computers, Tinsley developed the first detailed models of the stellar populations of galaxies of various types and predicted how they would evolve (e.g., Tinsley 1972). This important tool helped provide an empirically motivated model for understanding observations.

At the same time, rapid theoretical progress, much of it driven by the work of Peebles and Zeldovich in the 1960's, was taking place in reconciling the Big Bang theory with the evolution of structure in the universe and the growth of galaxies. The basic principle was that galaxies formed through the development of initial matter overdensities, imprinted as random fluctuations in the power spectrum after the Big Bang. Press & Schechter (1974) developed a linear formalism for tracking these fluctuations and showed how self-similar mass distributions matching the observed structure among galaxies could be achieved with a hierarchical, "bottom-up" framework. The general behavior of gas collapse, cooling, and dissipation in the peaks of the density distribution was explored in several landmark papers in the late 1970's (e.g., Rees & Ostriker 1977; Silk 1977; White & Rees 1978) that set the foundation for our modern picture of how galaxies form out of the neutral gas in the early universe.

1.1.1 Faint Number Counts and Galaxy Redshift Surveys

In a way reminiscent of the relationship between Kant's prediction of island universes and their eventual confirmation, it has taken 30 years of intense observations and additional theoretical developments for this hierarchical worldview of galaxy formation to gain acceptance. Indeed, through the late 1970's and into the 1980's indisputable evidence for evolution in the galaxy population could not even be firmly established. Butcher & Oemler (1978) showed evidence for a changing number of blue galaxies in distant clusters, but studies of the field population[2] were at first restricted to photographic magnitude number counts (Tyson & Jarvis 1979; Peterson et al. 1979) and spectroscopic surveys limited in both magnitude and redshift (Turner 1980; Gunn 1982; Kirshner et al. 1983; Peterson et al. 1986). Of these two, number counts proved more valuable at the time for probing distant galaxies. The advent of CCDs enabled very deep observations (e.g. $B_J < 25$, Tyson 1988) that confirmed evidence for an excess in the number counts above Tinsley-like models with no evolution (Figure 1.1). Number count studies continued into the early 1990's, with particular interest in K-band counts because of the smaller k-corrections and uncertainties due to dust in this waveband. Early reviews on the topic of number magnitude counts are provided in Koo & Kron (1992) and Ellis (1997).

The results from number counts provided tantalizing evidence for evolution in the galaxy population but were inherently limited because the observed galaxies could not be located in redshift space. The need was clear, and a new era of distant galaxy redshift surveys was launched with the work by Broadhurst et al. (1988). Using the Anglo Australian Telescope equipped with a multi-object, fiber-fed spectrograph, Broadhurst et al. (1988) surveyed 187 galaxies to $b_J < 21.5$. Although they found evidence for an increase in the fraction of blue, star-forming field galaxies with redshift, the observed redshift distribution was consistent with no-evolution models, seemingly

[2]This period also saw other exciting developments in galaxy studies, including observations of clustering and spatial distribution characteristics (Tonry & Davis 1979; Davis & Peebles 1983), continuing efforts to understand galaxies in clusters (e.g., Dressler 1980), and the identification of scaling relations (e.g., Faber & Jackson 1976; Tully & Fisher 1977; Kormendy 1977). The review here will focus, however, on efforts to understand the distant field population.

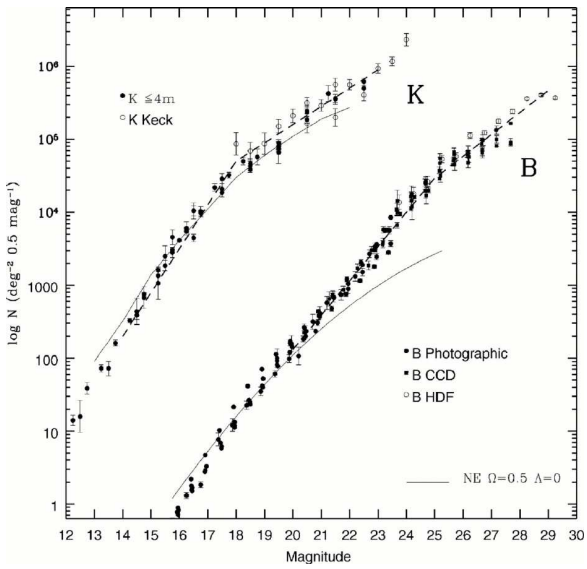

Figure 1.1 A compilation of number magnitude counts in the B and K band from Ellis (1997). The samples come from Metcalfe et al. (1996) and Moustakas et al. (1997). Dashed lines are power-law fits to the data, while the solid lines indicate no-evolution predictions. The K-band counts have been offset by +1 dex for clarity.

in contradiction with expectations from number counts. The same general pattern was also found in Colless et al. (1990), whose Low Dispersion Sky Survey (LDSS) utilized multi-slit spectroscopy to observe 149 galaxies one magnitude fainter than Broadhurst et al. (1988).

Though demonstrating evolution, these first results did not agree with the interpretation of the significant faint excess in the number counts. More ambitious surveys making use of new telescopes and instrumentation soon followed with the hope of addressing the problem. The Canada-France Redshift Survey (Lilly et al. 1995a) measured 730 galaxies to $z \sim 1$, showing strong differential evolution in the luminosity function (Figure 1.2) with a brightening of blue galaxies at $z \gtrsim 0.5$, while the red population was observed to barely evolve (Lilly et al. 1995b). The Autofib Survey (Ellis et al. 1996) obtained 1700 spectroscopic redshifts and showed similar results, including a steepening of the B-band luminosity function with redshift and stronger evolution among galaxies with inferred star formation (based on detected OII emission, Ellis et al. 1996) as well as late spectral type (Heyl et al. 1997). Work in the Hawaii Deep Fields (Cowie et al. 1996) added K-band photometry to 393 spec-

troscopic redshifts, providing the first evidence for a decrease in the typical mass of star-forming galaxies with time—a phenomenon they called "downsizing."

As discussed in the review by Ellis (1997), these first large spectroscopic surveys greatly increased our understanding of the evolving galaxy population and luminosity function out to $z \lesssim 1$, but like earlier redshift surveys (Broadhurst et al. 1988; Colless et al. 1990) still left the puzzle of the excess faint galaxies unsolved. The resolution of this problem came from three developments. First, part of the discrepancy was mitigated by improved local studies of the luminosity function (e.g., Lin et al. 1996; Marzke & da Costa 1997; Bromley et al. 1998; Lin et al. 1999; Cross et al. 2001) that revealed a steeper faint-end slope, implying that less evolution was needed to explain the faint counts (this problem was discussed in Ellis 1997). Second, a non-zero cosmological constant, Λ, became an increasingly popular way of reconciling low values of Ω_b with inflationary constraints that required $\Omega_{tot} = 1$ as well as explaining evidence for accelerated expansion from supernovae type Ia studies (Riess et al. 1998). Fukugita et al. (1990) had shown early on that the larger volumes and ages of cosmological models with $\Lambda > 0$ could more easily accommodate the faint galaxy number counts. Finally, the perception of how galaxies evolve had begun to change. The predominant view had been one in which galaxies form from an early collapse (Eggen et al. 1962) and evolve in isolation (Tinsley 1972), exemplified in this quote on faint galaxy studies from a lecture by Kron (Kron 1993):

> The term "galaxy evolution" is used universally in this context, but "galaxy aging" might better describe the phenomenon we are looking for.

However, by the early 1990's, the hierarchical framework developed by Peebles and its formulation in the Cold Dark Matter (CDM) paradigm (e.g., Blumenthal et al. 1984; Davis et al. 1985; Bardeen et al. 1986) had been incorporated into the first semi-analytic models (White & Frenk 1991) that were capable of matching the observations. The notion that galaxies merge (i.e., violation of number conservation) at relatively late times found increasing acceptance in the community (e.g., Carlberg & Charlot 1992; Carlberg 1992) and helped explain the faint blue excess as the progenitors of

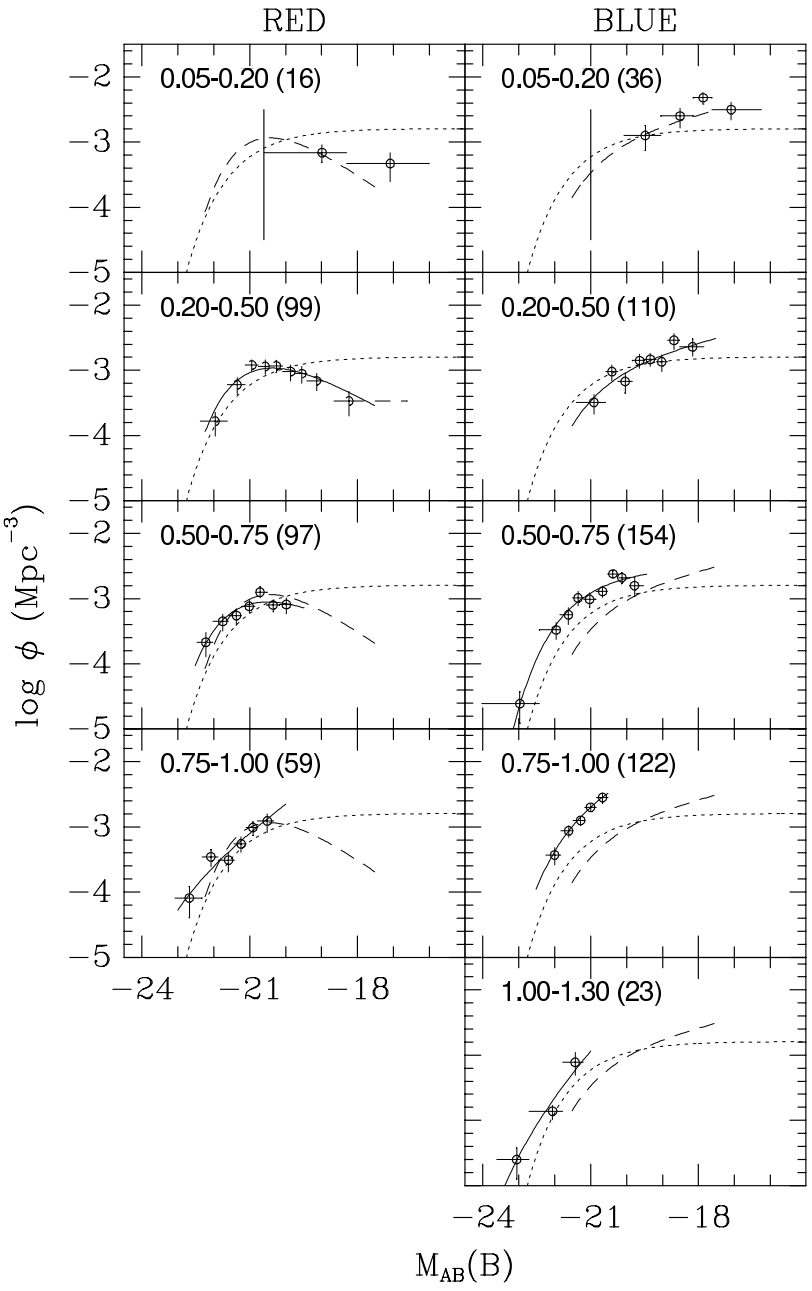

Figure 1.2 Red and blue luminosity functions at different redshifts taken from Lilly et al. (1995a). The "best estimate" luminosity functions are shown. For $z > 0.2$, the solid curve traces a Schechter function fit. The dashed curve reproduces the result obtained for the $0.2 < z < 0.5$ redshift bin, and the dotted line is the local, combined luminosity function from Loveday et al. (1992).

merging systems.

The resolution of the faint blue galaxy problem represents a shift in thinking about galaxy formation. At the very least, it highlights the necessity for accurate $z = 0$ benchmarks such as the luminosity and mass functions to which high-z observations can be compared. It also marks a new era of cosmology defined by a nonzero cosmological constant. But, perhaps most important, it reinforces a dynamic perspective of galaxies, which, in accordance with CDM predictions, emphasizes the role of interactions in shaping the properties of galaxies and the importance of mass assembly as the driving mechanism behind their growth.

1.1.2 The Cosmic Star Formation History

While the spectroscopic surveys of the mid-1990's were exploring the luminosity function of the field population to $z \sim 1$, two new developments helped to outline the evolution of the *global star formation rate* (SFR) to redshifts as high as $z \sim 5$. The first was tracing the evolving luminosity density of the universe and fitting it with models of the integrated luminosity of the star-forming population. With the very deep imaging afforded by Hubble Space Telescope (HST) observations, and especially the Hubble Deep Field (HDF, Williams et al. 1996), as well as the addition of photometric redshifts (e.g., Sawicki et al. 1997), this technique was used to constrain the global SFR to $z \sim 5$ (e.g., Lilly et al. 1996; Madau et al. 1996, 1998). Consistent with interpretations based on the global production of metals (e.g., Pei & Fall 1995), numerous subsequent papers confirmed the general trends found in this work (see Figure 1.3), namely an order of magnitude rise in the SFR with redshift to $z \sim 1$ with a peak at $z \sim 1$–2 followed by an uncertain but apparently moderate decline at higher redshifts (see the review by Hopkins 2004).

The second development, the location and characterization of the star-forming Lyman break population at $z \sim 3$, supported this picture of an enhanced cosmic SFR at early times. Through spectroscopic follow-up conducted at Keck Observatory, Steidel and collaborators not only confirmed the high redshifts of Lyman break

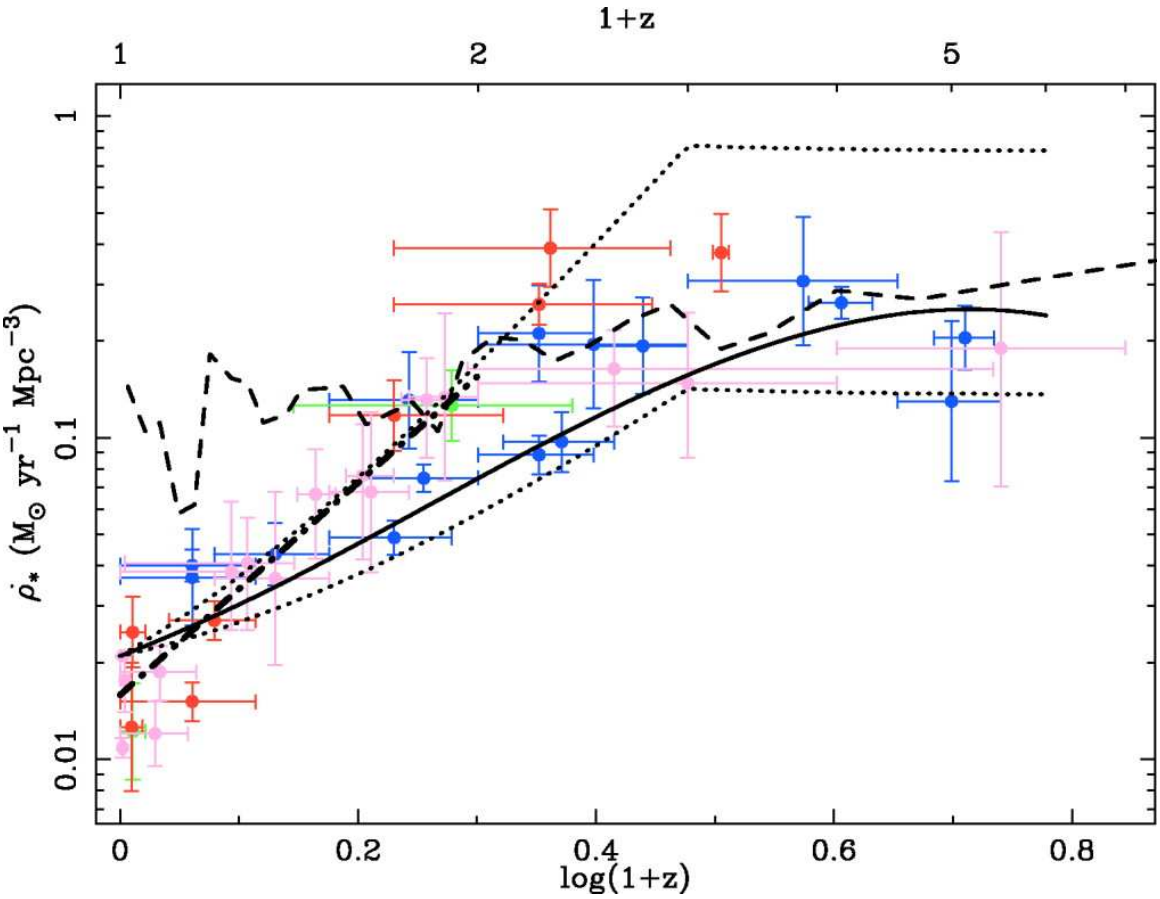

Figure 1.3 A compilation of the global SFR density as measured by numerous authors from Hopkins (2004). The solid curve shows a fit to the data. The dotted curves present models and the dashed line delineates expectations from spectral studies of local galaxies.

galaxies (LBGs) but presented evidence that they were massive systems undergoing significant star formation and were likely to be the progenitors of present-day massive ellipticals (Steidel et al. 1996; Giavalisco et al. 1996). Furthermore, by extending such work to higher redshifts, Steidel et al. (1999) demonstrated that an equally vigorous amount of star formation was exhibited by LBGs even at $z \sim 4$. This established the presence of a high rate of cosmic star formation at very early times, as illustrated in Figure 1.3.

These new constraints on the cosmic star formation history provided a valuable benchmark for models of galaxy formation that incorporated hierarchical merging (e.g., Cole et al. 2000) and "collisional starbursts" (e.g., Somerville et al. 2001) in or-

der to describe the substantial increase in the SFR at early times. At the same time, studies at $z \lesssim 1$ with HST found significant evolution in morphology and evidence for galaxy interactions that supported expectations for the hierarchical framework. Hubble imaging was added to spectroscopic surveys to constrain the luminosity function and number counts of morphological populations (e.g., Driver et al. 1995a,b; Abraham et al. 1996; Brinchmann et al. 1998; Driver et al. 1998) which demonstrated the increasing abundance of star-forming irregular galaxies and a higher incidence of merging (Burkey et al. 1994; Driver et al. 1998; Le Fèvre et al. 2000) at early times. In the context of the global SFR, these observations seemed to be probing the final stages of the active period at $z \sim 2$. They suggested that the decrease in the blue luminosity density—and, hence, the cosmic SFR—was driven by a decline in the merger rate exemplified by the decreasing abundance of irregular star-forming galaxies. Thus, in support of the hierarchical scenario, it appeared that galaxy assembly was responsible for driving evolution and governing the rate of star formation in the universe.

1.1.3 The Era of Galaxy Mass Studies

In recent years, models based on the CDM (or now ΛCDM) framework such as the one described in Cole et al. (2000) have become increasingly successful at reproducing the observed cosmic SFR and luminosity function to $z \sim 1$. But while work on the evolution of galaxy luminosity has continued to the present day (e.g., Cohen 2002; Wolf et al. 2003; Willmer et al. 2005; Faber et al. 2005; Ilbert et al. 2005), the results of such efforts are difficult to interpret in physical terms and do not place strong additional constraints on models of galaxy formation. This limitation of optical galaxy tracers was recognized and described by Brinchmann & Ellis (2000):

> To make progress, we require an independent "accounting variable" capable of tracking the likely assembly and transformation of galaxies during the interval $0 < z < 1$. The color and emission-line characteristics are transient properties and poorly suited for this purpose ... The dynamical

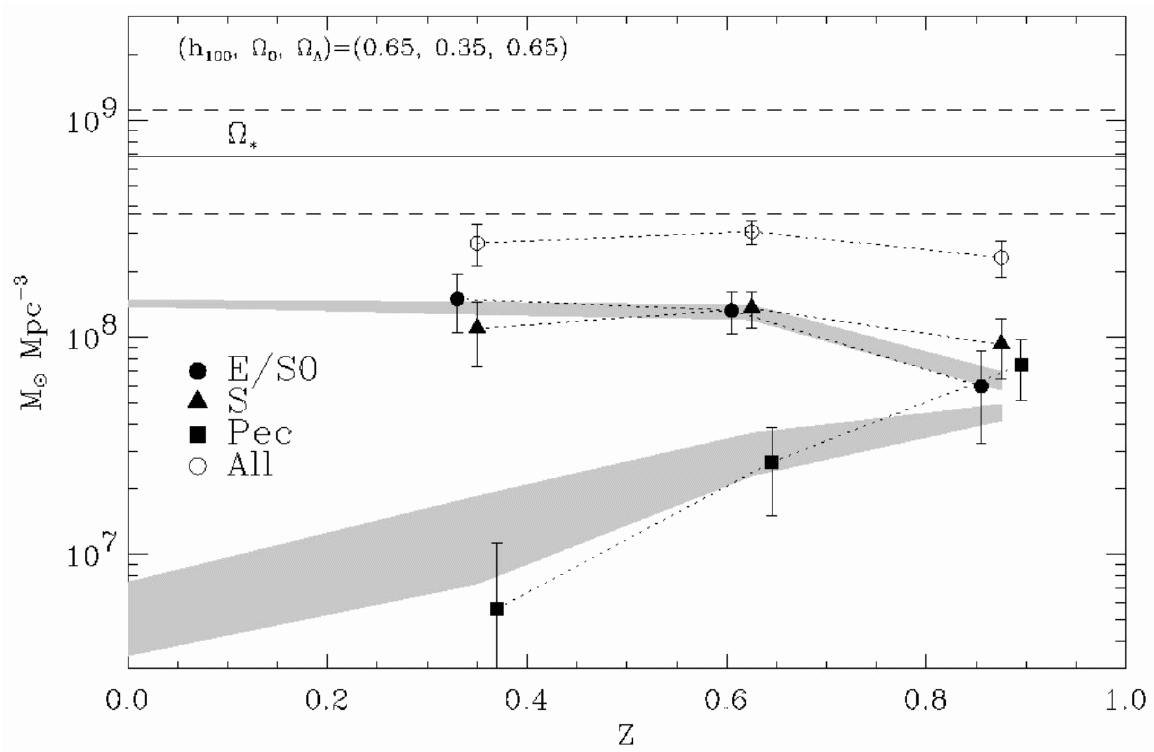

Figure 1.4 The evolution in the global stellar mass density of E/S0's, spirals, and peculiars defined by visual HST morphology (from Brinchmann & Ellis 2000). The shaded regions show predictions from simple merger models.

or stellar mass is the obvious choice.

If reliable galaxy mass estimates can be obtained, it is possible to move beyond luminosity measurements and apply comprehensive tests to the CDM paradigm by comparing the expected hierarchical assembly of dark matter to the observed assembly history of galaxy mass.

Brinchmann & Ellis (2000) employed a novel technique that utilizes K-band photometry to estimate the stellar masses of galaxies (this tool is a critical aspect of the work presented in this thesis and is described in detail in Chapter 2). In this way, they were able to probe the mass assembly of morphological populations, demonstrating how the global mass density of late-type galaxies has declined since $z \sim 1$, while that of spheroidals has grown (Figure 1.4)—a process suggestive of transformation between the two populations.

Arguably, this important result marks the beginning of a new approach to the subject that benefits from investigating the mass-dependent evolution and assembly of galaxies. While modern studies of high-z dynamical masses (e.g., Böhm et al. 2004; Treu et al. 2005b) and gravitational lens galaxies (Bolton et al. 2005) are coming online, the promise of this approach is also a large part of the motivation for ground-based near-infrared (near-IR) surveys, many of which are further described in Chapter 2 (e.g., Saracco et al. 1997, 1999; McCracken et al. 2000; Huang et al. 2001; Drory et al. 2001; Chen et al. 2002; Cimatti et al. 2002; Fontana et al. 2003; Abraham et al. 2004), as well as stellar masses derived from Spitzer Space Telescope observations at $z > 1$ (e.g., Shapley et al. 2005; Papovich et al. 2005).

1.2 The Mass Assembly History of Field Galaxies

As described in the previous section, the end of the last decade saw an enormous increase in our knowledge about galaxy evolution with an accompanying shift toward a merger-driven ΛCDM framework as a means of interpreting observations. While successful in a variety of ways, many unanswered questions remain in our understanding.

- When do galaxies of a given mass assemble their stellar content? Does the rate of assembly agree with ΛCDM predictions?
- What causes the significant decline in the global SFR?
- How important is merging in the assembly of galaxies and what role does it play in their evolution?
- What causes the bimodality in the galaxy distribution? How are properties such as color, star formation rate, morphology, and mass related? How do they evolve with time?

The work presented in the chapters that follow addresses these questions through an investigation of the stellar masses of distant galaxies. Ideally, it would be possible

to characterize the assembly of galaxies beginning at very high redshifts and indeed significant progress has occurred in this area (e.g., Juneau et al. 2005; Reddy et al. 2005; Shapley et al. 2005; Papovich et al. 2005; Chapman et al. 2005; van Dokkum et al. 2006). In this thesis, however, I will concentrate on the interval $0 < z \lesssim 1.5$, which, although it may not include the most active epochs of galaxy formation, is accessible to new spectroscopic and near-IR instruments that enable detailed, multi-wavelength studies of statistically complete samples covering a large dynamic range in mass. The primary goal is a detailed account of the mass assembly history of galaxies over this redshift interval. A plan of the thesis follows.

1.2.1 The Infrared Survey at Palomar: Observations and Methods for Determining Stellar Mass

Brinchmann & Ellis (2000) showed the power of combining K-band photometry, optical imaging, and spectroscopic redshifts in surveys of evolving populations. Further progress required much larger samples so that the broad patterns in the global stellar mass density (e.g., Cowie et al. 1996; Brinchmann & Ellis 2000; Cohen 2002) could be broken down and studied in terms of the galaxy mass function. As described in Chapter 2, this was the inspiration for an extensive near-IR campaign I undertook at Palomar Observatory. After 65 nights over nearly three years, I present an unprecedented sample of over 12,000 galaxies with spectroscopic redshifts ($0.2 < z < 1.5$) from the DEEP2 Galaxy Redshift Survey (Davis et al. 2003) and Palomar K_s-band photometry down to $K_s \approx 20.5$ (Vega).

Chapter 2 also describes the method I developed for utilizing near-IR plus optical photometry to estimate the stellar masses of galaxies. This key tool figures prominently in all of the work presented in this thesis.

1.2.2 The Mass Assembly History of Morphological Populations

The impact of HST observations on the study of galaxy morphology and evolution was discussed in §1.1.2. These studies demonstrated how the Hubble Sequence, which provides a reliable rubric for classifying the morphology of galaxies at $z = 0$, begins to break down at $z \gtrsim 1$ (e.g., Conselice et al. 2004). The increased SFR at these epochs suggests a link to morphology that is further supported by the higher frequency of bright, blue late-type galaxies at early times. In addition, Brinchmann & Ellis (2000) showed evidence for the possible transformation of late-types into spheroidal systems based on the evolving stellar mass density of these populations. While theoretical expectations suggested that merging can lead to spheroidal configurations (e.g., Barnes & Hernquist 1991), details on the nature of this transformation were not known.

Chapter 3 presents a study (Bundy et al. 2005a) utilizing observations in the GOODS fields from HST, Palomar, and Keck observatories to address these issues. By charting the galaxy stellar mass function of ellipticals, spirals, and irregular galaxies out to $z \sim 1$, we extended the work of Brinchmann & Ellis (2000) and showed that ellipticals dominate at the highest masses even at early times, indicative of an early formation time for the most massive galaxies. Below a stellar mass of $2\text{–}3\times10^{10}\mathrm{M}_{\odot}$, the galaxy population becomes dominated by late-type systems. This transition mass is not only very similar to the bimodal division as traced by various parameters in the $z = 0$ population (e.g., Kauffmann et al. 2003b), but also appears to be higher at $z \sim 1$. This, combined with our observation of very little evolution in the total mass function, suggests that the mechanism driving morphological evolution operates on a mass scale that shifts downward with time, a phenomenon we refer to as morphological downsizing.

1.2.3 Downsizing and the Mass Limit of Star-Forming Galaxies

Following the work just described (Bundy et al. 2005a), Chapter 4 presents a comprehensive study of the mass-dependent evolution of field galaxies utilizing the large Palomar/DEEP2 sample detailed in Chapter 2. Representing the culmination of the work presented in this thesis, the primary aim of this study was to characterize the assembly of galaxies through an analysis of the evolving stellar mass functions of well-defined populations.

As mentioned previously, many groups have measured the significant decline in the global SFR since $z \sim 1$ (Hopkins 2004), but the nature of this decline is not well understood. The early work by Cowie et al. (1996) provided some insight by revealing a phenomenon called downsizing, in which the mass scale of star-forming galaxies moves from high mass systems at $z \sim 1$ to lower mass galaxies with cosmic time. However, the detailed nature of the process and the physical mechanism responsible for driving it remained unclear. The key question was whether downsizing resulted from external environmental effects (perhaps associated with accelerated evolution in overdense regions) or was caused by an internal process within the galaxy.

The previously mentioned work (Chapter 3) suggested that tracing the stellar mass that divides the bimodal galaxy population, M_{tr}, could provide a powerful way of quantifying the downsizing signal and investigating its nature. The combined survey of Palomar near-IR imaging and DEEP2 redshifts offers the best data set available for this experiment. Chapter 4 describes my analysis of this data set and the evolution of M_{tr} revealed in the galaxy stellar mass function partitioned by restframe color as well as [OII] SFR. These observations strongly suggest that an internal physical mechanism is responsible for quenching star formation in massive galaxies, driving downsizing, and bringing about the decline in the global SFR. The most likely candidate, merger-driven AGN feedback, and hopes of constraining how this process works with future observations are discussed in the conclusions presented in Chapter 7.

1.2.4 A Direct Study of the Role of Merging

The hierarchical framework in which galaxies form in dark matter halos and grow by merging with galaxies hosted in other halos was introduced in §1.1. This theoretical picture underlies the most advanced semi-analytic (e.g., Cole et al. 2000; Somerville et al. 2001; Croton et al. 2005; Bower et al. 2005) and numerical (e.g., Nagamine et al. 2004; Springel et al. 2005c) models of galaxy formation today, successfully reproducing a number of observations including the total stellar mass function, clustering properties, and the bimodality of galaxies. As discussed previously, late-time ($z \lesssim 1$) merging is one of the key drivers of evolution in this framework. Not only is it the means by which galaxies assemble, it is also implicated in the morphological transformation (e.g., Barnes & Hernquist 1991; Springel et al. 2005a) discussed in Chapter 3 as well as the quenching of star formation (e.g., De Lucia et al. 2005; Hopkins et al. 2005a) described in Chapter 4.

Directly testing and quantifying the role of merging in galaxy evolution remains a challenging endeavor, however. The problem is, first, how to identify an active merger and, second, determining the timescale on which the merger proceeds. There are generally two approaches, and both involve significant uncertainties. First, utilizing HST one can search for disturbed morphologies suggestive of ongoing interactions (e.g., Driver et al. 1998; Le Fèvre et al. 2000; Conselice et al. 2003; Lotz et al. 2006). This technique suffers from contamination from non-merging but still irregular systems, uncertainties in how long the disturbed morphology lasts, and the inability to distinguish major from minor mergers. The second approach is to count pairs of nearby galaxies that are assumed to be on the verge of merging (e.g., Patton et al. 1997, 2000; Le Fèvre et al. 2000; Lin et al. 2004). Here, contamination from foreground and background sources and, again, uncertainties in the merger timescale pose significant challenges.

On top of these hurdles, previous studies of the merger rate have relied on optical diagnostics to probe what is inherently a mass assembly process. In Chapter 5 I discuss work on the first attempt to constrain the merger rate in terms of stellar

mass, allowing this important process to be understood in the context of the mass-dependent studies presented in Chapters 3 and 4. As reported in Bundy et al. (2004), this work demonstrates a bias toward higher merger rates in optical observations compared to the infrared and presents the first estimate of the stellar mass accretion rate due to merging since $z \sim 1$. Extensions of this work are underway and described in Chapter 7.

1.2.5 Relating Stellar Mass to Dark Matter through Disk Rotation Curves

The work introduced in the previous sections exploits near-IR stellar mass estimates to investigate how galaxies assemble and evolve over the interval $0 < z < 1.5$. Stellar mass studies are valuable not only because they provide a census of the stars generated by the global SFR (see Dickinson et al. 2003) but also because they offer a proxy for the total mass of a galaxy. It is therefore critical to verify and test the limits of this relationship between stellar mass and total mass. Clarifying this link also provides a way of probing the behavior of dark matter, which, under the assumption that it interacts only through gravity, is more easily understood theoretically compared to the complex hydrodynamic processes that take place in the luminous component of galaxies.

Chapter 6 presents work on one of the first attempts to establish the connection between stellar and dark matter in the context of field galaxy studies. Using a sample of spiral galaxies with redshifts out to $z = 1.2$, total masses inferred from Keck rotation curves were compared to stellar mass estimates gleaned from K-band photometry. The work presented here is reported by Chris Conselice in Conselice et al. (2005). My role in the project was assembling the various disparate observations taken on numerous telescopes over several years, providing the analysis of stellar masses and the Tully-Fisher relations, and examining our results in terms of specific models of disk formation (van den Bosch 2002).

Our initial results in this program show a clear trend between stellar mass and

total halo mass in this sample with no detected evolution out to $z \sim 1$, although our observations involve significant uncertainties. We present the first measurement of the high-z stellar mass Tully-Fisher relation, relating stellar mass to maximum rotational velocity, V_{max}, and show how the observations are consistent with the hierarchical assembly of galaxies in which the mass in baryons and dark matter grows together. Considering the limitations in the way the sample was selected and the spectroscopic data quality, we have begun a much more ambitious project using DEIMOS in the GOODS fields to obtain 8–10 hour rotation curves for a carefully selected sample of $\sim$120 disk galaxies. This project is described in more detail in Chapter 7.

Chapter 2

The Infrared Survey at Palomar: Observations and Methods for Determining Stellar Masses

In this chapter I describe an extensive infrared imaging survey I conducted at Palomar Observatory that serves as the core observational component of my thesis. I discuss the strategy adopted in this survey, its relationship to the DEEP2 Galaxy Redshift Survey, and the observations as well as photometric analysis. This chapter also provides details on the method I developed for utilizing infrared observations to estimate the stellar mass of galaxies. This crucial tool is used in all of the work presented in this thesis.

2.1 Motivation for the Survey

Over 15 years ago, the advent of new infrared detectors on large telescopes provided the opportunity to conduct the first galaxy surveys that took advantage of the small k-corrections (e.g., Kauffmann & Charlot 1998) and relatively low dust extinction in the near-IR. Because of the small detector area of infrared detectors available at the time, these surveys were either very shallow, reaching $K \lesssim 13$–17 over 0.2–2 deg^2 (e.g., Glazebrook et al. 1991; Mobasher et al. 1993; Glazebrook et al. 1994), or deep but narrow, reaching $K \lesssim 21$–24 over $\sim$100 arcmin^2 (e.g., Gardner et al. 1993; Cowie et al. 1994; Djorgovski et al. 1995; McLeod et al. 1995; Saracco et al. 1997). Early

science results focused on using K-band number counts to help constrain cosmological parameters (e.g., Djorgovski et al. 1995) and unravel key aspects of galaxy evolution (e.g., Broadhurst et al. 1992).

As it became increasingly possible to combine infrared observations with spectroscopic redshifts and multi-band optical photometry (e.g., Cowie et al. 1996), the utility of near-IR luminosities as a stellar mass estimator became apparent (Kauffmann & Charlot 1998; Brinchmann & Ellis 2000). Compared to dynamical mass estimates—which can be derived from spectroscopy for only certain types of galaxies (e.g., Vogt et al. 1996; Jorgensen et al. 1996)—infrared mass estimates are a less expensive proxy (in terms of telescope time) for galaxy mass and can be more easily measured for entire samples, regardless of type.

Both narrow and wide-field infrared studies began exploiting this capability. The work by Dickinson et al. (2003) perhaps represents the culmination of near-IR pencil-beam studies. Using stellar mass estimates based primarily on deep HST/NICMOS imaging in the Hubble Deep Field–North (HDF–N) region (only 5.0 arcmin^2), Dickinson et al. (2003) were able to characterize the evolution in the global stellar mass density over $0 < z < 3$ for the first time. In the case of wide-area near-IR surveys capable of producing statistical samples at $z \lesssim 1$, it has only recently been possible to improve significantly upon work such as that by Brinchmann & Ellis (2000). They used a sample of 321 field galaxies imaged in the K-band and the optical with HST (WFPC2) to show how, since $z \sim 1$, the global mass density of various morphological populations evolves. Examining this global evolution as a function of mass, i.e. measuring the evolving galaxy stellar mass function, requires larger samples, however.

By 2002, when the Palomar survey began, there were two key efforts just finishing that were motivated in large part by charting the galaxy stellar mass function. The Munich Near-Infrared Cluster Survey (MUNICS, Drory et al. 2001) began on the Omega-Prime instrument (6.75×6.75 arcmin^2) at the 3.5m Calar Alto Telescope in 1996. The final MUNICS sample contains 5000 galaxies spread over $\approx$1 deg^2 to a depth of $K \lesssim 18.7$ (Vega). It consists of primarily ($\approx$90%) photometric redshifts. Complimentary to MUNICS, the K20 Survey (Cimatti et al. 2002), which began in

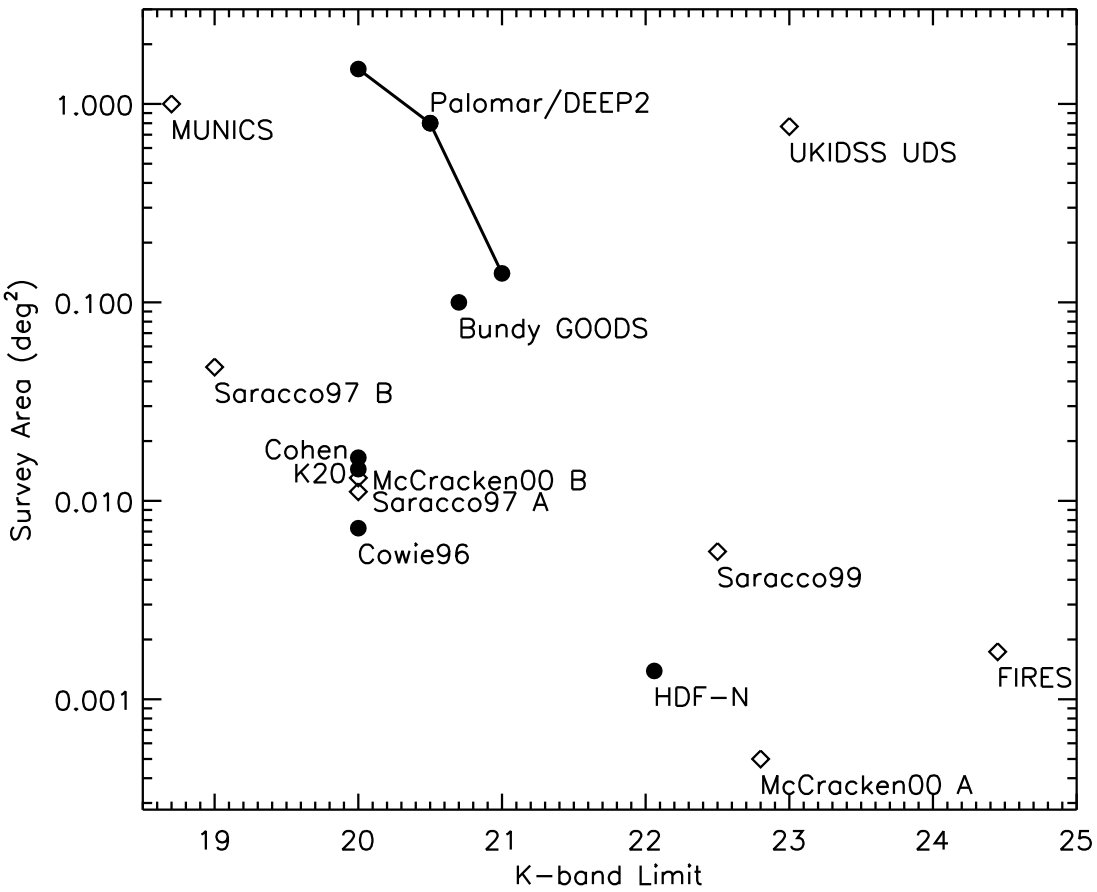

Figure 2.1 Comparison of the depth and coverage of a number of near-IR surveys. Filled symbols denote surveys with significant spectroscopic follow-up: *Palomar/DEEP2* shows the three nested surveys described in this chapter (§2.2.2); *Bundy GOODS* refers to Chapter 3 and Bundy et al. (2005a); *Cohen* refers to the Caltech Faint Galaxy Redshift Survey (see Hogg et al. 2000; Cohen 2002); *K20* is presented in Cimatti et al. (2002); *Cowie96* is the Hawaii Deep Field work (Cowie et al. 1996); and *HDF* refers to the work by Papovich et al. (2001) and Dickinson et al. (2003). Open symbols represent surveys without spectroscopic follow-up: *MUNICS* refers to the survey presented in Drory et al. (2001); *UKIDSS UDS* is the deepest component of the UKIRT Infrared Deep Sky Survey, which finished K-band imaging in late 2005; *Saracco97 A* and *B* are subsamples of the ESO K'-band Survey (Saracco et al. 1997); *McCracken00 A* and *B* are subsamples of the work discussed in McCracken et al. (2000); and *FIRES* is the Faint IR Extragalactic Survey (Labbé et al. 2003). It should be noted that the UKIDSS Deep Extragalactic Survey (DES, their "medium" depth effort) is 36% complete (as of February 2006) in its K-band imaging goal of $K = 21$ over 35 deg^2—this part of parameter space is literally "off the chart" on the figure above.

1999 on the ESO VLT, has surveyed about 550 galaxies—most (92%) with spectroscopic redshifts—down to $K < 20$ over an area of 52 arcmin^2.

While the MUNICS and K20 programs represent significant progress in wide near-IR surveys and led to many results (e.g., Fontana et al. 2004; Drory et al. 2004a), each suffers from important limitations. MUNICS is too shallow to reliably probe below the characteristic mass, M^*, at $z \sim 1$, and its reliance on photometric redshifts introduces significant uncertainties in stellar mass estimates (see §2.4). The K20 Survey, on the other hand, suffers from substantial random errors and cosmic variance because of its small size, preventing detailed studies of sub-populations within the primary sample and reducing the statistical significance of the results. The infrared survey at Palomar was designed to address these limitations.

The primary goals of the survey were to fully characterize the evolving stellar mass function and chart the assembly history of the galaxy population as a function of various physical parameters. These goals set clear specifications for the survey. To mitigate cosmic variance, for example, the surveyed area had to be at least 1.0 deg^2. Furthermore, building a statistically complete sample that would be robust to various cuts and sensitive to evolutionary trends required ∼10,000 galaxies with spectroscopic redshifts out to $z \sim 1$. Finally, to probe the mass function below M^*, we set a target depth of $K = 20$ (Vega), with a good fraction of the sample aimed at $K \gtrsim 21$ to detect even fainter galaxies and test for incompleteness. A comparison of the depth and area covered by the Palomar survey to a selection of other near-IR surveys is made in Figure 2.1.

The Wide Field Infrared Camera (WIRC, Wilson et al. 2003), successfully commissioned on the 5m Hale Telescope at Palomar Observatory in 2002, provided the large field of view (8.6×8.6 arcmin^2) and sensitivity needed for achieving these goals. At the same time, the DEEP2 Galaxy Redshift Survey (Davis et al. 2003) had begun its second year, delivering what would be an unprecedented spectroscopic sample at $z \sim 1$—the perfect data set for subsequent follow-up imaging with WIRC. After several nights of testing in late 2002, we began our infrared campaign as a Palomar "Large Program" in 2003a and completed it two and a half years later.

Table 2.1. Survey Field Characteristics

Field	RA	Dec	Dimensions	IR Coverage	K_s Sources
EGS (Field 1)	14:16:00	+52:00:00	$16' \times 1.5°$	100%	45066
Field 2	16:52:00	+34:00:00	$0.5° \times 2.25°$	27%	13523
Field 3	23:00:00	+00:00:00	$0.5° \times 2.25°$	33%	18377
Field 4	02:30:00	+00:00:00	$0.5° \times 2.25°$	33%	19411

2.2 Survey Design

2.2.1 Field Layout

The layout and much of the strategy behind the Palomar survey was shaped by the nature and progress of the DEEP2 Galaxy Redshift Survey (Davis et al. 2003). More details about the DEEP2 sample and its contribution to the major scientific results of this thesis are presented in Chapter 4, but I present some of the key features of DEEP2 here.

The DEEP2 survey is comprised of four independent regions covering a total area of more than 3 square degrees. The properties of the four fields are summarized in Table 2.1. The DEEP2 redshift targets were selected based on BRI colors determined from observations with the CFHT 12k camera, which has a field of view of $0.^{\circ}70 \times 0.^{\circ}47$ (see Coil et al. 2004). DEEP2 Fields 2–4 are composed of three contiguous CFHT pointings, oriented from east-to-west. The Extended Groth Strip (EGS, also known as Field 1) has a different geometry, encompassing and extending the original Groth Strip Survey (Groth et al. 1994) to a swath of sky $16'$ wide by $1.^{\circ}5$ long and oriented at a $\sim 45°$ position angle. This geometry required four tiered CFHT pointings because the 12k camera cannot be rotated.

With the four target fields defined in this way, the DEEP2 team concentrated first on observing the central CFHT pointing in Fields 2–4. In the EGS, DEEP2 observations began at the southern end of the field and progressed upward. For all four fields, we coordinated the Palomar K_s-band observations to track the progress of

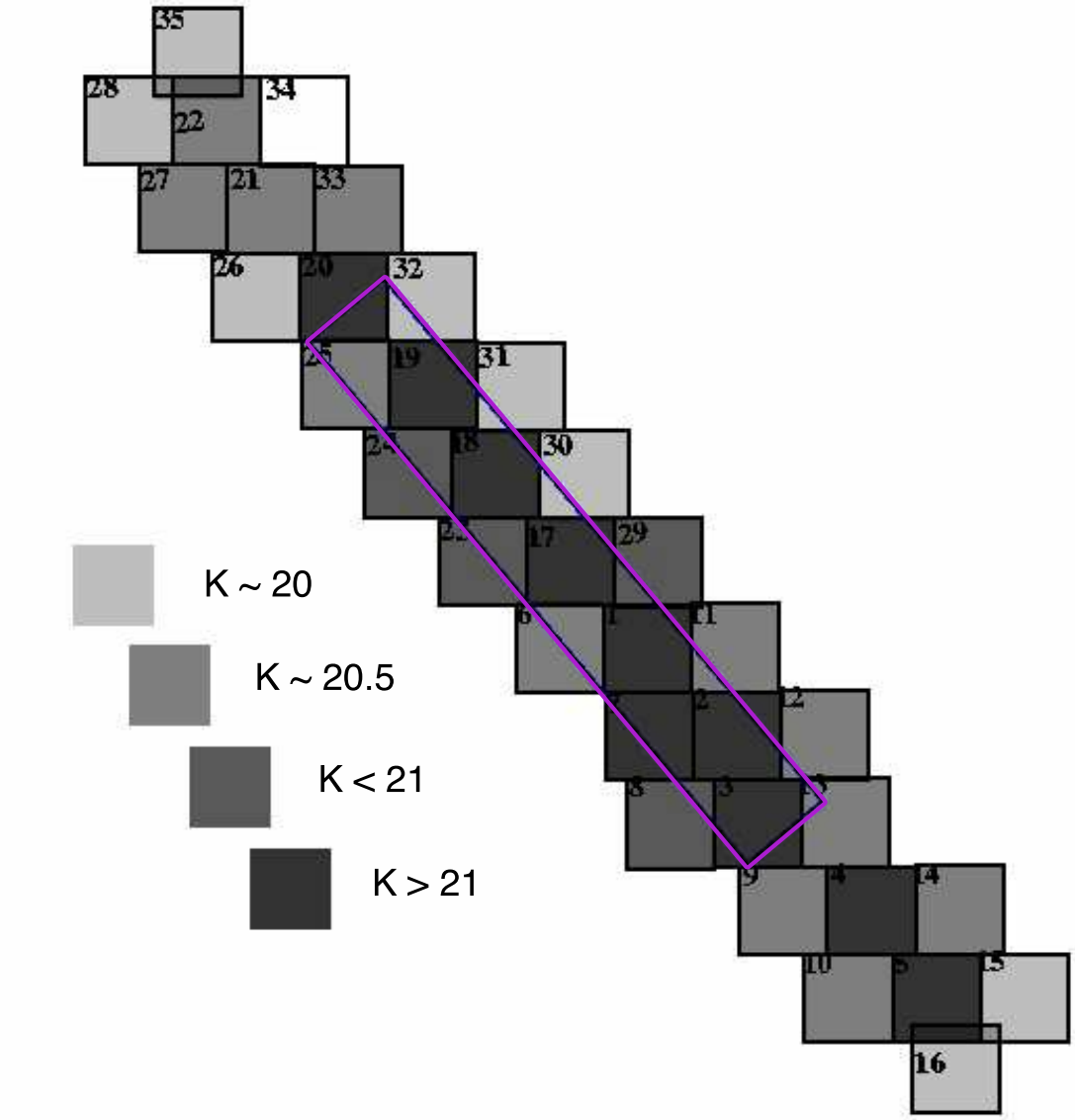

Figure 2.2 WIRC pointing layout and K_s-band depth in the EGS. The region imaged by HST/ACS is indicated by the central rectangle.

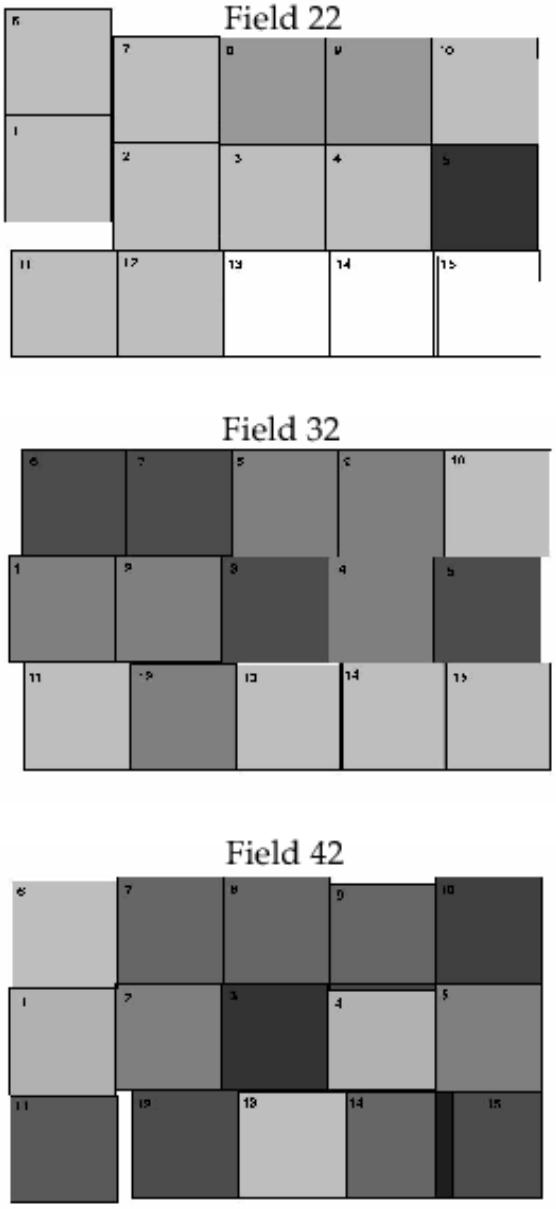

Figure 2.3 WIRC pointing layout and K_s-band depth in Fields 2–4. The shading depth is the same as in Figure 2.2.

DEEP2. Palomar K_s-band coverage is complete in the central third of Fields 3 and 4. In Field 2, 80% of the central CFHT pointing was surveyed and the coverage in the EGS is 100%. The EGS was considered the highest priority field in view of the many ancillary observations—including HST, Spitzer, and X-ray imaging—obtained there. The final Palomar Survey covers 1.6 square degrees, with Fields 2–4 accounting for 0.9 square degrees, and the EGS accounting for 0.7. Coverage maps for each of the four regions are shown in Figures 2.2 and 2.3.

2.2.2 Depth of K_s-band Coverage

A tiered approach was adopted to maximize the depth and coverage of the survey while addressing the typical weather patterns at Palomar. A base target depth of $K_s = 20.0$ (Vega or 21.8 in AB magnitudes) was used for all pointings. At $z \sim 1$, a galaxy with $K_s = 20$ roughly corresponds to a stellar mass of 10^{10} $M_\odot$, which is about one order of magnitude less than the characteristic mass, M^*. The $K_s = 20$ limit was also chosen because it is achievable in 1–2 hours of integration time in average to mediocre conditions (determined mainly from the seeing FWHM which is $\approx 1''$ in the K_s-band in average Palomar conditions). When conditions were superior, with seeing of $0\farcs6$–$0\farcs9$ (this occurred only about $\sim$15% of the time, unfortunately), we concentrated on select fields with the goal of reaching $K_s = 21$ (Vega), enabling detections of galaxies with stellar masses of $\approx 5 \times 10^9$ $M_\odot$ at $z \sim 1$. The magnitude depth quoted here is defined as the 5σ detection limit in an aperture with a diameter equal to the seeing FWHM. Tests showed this depth estimate to be comparable to the 80% completeness limit determined from Monte Carlo simulations using inserted fake sources (see 2.3.1).

This strategy effectively combines several surveys of different depths into one (see the "Palomar/DEEP2" data points in Figure 2.1). Our shallowest component covers 1.5 square degrees to $K_s > 20.0$. This was the base goal for the depth in all of the observations. Nested within this area is a deeper component covering 0.8 square degrees to $K_s > 20.5$. And within this component, 0.14 square degrees reach $K_s > 21$

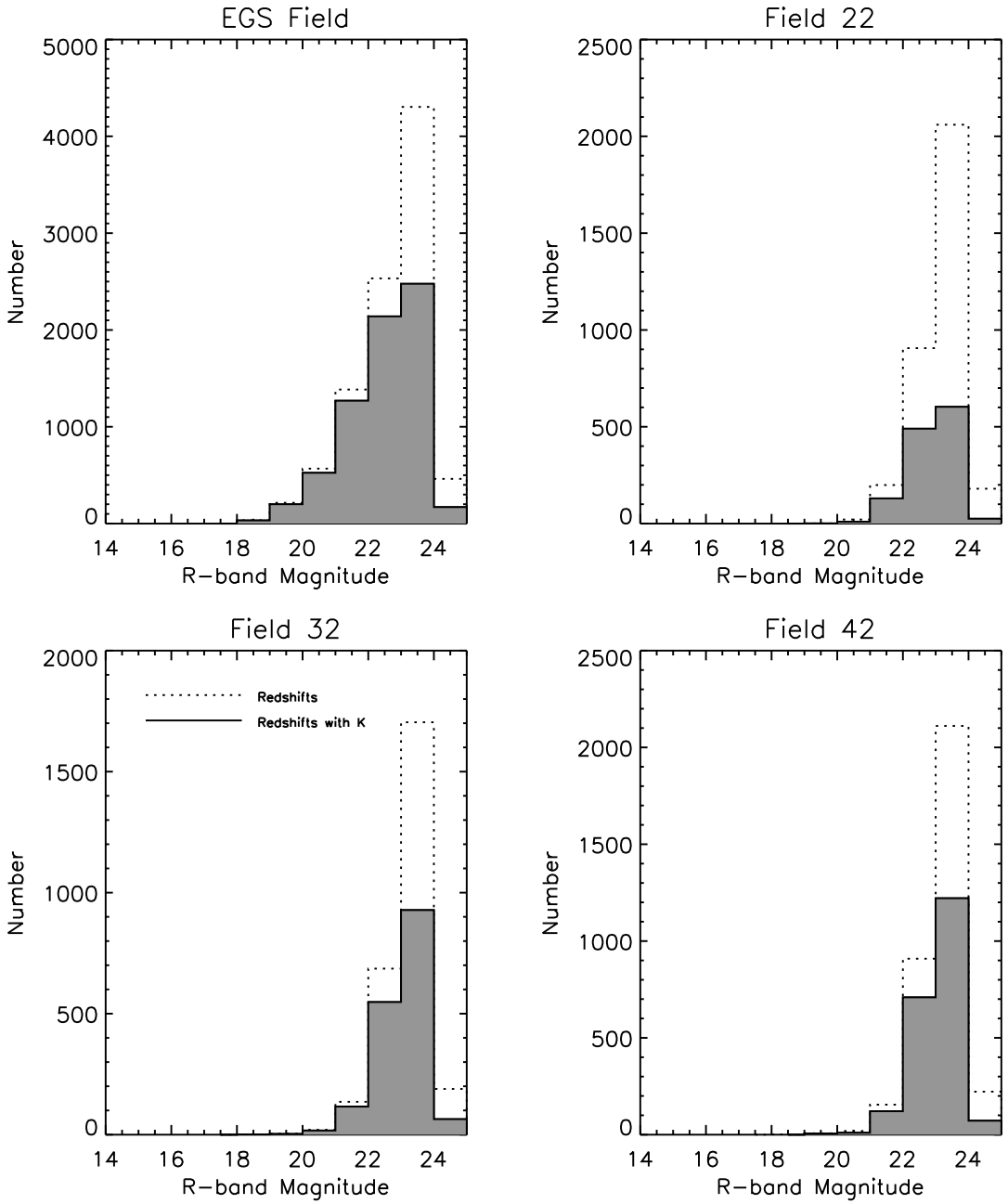

Figure 2.4 This figure illustrates the redshift detection rate in each of the four fields. The dotted histograms show the R_{AB} number counts for galaxies with successful DEEP2 redshifts. The shaded histogram illustrates the fraction of these galaxies that have K_s-band detections. The EGS field is clearly the deepest in terms of detected DEEP2 sources.

(most of the deepest pointings are in the central portion of the EGS). This tiered approach enables one to generate comparable samples across a broad redshift range by constructing redshift intervals that balance the size of the cosmic volume sampled with the stellar mass limit probed (see 4.2.3).

The depth of the observations also determines the fraction of DEEP2 redshift galaxies that are detected in the K_s-band. This fraction ranges from ≈65% for K_s-band depths near $K_s = 20$ to ≈90% for $K_s = 21$. The K_s-band depth and redshift detection rate for each field are illustrated in Figure 2.4.

2.2.3 Mapping Strategy

The field-of-view of WIRC is $8\farcm7 \times 8\farcm7$, and it has a fixed orientation on the sky with its y-axis aligned North–South. In each of the four fields in the survey, WIRC target pointings were chosen to cover the full extent of DEEP2 redshift sources and were tiled to minimize the overlap between adjacent WIRC pointings. The advantage of this kind of tiling pattern—as opposed to one with overlap between images—is that it maximizes the area covered. The down side is that each pointing has to be photo-calibrated independently, leading to the possibility of slight zeropoint offsets from one pointing to the next. However, because of the relatively low number density of bright K-band sources, self-calibration between overlapping pointings would require shared regions that are at least 25% of the WIRC field of view, significantly reducing the total survey area. In addition, it is difficult in practice to make sure that each set of exposures, taken at a given pointing over different nights, is perfectly aligned with previous observations at the same position. This is due to occasional pointing problems on the 200 inch Hale Telescope as well as glitches in the dither script, both of which can lead to spatial offsets of tens of arcseconds, making the alignment of adjacent mosaics more difficult.

The tiling patterns are straightforward in the case of Fields 2–4 because these rectangular areas are also aligned along the N–S/E–W axes (see Figure 2.3). The long and narrow EGS region is tilted at a ∼45° position angle. To fully cover the spectroscopic

observations in the E–W direction required rows of three WIRC pointings. The N–S direction required about 12 different positions, so, in total, 35 WIRC pointings were used to map the EGS in the K_s-band (Figure 2.2). Roughly two-thirds of the WIRC pointings in the EGS contain regions of sky without DEEP2 spectroscopic targets. These perimeter pointings were given less priority than the central WIRC positions for this reason, so the deepest EGS exposures ($K_s \gtrsim 21$) were taken in positions along the center of the EGS. In addition, there is, in general, better K_s-band data in the southern portion of EGS because DEEP2 redshifts were first acquired there (as of the completion of this work, the northern 20% of the EGS DEEP2 observations were not complete). Finally, deep K_s-band imaging was extended northward to include the region of the EGS covered by HST/ACS observations in 2004 (see Figure 2.2).

The mapping mode on a given night was chosen based on the observing conditions. In excellent conditions, the exposure time at a given WIRC position could add up to several hours. In average conditions, 1–2 hours was spent integrating at a given position before moving on to the next pointing. The choice of which WIRC pointing in a given field to expose on was determined by the data already available in that field as well as the conditions at the time so that each new observation would provide the maximum scientific return for the survey.

With most of the shallow ($K_s \gtrsim 20$) component of the survey completed, J-band observations were obtained in the case of average conditions during the last year of the survey. In Fields 3 and 4, J-band imaging to $J \lesssim 22$ (Vega) was obtained for 80% and 100% of each field, respectively. No J-band data was taken in Field 2, and in the EGS we carried out deep J-band imaging ($J \lesssim 23$) along the central 9 WIRC pointings. These positions were chosen because they are coincident with the deepest K_s-band data and overlap with the HST/ACS region. The same WIRC positions and tiling patterns used in the K_s-band were also used in the J-band.

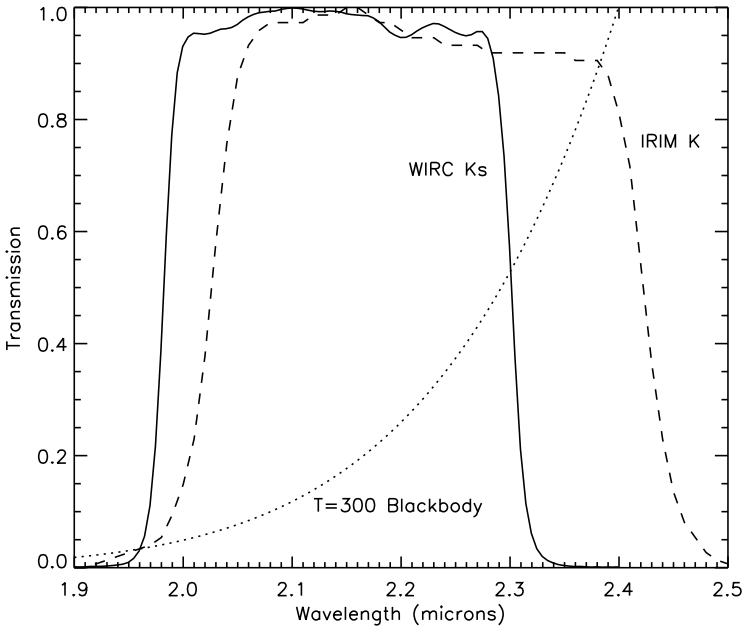

Figure 2.5 The WIRC K_s filter response (solid line) compared the Kitt Peak IRIM K-band filter (dashed line) and a normalized blackbody spectrum at $T = 300$ K (dotted line).

2.3 Observations and Data Reduction

Near-IR observations from the ground are background-limited due to the thermal radiation from the atmosphere.[1] The K_s filter is designed with a sharper red cut-off compared to the K filter to help limit the background contribution (see Figure 2.5), but with sky background levels of K_s ∼13 mag/arcsec^2 (typical for Palomar Observatory), short integrations are required to prevent detector saturation. For WIRC's 2048 × 2048 Hawaii-II HgCdTe detector (additional details on the detector are provided in Table 2.2), our tests confirmed that the response became nonlinear at ∼25,000 adu. This restricts K_s-band integration times to 20 seconds in conditions with $T \sim 20$°C, 30 seconds with $T \sim 10$°C, and 40 seconds with $T \sim 0$°C. Before and after each exposure, 3.25 seconds are required to read out the array, so choosing the longest exposure time allowed by the conditions helps increase the efficiency of

[1]Wein's Law gives $\lambda_{peak} \sim 10\mu$m for a blackbody at $T = 300$ K, roughly the temperature of the atmosphere.

Table 2.2. WIRC Characteristics

Hawaii-II HgCdTe Detector	
Position on 200 inch	Prime Focus, f/3.3
Field of view	8.7 arcmin^2
Pixels	2048 × 2048, 0.2487″/pixel
Gain	5.467 e$^-$/adu
Dark Current	∼0.26 e$^-$/s
Read Noise	< 15 e$^-$

observations.

Sky background levels in the near-IR vary on scales of several minutes (K. Matthews, priv. communication). To remove these fluctuations, individual K_s-band exposures at a given WIRC pointing and dither position were taken with an integration time of 2 minutes before moving to the next dither position. By changing the number of coadds per position—6 coadds × 20 seconds ($T \sim 20$°C), 4 coadds × 30 seconds ($T \sim 10$°C), or 3 coadds × 40 seconds ($T \sim 0$°C)—the 2 minute integration time was maintained under all conditions, making it easier to stack images taken on different nights. The vast majority of observations were obtained in the 4 × 30 second mode.

In all observations, 2 minute exposures were dithered over a 3 × 3 grid (Figure 2.6). The grid point spacing was chosen to be 7″ to insure accurate photometry for target galaxies as large as ∼3″ while minimizing the slew time between dither positions. Because adjacent exposures contribute significantly to the flat fielding of a given frame (see below), the sequence for slewing to each point in the grid was chosen to maximize the dithered offset between frames (the sequence is numbered in Figure 2.6). This 9-point sequence was typically repeated 3 times at a given pointing so that the full dither pattern contained 27 positions and a total integration time of 54 minutes. A random spatial offset, typically ∼1.″5, was applied to each of the 27 positions. This prevented direct overlap in the 54-minute observation set and improved the final image quality. The main sources of overhead were reading out the detector and slewing to the next dither position. With the most common set-up of

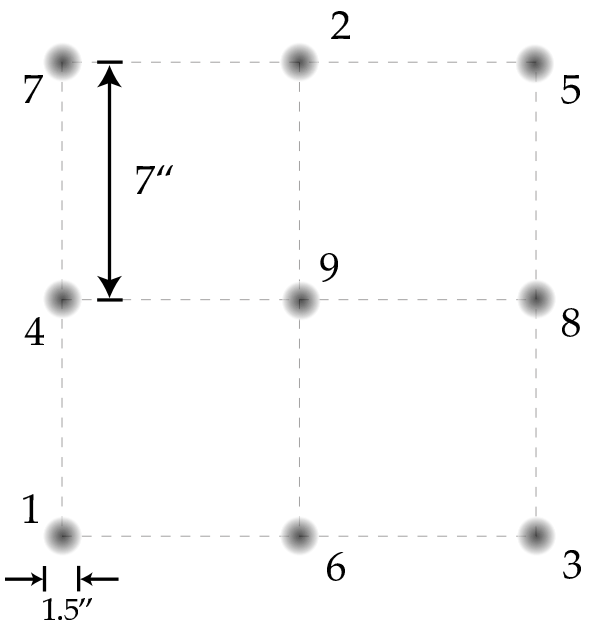

Figure 2.6 The 3 × 3 dither pattern used in the WIRC observations. The numbers indicate the order in which the pattern was executed. A random spatial offset of ∼1.″5 was applied at each position.

4 × 30 sec exposures, a full set of 27 frames and 54 minutes on sky corresponds to about 70 minutes of clock time, giving an efficiency of 77%.

Camera control and data taking were carried out using a dual-processor "Linux box." A second, identical machine was purchased in early 2003 as a back-up and was also configured to "grab" incoming raw data and store it on a separate hard drive, independent from the control computer. Most data reduction and analysis was performed on this second machine to help prevent crashes of the control computer. It was possible, however, to examine subtracted "first-look" images on the data-taking machine, as this process does not require significant computation. As illustrated in Figure 2.7, the dominant sky background and flat-field pattern which obscures most astronomical sources in raw K_s-band frames can be removed simply by subtracting two images from an observing sequence. With the background removed and sources now visible, the result can be easily inspected to determine the seeing and focus accuracy by measuring the profile shape of stars in the field of view. Based on such measurements, it was often possible to adjust the focus "on the fly" without significant interruption to the observing sequence.

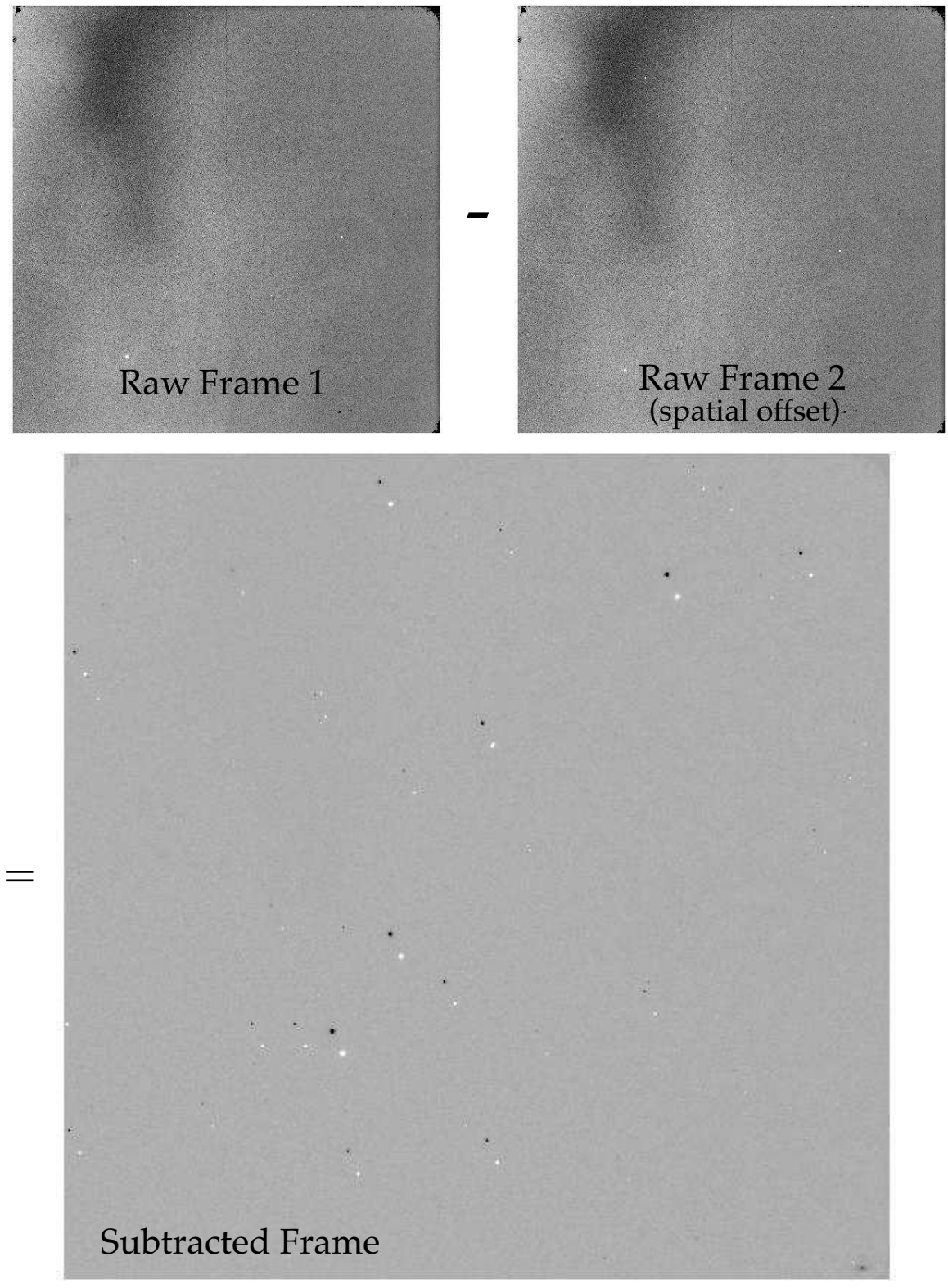

Figure 2.7 Example of subtracting two raw WIRC frames to obtain a "first look" image. The two raw images shown at the top are part of a set of 4×30 second observations taken on October 20, 2005 in average conditions with seeing FWHM of $1\farcs1$. The dominant background and flat-field pattern common to both images is apparent and obscures all but the brightest astronomical sources in the raw frames. Pairs of positive and negative sources are easily seen in the subtracted frame, however. Their separation of $\sim 7''$ reflects the dither offset between the two frames.

In addition to generating first-look subtracted frames, a full data reduction pipeline I developed specifically for WIRC could be run on the secondary computer while observations were being taken. Despite the relatively large file sizes (each coadded WIRC exposure is ∼16 MB), a set of 27 exposures (54 minutes on sky) could be fully reduced in just over 20 minutes, allowing for near real-time inspection of the final image quality and observing conditions.

The image reduction pipeline first creates a "running sky flat" for a given science frame by (median) averaging together 3 adjacent frames taken before and 3 taken after the science frame (see Figure 2.8). Each science frame is then divided by its corresponding sky flat, which tracks the detector sensitivity and illumination pattern of the telescope during the course of the observations. Experimentation showed that neither dome flats nor twilight flats provide an adequate flat field for WIRC, presumably because of different illumination patterns and stray light. Variations in the night sky background (due to clouds, as an extreme example) also affect the illumination pattern. This means that sky flats created at one time of night are not suitable for reducing data taken later that night, let alone data taken on different observing runs.

With each science frame divided by a median sky flat, stars and galaxies are easily detected. By cross-correlating the science frames, the spatial offset between them in pixels can be determined. The telescope pointing position (which is stored in the image header) is used as an initial guess for these offsets, but is not accurate enough to align the science frames. At this point in the reduction pipeline, an object mask is made based on the location of bright sources in the first frame. Knowing the spatial offsets between each frame, this mask is applied to the creation of new sky flats in which objects on adjacent frames are masked out before these frames are averaged together (Figure 2.8). This provides significantly cleaner sky-flat fields and improves the final, coadded image quality. After this second pass of improved flat fielding, the science frames are aligned and stacked into the final mosaic. In practice, the pipeline works with sets of 12 frames at a time to prevent the memory requirements on the processing computer from becoming unmanageable.

The pipeline was tested extensively and functions without need for human inter-

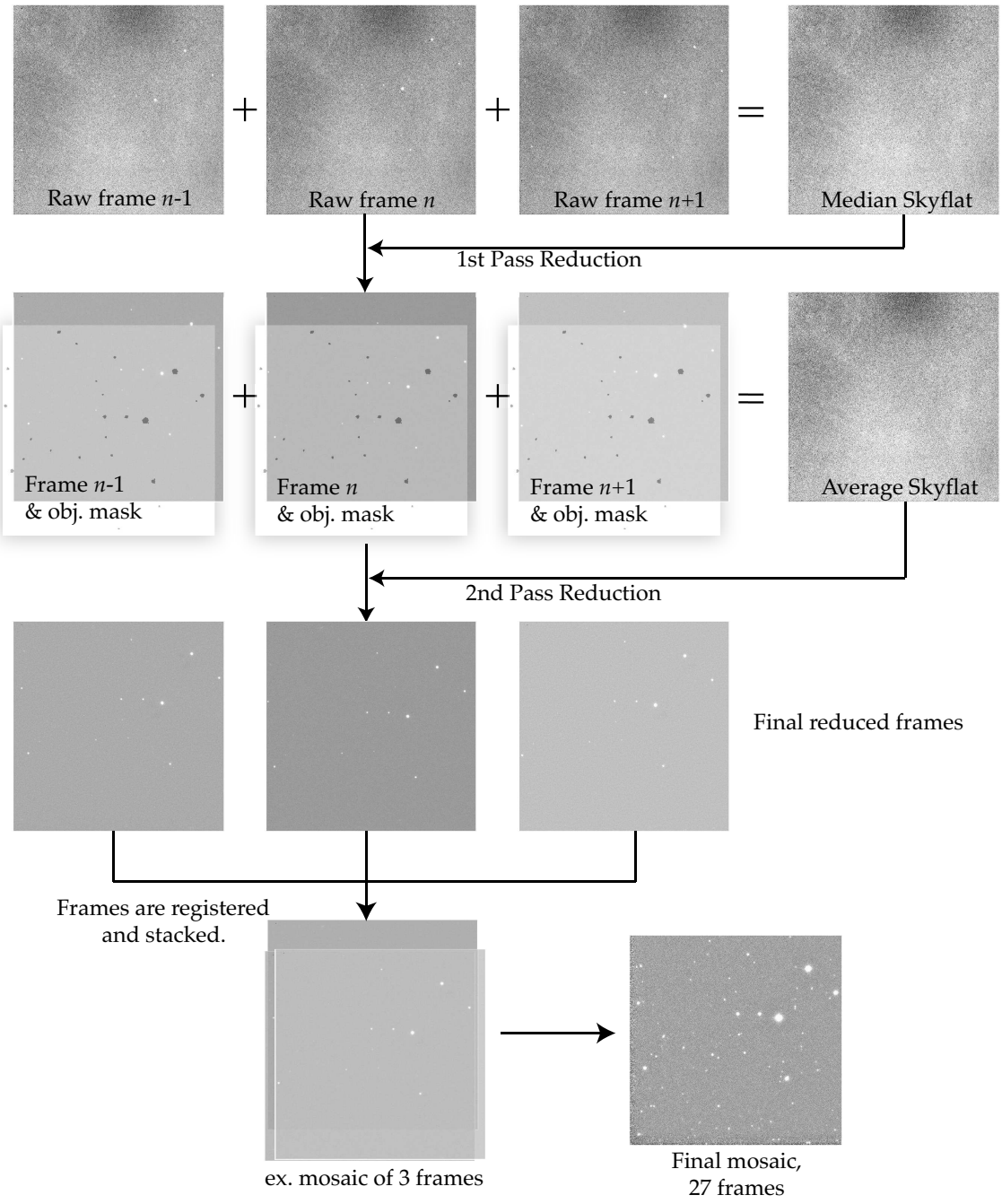

Figure 2.8 Schematic diagram outlining the steps in the double-pass WIRC reduction pipeline. For illustration purposes, the frames shown above are from the SE quadrant of the detector and only 3 frames are shown, whereas in practice, sky flats are created from 6 frames.

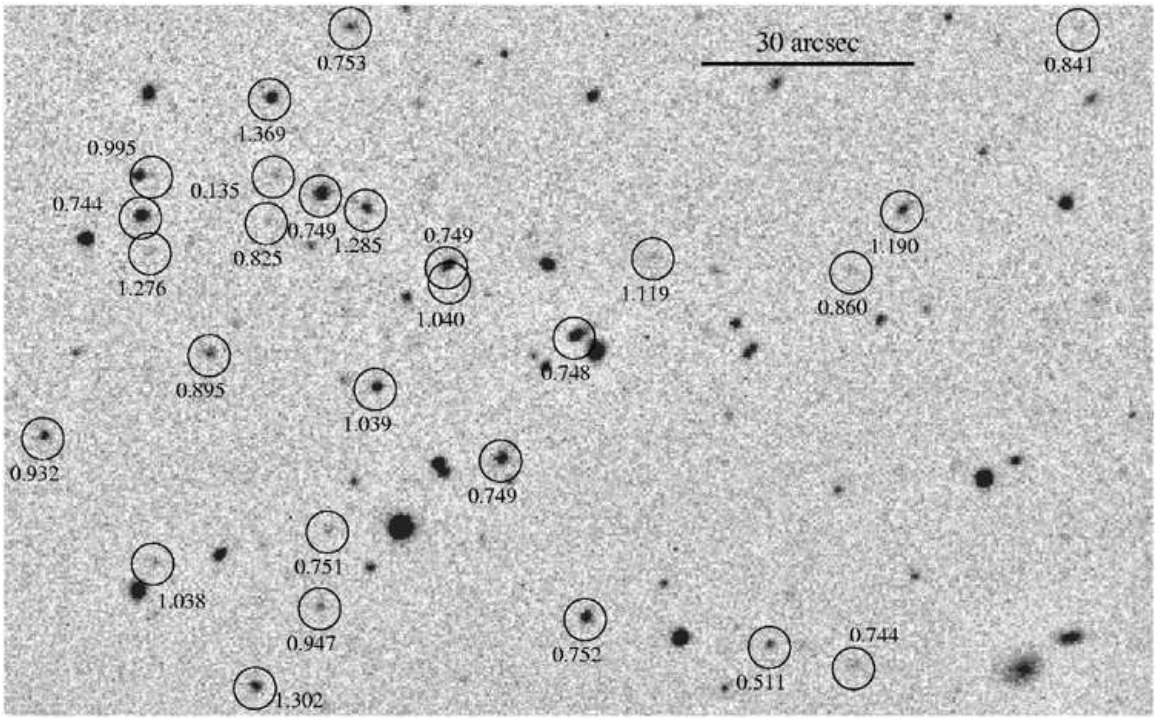

Figure 2.9 An example of the image quality obtained from a deep ($K_s \approx 21$, Vega) mosaic in Field 4 with DEEP2 sources circled and redshifts indicated.

action about 90% of the time when observing conditions are good. One common problem it does not address is the occasional satellite trail across an image frame. I found that these trails, even in one image, will propagate into the final mosaic and so I simply removed frames with satellite trails from the reduction set. When there are clouds present, flat fielding becomes problematic and the cross-correlation routine can fail. In these cases, the pipeline will ask for help in choosing the correct alignment. It can also be executed in a more interactive mode in which the user can use the mouse to select common objects in each frame, the positions of which are then used to align the observations and make the final mosaic. The reduction pipeline was made publicly available and has been used by other WIRC observers.

At a given pointing, individual 54-minute mosaics were often obtained on different nights and so may vary in terms of seeing, sky background levels, and transparency. Most K_s-band pointings consist of more than two independently combined mosaics, with the deepest pointings comprising as many as 6 independent mosaics. Mosaic coaddition was performed using an algorithm that optimizes the depth of the final

image by applying weights based on the seeing, background, and transparency of the constituent mosaics. Following Labbé et al. (2003), the weight of mosaic i is given by

$$w_i \propto (\mathrm{scale}_i \times \mathrm{var}_i \times s_i^2)^{-1}, \tag{2.1}$$

where scale_i is the flux scale factor and accounts for transparency, var_i is the variance, and s_i is the seeing FWHM. The final seeing FWHM in the K_s-band data ranges from $0\farcs8$ to $1\farcs2$ and is typically $1\farcs0$. An example of the data quality in a final K_s-band mosaic is shown in Figure 2.9.

2.3.1 Photometry and Catalogs

Photometric calibration was carried out separately in each field by observing Persson near-IR standards (Persson et al. 1998) and taking short, 5-minute calibration images at each WIRC position during photometric conditions. These short integrations are sufficient for detecting objects at $K_s \lesssim 18$, and the number density of strongly detected sources (about 10 with $12 < K_s < 16$ per image) enables zeropoint calibration for the final mosaics that is typically good to 0.02 mags. This is superior to calibrating with 2MASS, which has a brighter detection limit, leading to fewer sources in common with the final WIRC images and zeropoint uncertainties of $\sim$0.06 mags (and sometimes more). The use of 2MASS is also complicated by the fact that bright stars ($K_s \lesssim 12$) often saturate in the WIRC frames and cannot be used for photometric calibration. I note that the DEEP2 CFHT B and I photometry is calibrated with respect to the CFHT R-band by comparing to the stellar locus in color-color space (Coil et al. 2004). A similar technique could in theory work for the K-band, but the WIRC field-of-view does not contain enough stars (for fields at high galactic latitude) to sample the stellar locus sufficiently. This technique will be possible in the future with larger format near-IR cameras.

The final WIRC mosaics were registered to the DEEP2 astrometric system (see Coil et al. 2004) using bright stars from the CFHT R-selected catalog. The typical root mean square (rms) variation in the astrometric solutions was $0.1''$. In the EGS,

WIRC images were also registered to the 2MASS astrometry to allow for comparisons to Spitzer Space Telescope IRAC data, which uses the 2MASS system. Each of the final K_s-band mosaics were inspected visually, and a mask was made to exclude the low signal-to-noise perimeter that results from stacking dithered images. Only $\sim$8% of the area in the final mosaic was typically masked out.

With the final K_s-band images prepared in this way, we used SExtractor (Bertin & Arnouts 1996) to detect and measure K_s-band sources. In addition to the total magnitude (for which we use the MAG_AUTO output—we do not adjust this Kron-like magnitude to account for missing light in extended sources), we also measured aperture photometry in $2''$, $3''$, $4''$, and $5''$ diameters (later experimentation with SED modeling and color-color diagrams indicated that the $2''$ diameter aperture colors were the most precise). We combined the resulting SExtractor catalog output for each K_s-band image in a given field to create K-selected catalogs.

To determine the corresponding magnitudes of K_s-band sources in the CFHT BRI and Palomar J-band images, we applied the IDL photometry procedure, APER, placing apertures with the same set of diameters at sky positions determined by the K_s-band detections. About 25% of the K_s-band sources do not have optical counterparts in the CFHT optical data. Source pairs from overlapping images with measured separations less than $1\farcs0$ were considered duplicates, and the source with the poorer signal-to-noise was removed from the final catalog.

Photometric errors and the K_s-band detection limit of each image were estimated by randomly inserting fake sources of known magnitude into each K_s-band image and recovering them with the same detection parameters used for real objects. The inserted objects were given Gaussian profiles with a FWHM of $1\farcs3$ to approximate the shape of slightly extended, distant galaxies. We define the detection limit as the magnitude at which more than 80% of the simulated sources are detected. Robust photometric errors based on simulations involving thousands of fake sources were also determined for the BRI and J-band data. These errors are used to determine the uncertainty of the stellar masses and in the determination of photometric redshifts, where required.

For each of the four fields, FITS table catalogs were made that include information on each K-detected source in that field. This includes the $BRIJK$ photometry, estimated magnitude uncertainties, positions, the corresponding K_s-band image depth, DEEP2 spectroscopic redshifts (where available), photometric redshifts (see §4.2.4), and stellar mass estimates (described below). These catalogs have been made available to the DEEP2 team which has used them extensively, and they will become publicly available as the DEEP2 survey is released to the public, beginning in 2007.

2.4 Estimating Stellar Mass

One of the primary motivations for the Palomar near-IR survey was the ability to use K_s-band observations combined with spectroscopic redshifts to estimate the stellar mass of survey galaxies. Because K-band stellar M_*/L ratios are relatively insensitive to the detailed makeup of stellar populations, K-band luminosities alone provide stellar mass estimates that are uncertain by factors of 5–7 (Brinchmann 1999). However, for samples with known spectroscopic redshifts, optical-infrared color information can further constrain the stellar population and M_*/L ratio so as to reduce this uncertainty to a factor of 2–3. The basic technique relies on accurate luminosity distances from spectroscopic redshifts to determine the near-IR (K-band) luminosity of sample galaxies. With a M_*/L_K constrained by comparisons of the galaxy SED to model expectations, the luminosity can be multiplied by the mass-to-light ratio to derive an estimate for the stellar mass ($L_K \times M_*/L_K = M_*$) with relatively high precision. Building on the precepts discussed in Brinchmann & Ellis (2000) and Kauffmann et al. (2003a), I have developed my own Bayesian code for estimating stellar mass and describe it below.

The code uses spectroscopic redshifts and multi-band optical through near-IR colors (typically $BRIK$) to compare the observed SED of a sample galaxy to a grid of 13440 synthetic SEDs compiled from the stellar population synthesis package developed by Bruzual & Charlot (2003). The templates in this grid represent the assumed priors in this Bayesian technique and span 4 dimensions in parameter space: star for-

mation history (τ), age, metallicity, and dust content. The star formation histories are parametrized as exponentials (SFR $\propto e^{-\frac{t}{\tau}}$), with 35 τ values selected randomly from a linear range between 0.01 and 1 Gyr:

τ (Gyr) = [0.04, 0.14, 0.40, 0.54, 0.60, 0.70, 0.71, 0.87, 0.92, 0.93, 1.39, 1.62, 1.75, 1.75, 1.87, 1.99, 2.14, 2.63, 2.74, 3.06, 3.19, 4.08, 4.12, 4.79, 5.26, 5.50, 6.09, 6.28, 6.98, 7.71, 7.88, 7.96, 8.17, 8.89, 9.10].

The age dimension consists of 16 steps selected randomly from a linear range between 0 and 10 Gyr:

t (Gyr) = [0.67, 0.98, 1.28, 2.74, 4.36, 5.06, 5.16, 6.15, 6.46, 6.75, 6.98, 7.97, 8.71, 9.10, 9.53, 9.70].

The metallicity dimension consists of 6 values:

Z = [0.0001, 0.0004, 0.004, 0.008, 0.02 ($Z_\odot$), 0.05].

Finally, the dust content is parametrized by varying $\hat{\tau}_V$, the total effective V-band optical depth affecting stars younger than 10^7 yr, while setting the fraction of this extinction contributed by the ambient ISM to $\mu = 0.3$ (see Bruzual & Charlot 2003). The values of $\hat{\tau}_V$ are

$\hat{\tau}_V$ = [0.0, 0.5, 1, 2].

The values of the parameters listed above were chosen with the goal of fully sampling the possible range of observations. Comparisons between observed galaxy colors and model colors verified that the model space defined above is representative, although the degree to which it reflects real galaxies is an inherent limitation in this technique. Finally, it is important that the sampling of model parameters be random. Systematic biases can be introduced in the results by assuming the values of priors are spaced in a certain way (Sivia 1996).

A unique template spectrum is stored at each grid point and is then compared to the observed galaxy's SED after applying the appropriate redshift and transmission

functions for each filter band. The probability that the specified model at each grid point accurately describes the observed SED is given by

$$P \propto \exp\left(\frac{-\chi^2}{2}\right) \quad \text{with} \quad \chi^2 = \sum_i^{N-1} \frac{\left[(m_i - m_{i+1})_{model} - (m_i - m_{i+1})_{obs}\right]^2}{\sigma_i^2 + \sigma_{i+1}^2}, \qquad (2.2)$$

where i ranges over the observed filters and m_i is the measured magnitude in filter i. In this way, χ^2 effectively measures how well the colors of the template spectrum match the colors of the observed galaxy, modulo the photometric uncertainty (σ_i). This relative probability is calculated at each point in the grid, giving a multi-dimensional probability "cloud" whose size, shape, and position reflects the range of models that best fit the observations, given their uncertainty.

In addition to the relative probability, the corresponding M_*/L_K ratio of each model in the grid is also tracked and converted into a stellar mass by scaling the total K_s-band luminosity of each model (roughly equal to $L_{K\odot}$ for the Bruzual & Charlot (2003) models) to the galaxy's observed L_K. The probabilities are then summed (marginalized) across the grid, renormalized, and binned by model stellar mass. This gives a stellar mass probability distribution for each sample galaxy. We use the median of the distribution as the best estimate. Several examples taken from Bundy et al. (2005a) are shown in Figure 2.10.

The stellar mass measured in this way is robust to degeneracies in the model, such as those between age and metallicity. Although these degeneracies can produce bimodal probability distributions (see Figure 2.10), even in these cases, the typical width of the distribution gives uncertainties from the model fitting alone of 0.1–0.2 dex. For about 2–3% of the SED fits, the minimum χ^2 values are significantly greater than 1.0. For these more poorly-constrained objects, we add an additional 0.2 dex in quadrature to the final mass uncertainty. Although in principle the best fitting model also provides estimates of the age, metallicity, star formation history, and dust content of a sample galaxy, these quantities are much more affected by degeneracies and are poorly constrained compared to the stellar mass.

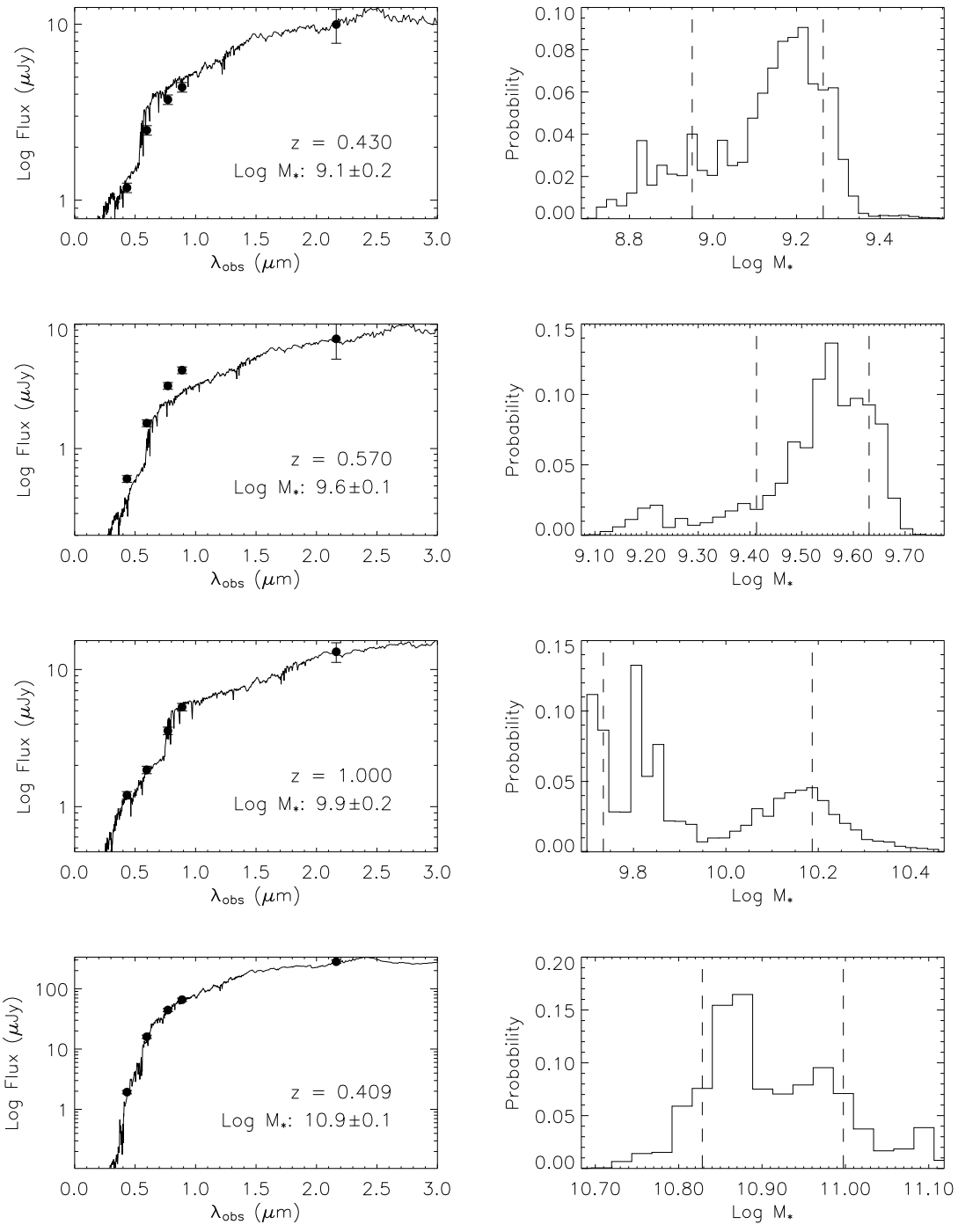

Figure 2.10 Examples of the best-fitting model spectra and the resulting stellar mass probability distribution as determined by the stellar mass code (from Bundy et al. 2005a). The photometry points are plotted and final mass indicated. The dashed lines denote the 68% confidence intervals in the derived stellar mass.

Photometric errors enter the analysis by determining how well the template SEDs can be constrained by the data. Larger photometric uncertainties "smear out" the portion of the model grid that fits an observed galaxy with high probability. This is reflected in a wider stellar mass probability distribution. Additional uncertainties in the K_s-band luminosity (from errors in the observed total K_s-band magnitude) lead to final stellar mass estimates that are typically good to 0.2–0.3 dex. The largest systematic source of uncertainty comes from the assumed IMF, in this case that proposed by Chabrier (2003). The stellar masses we derive using this IMF can be converted to Salpeter by adding 0.3 dex.

2.4.1 Optical Masses, Photo-z's, and Other Caveats

The combination of extensive spectroscopic redshifts and K-band photometry makes the DEEP2/Palomar survey an ideal and unique data set for tracing the stellar mass evolution of galaxies. Other groups have attempted to estimate stellar masses without this important combination, lacking spectroscopy (e.g., Drory et al. 2004a), near-IR data (e.g. COMBO17), or both (e.g., Gwyn et al. 2005). I discuss some concerns about these efforts as well as general caveats about stellar mass estimates below.

Spectroscopic redshifts not only precisely locate galaxies in space and time but enable the reliable determination of restframe quantities such as color and luminosity which are critical for accurate comparisons to stellar population templates and the ability to measure luminosity and convert to stellar mass. The additional stellar mass uncertainty resulting from the use of typical photo-z's is illustrated in Figure 2.11, taken from Bundy et al. (2005a). In this experiment we measure photometric redshifts for galaxies that already have secure spectroscopic redshifts and use these photometric redshifts to determine a second set of stellar mass estimates. Figure 2.11 shows the difference in stellar mass for the same galaxies when photometric redshifts are used instead of spectroscopic redshifts, plotted as a function of their spectroscopic redshift. Individual mass estimates become less certain, and there are several catastrophic outliers with stellar masses that differ by an order of magnitude.

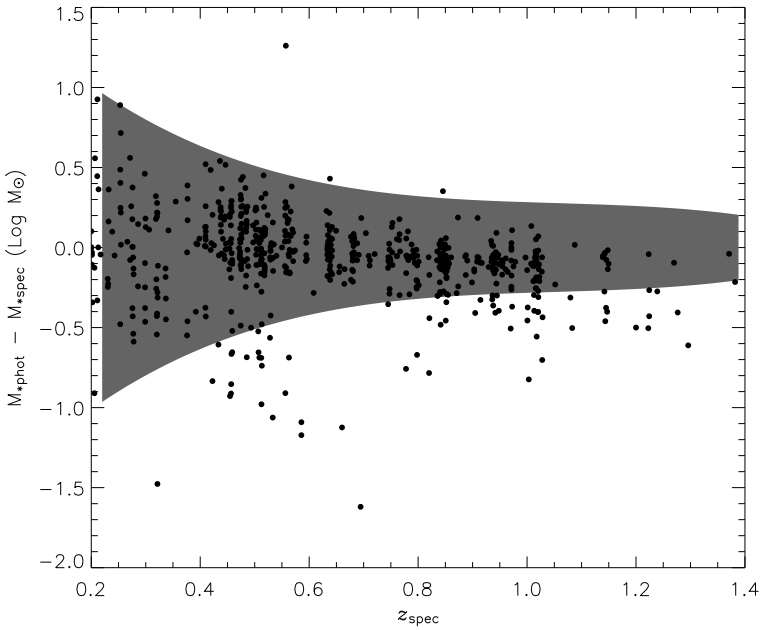

Figure 2.11 Difference in estimated stellar mass for our spectroscopic sample when photo-z's are used instead of spec-z's. The shaded region shows the expected standard deviation resulting from variations in the luminosity distance due to photo-z error.

The shaded region shows the standard deviation in stellar mass error based on a Monte Carlo simulation of 20,000 galaxies in which simulated redshifts were drawn from the observed photometric redshift error distribution ($\sigma[\Delta z/(1+z)] = 0.12$). The simulation includes only the primary effect on the luminosity distance. The shaded region accounts for both the rms uncertainty and the effect of catastrophic photo-z failures since both are included in the measurement of $\sigma[\Delta z/(1+z)]$.

Figure 2.11 shows a systematic offset such that most of the dramatic outliers tend to have lower masses when photometric redshifts are used than when spectroscopic redshifts are used. This trend is a common result of photo-z codes based on priors, which, as discussed in §3.2.3, often assign outliers lower photo-z measurements as compared to their spectroscopic values. The smaller luminosity distance that results from the photo-z underestimate leads to stellar masses that are also underestimated.

The importance of near-IR observations was discussed by Kauffmann & Charlot (1998) and first exploited by Brinchmann & Ellis (2000) who demonstrate that near-infrared and especially K-band photometry traces the bulk of the established stellar

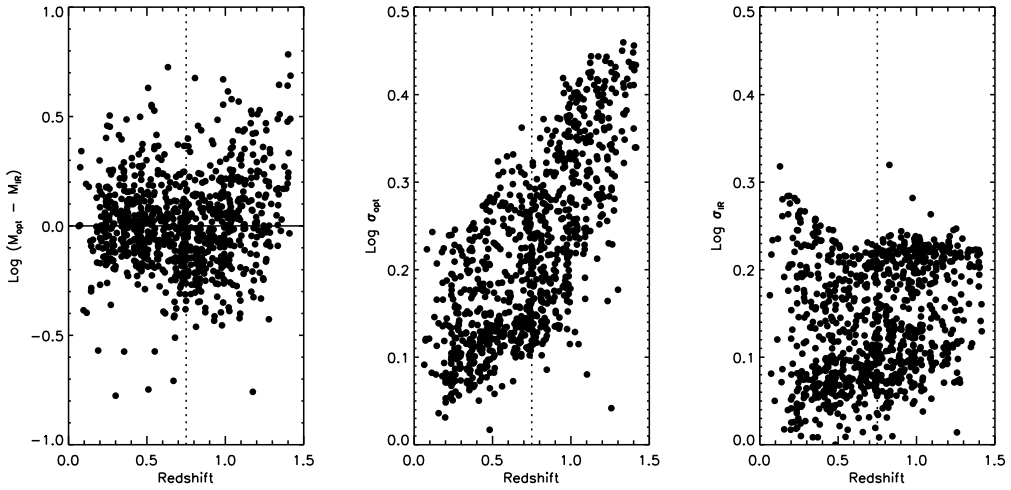

Figure 2.12 Uncertainties present in optical stellar mass estimates. The left-hand plot shows the difference between stellar masses estimated with BRI photometry and those with K-band included, based on a random sample drawn from the EGS. At all redshifts there are significant discrepancies in the optical masses. The range of errors increases beyond $z = 0.75$ (dotted line). This is also apparent in the uncertainties of the optical masses plotted in the middle diagram. The IR masses maintain relatively low uncertainties at all redshifts in the DEEP2 sample.

populations and enables reliable stellar mass estimates for $z \lesssim 1.5$. With the addition of SED fitting from multi-band optical photometry, the final uncertainty in such estimates can be reduced to factors of $\sim$2 based on K-band observations out to $z \approx 1.5$ (Brinchmann & Ellis 2000). The importance of K-band observations is highlighted in Figure 2.12. At all redshifts the optical masses derived from BRI photometry exhibit significant errors, some approaching an order of magnitude discrepancy. This is especially a problem for galaxies with $z > 0.75$, where the I-band filter begins sampling the restframe SED blueward of the 4000 angstrom break. As shown in the middle plot of Figure 2.12, estimated uncertainties from optical mass estimates become even less secure as the redshift increases and increasingly bluer portions of the restframe SED are shifted into the reddest filter bands. Thus, a comparison to Figure 2.11 shows that the combined lack of K-band photometry and spectroscopic redshifts leads to stellar mass errors greater than factors of 5–10 with catastrophic failures off by nearly two orders of magnitude.

Even with the combination of near-IR and spectroscopic redshifts, stellar mass

estimates like those described here suffer inherent uncertainties and are unlikely to improve much beyond the 50% level even with the best observations. The primary difficulty lies in accurately modeling the stellar population. The code described in the previous section uses the simplest simple stellar population (SSP) models, and while these do a fair job representing the global properties of galaxies, they are limited in accuracy because they cannot reflect the complex formation history we know most galaxies undergo. Some authors like Papovich et al. (2001) and Kauffmann et al. (2003a) have fit observed SEDs with multi-component models. These are typically used to constrain the maximum allowable stellar mass, but they entail added complexity and parameters which are difficult to constrain and in most cases do not improve the final mass estimate.

Furthermore, even templates with precise and accurate star formation histories suffer from the assumptions that go into them. Comparisons between different models made by different authors using the same parameters do not always give the same results (Drory et al. 2004b). There are differences in prescriptions for abundance ratios, dust extinction, and the contribution of hard-to-model components like AGB stars, to name a few (see Bruzual & Charlot 2003).

So, while stellar estimates provide a unique and valuable tool for charting galaxy evolution, their utility and precision only goes so far and is unlikely to be vastly improved upon in the future. In the work described in the following chapters, I rely heavily on stellar mass estimates to trace the evolution of galaxies but maintain a conservative approach when evaluating their precision.

Chapter 3

The Mass Assembly Histories of Galaxies of Various Morphologies in the GOODS Fields[1]

We present an analysis of the growth of stellar mass with cosmic time partitioned according to galaxy morphology. Using a well-defined catalog of 2150 galaxies based, in part, on archival data in the Great Observatories Origins Deep Survey (GOODS) fields, we assign morphological types in three broad classes (Ellipticals, Spirals, Peculiar/Irregulars) to a limit of z_{AB}=22.5 and make the resulting catalog publicly available. Utilizing 893 spectroscopic redshifts, supplemented by 1013 determined photometrically, we combine optical photometry from the GOODS catalog and deep K_s-band imaging to assign stellar masses to each galaxy in our sample. We find little evolution in the form of the galaxy stellar mass function from $z \sim 1$ to $z = 0$, especially at the high mass end where our results are most robust. Although the population of massive galaxies is relatively well established at $z \sim 1$, its morphological mix continues to change, with an increasing proportion of early-type galaxies at later times. By constructing type-dependent stellar mass functions, we show that in each of three redshift intervals, E/S0's dominate the higher mass population, while spirals are favored at lower masses. This transition occurs at a stellar mass of 2–3$\times 10^{10}$ $M_\odot$ at $z \sim 0.3$ (similar to local studies), but there is evidence that the relevant mass scale moves to higher mass at earlier epochs. Such evolution may represent the mor-

[1]Much of this chapter has been previously published as Bundy et al. (2005a)

phological extension of the "downsizing" phenomenon, in which the most massive galaxies stop forming stars first, with lower mass galaxies becoming quiescent later. We infer that more massive galaxies evolve into spheroidal systems at earlier times and that this morphological transformation may only be completed 1–2 Gyr after the galaxies emerge from their active star forming phase. We discuss several lines of evidence suggesting that merging may play a key role in generating this pattern of evolution.

3.1 Introduction

Great progress has been made in recent years in defining the star formation history of galaxies (Madau et al. 1996; Blain et al. 1999). The combination of statistically complete redshift surveys (Lilly et al. 1995a; Ellis et al. 1996; Steidel et al. 1999; Chapman et al. 2003) and various diagnostics of star formation (UV continua, recombination lines, and sub-mm emission) has enabled determinations of the co-moving star formation (SF) density at various redshifts whose rise and decline around $z \simeq 2$ points to the epoch when most stars were born (e.g., Rudnick et al. 2003; Bouwens et al. 2003; Bunker et al. 2004). Many details remain to be resolved, for example in reconciling different estimators of star formation (e.g., Sullivan et al. 2004) and the corrections for dust extinction. In addition, recent theoretical work including both numerical simulations and semi-analytic modeling is in some confusion as to the expected result (e.g., Baugh et al. 1998; Somerville et al. 2001; Nagamine et al. 2004).

An independent approach to understanding how galaxies form is to conduct a census of galaxies *after* their most active phases and to track their growing stellar masses. The co-moving stellar mass density at a given redshift should represent the integral of the previously-discussed SF density to that epoch, culminating in its locally-determined value (Fukugita et al. 1998). Unlike the star formation rate (SFR), the stellar mass of a galaxy is less transient and can act as a valuable tracer for evolutionary deductions.

Further insight is gained by tracing the integrated growth in stellar mass of dif-

ferent populations. For example, the rapid decline with time in the SF density over $0 < z < 1$ (Lilly et al. 1996; Fall et al. 1996) appears to result from the demise of an abundant population of star forming, irregular galaxies (Glazebrook et al. 1995; Abraham et al. 1996; Brinchmann et al. 1998). By considering the declining stellar mass density associated with irregular galaxies, Brinchmann & Ellis (2000) suggested that these sources transform, either by mergers or other means, into the slowly growing mass identified with regular ellipticals and spirals.

In a complementary fashion, the recent completion of large infrared surveys like K20 (Cimatti et al. 2002) and MUNICS (Drory et al. 2001) has traced the distribution in mass of the most massive galaxies out to $z \sim 2$ (Fontana et al. 2004; Drory et al. 2004a). These and other studies find a decrease in the overall normalization of the combined galaxy stellar mass function with redshift. Fontana et al. (2004) find very little evolution in the shape of the combined mass function out to $z \sim 1$. Drory et al. (2004a), in contrast, argue for a stronger evolution out to $z \sim 1$ based on a decrease in the characteristic mass and steepening of the faint–end slope. The MUNICS survey, though extensive in size, relies primarily on photometric redshifts and, at $K \lesssim 18.7$ (Vega), probes a limited mass range. The deeper K20 survey, on the other hand, utilizes primarily spectroscopic redshifts but is much smaller and suffers more from cosmic variance.

With sufficient data, it is possible to combine these earlier approaches, which concentrated on either volume-integrated quantities of separate populations or the mass distribution of combined galaxy types, and construct the stellar mass functions of individual populations. At $z = 0$, Bell et al. (2003) have used measurements of concentration and color in the Sloan Digital Sky Survey (SDSS) to classify galaxies as early or late type and derived separate mass functions for each, demonstrating that early-types dominate at higher masses. Baldry et al. (2004) use the bimodal color distribution observed in SDSS to separate early from late populations and find similar results. At higher redshifts, Fontana et al. (2004) were the first to examine type-dependent mass functions and divided their sample based on spectral type, finding some evidence for bimodality.

The public availability of ACS images and photometry in the Great Observatories Origins Deep Survey (GOODS, Giavalisco et al. 2004) together with spectroscopic redshifts (e.g., Wirth et al. 2004; Le Fèvre et al. 2004) provides a new opportunity for making progress at $z \sim 1$. With the addition of infrared photometry, it is possible to characterize the mass functions of separate and well defined *morphological* populations, although the small size of the GOODS fields makes cosmic variance one of the primary sources of uncertainty. It is therefore advantageous to combine the two GOODS fields, even though GOODS-N has the benefit of roughly twice as many spectroscopic redshifts as GOODS-S. With the various data sets available in GOODS, we can begin mapping out the mass assembly history responsible for the origin of the Hubble Sequence as well as understanding the physical processes that drive this assembly.

A plan of this work follows. In §3.2 we discuss the essential ingredients: the infrared data, including new K_s-band imaging of the GOODS-N field undertaken with the Hale 5m reflector at Palomar; visual morphologies of the ACS-selected galaxies in GOODS; and spectroscopic and photometric redshifts. In §3.3 we briefly discuss our method for measuring stellar masses for galaxies of known redshift based on infrared and optical photometry. In §3.4 we discuss important issues of completeness and selection effects in the sample. In §3.5 we present the methods and results of our analysis of the stellar mass functions and the integrated mass density of various morphological populations. We summarize and conclude in §3.7. Throughout, we assume a cosmological model with $\Omega_{\rm M} = 0.3$, $\Omega_\Lambda = 0.7$, and $H_0 = 100h$ km s^{-1} Mpc^{-1}.

3.2 Data

This study relies on the combination of many different data sets in the GOODS fields including infrared observations, spectroscopic and photometric redshifts, and HST morphologies.

3.2.1 Infrared Imaging

Because deep infrared data is not publicly available in GOODS-N, we carried out K_s-band imaging of the GOODS-N field in three overlapping pointings $8\farcm6$ on a side, using the Wide-field Infrared Camera (WIRC, Wilson et al. 2003) on the Hale 5m telescope at Palomar Observatory. The observations were made in November 2002, January 2003, and April 2003 under slightly different conditions. The total integration times for each of the sub-fields of 15ks, 13ks, and 5.6ks account for the different observing conditions so that the final depth in each pointing is similar. Mosaics of numerous coadditions of a sequence of 4×30 second exposures were taken in a non-repeating pattern of roughly $7\farcs0$ dithers and processed using a double-pass reduction pipeline we developed specifically for WIRC (see §2.3). The individual observations were combined by applying weights based on the seeing, transparency, and background for each observation. The final data quality is excellent, with average FWHM values for stars in the WIRC images of $0\farcs85$ for the first two fields and $1\farcs0$ for the third. Because the WIRC camera field is fixed North-South and cannot be rotated and only three positions were imaged, the overlap with the GOODS-N region is only $\sim 70\%$.

The WIRC images were calibrated by observing standard stars during photometric conditions and checked with comparisons to published K-band photometry from Franceschini et al. (1998). A comparison for relatively bright stars in each field was also made with 2MASS. Photometric errors and the image depth were estimated by randomly inserting fake objects of known magnitude into each image and then recovering them with the same detection parameters used for real objects. The inserted objects were given Gaussian profiles with a FWHM of $1\farcs3$ to approximate the shape of slightly extended, distant galaxies. The resulting 80% completeness values in the K_s-band are 22.5, 22.8, and 22.4 AB, which are similar to the 5-σ detection limit in each image.

Infrared imaging is publicly available for GOODS-S. We utilized K_s-band data taken with the SOFI instrument on the NTT because it is similar in depth and resolution to the Palomar observations. The SOFI data reach $K_s < 22.5$ (AB, 5-σ)

with stellar FWHM values less than 1.″0 on average. Detailed information on the SOFI observations can be found in Vandame et al. (2001).

For the infrared imaging in both GOODS fields we used SExtractor (Bertin & Arnouts 1996) to make a K-band catalog, limited to $K_s = 22.4$ (AB), and for total magnitudes we use the SExtractor Kron estimate. We do not adjust the Kron magnitude to account for missing light in extended sources. The optical-infrared color measurements, which are used for estimating photometric redshifts and stellar masses, are determined from 1.″0 radius aperture photometry. In the case of the infrared data, these measurements are made by SExtractor. They are then compared to the catalog of optical ACS $BViz$ 1.″0 photometry as tabulated by the GOODS team (Giavalisco et al. 2004).

3.2.2 ACS Morphologies

Based on version 1.0 HST/ACS data released by the GOODS team (Giavalisco et al. 2004), a z-selected catalog was constructed with a magnitude limit of $z_{AB} = 22.5$, where reliable visual morphological classification was deemed possible. The resulting sample of 2978 objects spread over both GOODS fields was inspected visually by one of us (RSE) who classified each object (using techniques discussed in detail by Brinchmann et al. 1998) according to the following scale: -2=Star, -1=Compact, 0=E, 1=E/S0, 2=S0, 3=Sab, 4=S, 5=Scd, 6=Irr, 7=Unclass, 8=Merger, 9=Fault. Following Brinchmann & Ellis (2000), we divide these classes into three broad categories: "E/S0" combines classes 0, 1, and 2 and contains 627 galaxies; "Spirals" combines classes 3, 4, and 5 and contains 1265 galaxies; and "Peculiar/Irregular" comprises classes 6, 7 and 8 and contains 562 galaxies. The morphological catalog is publicly available at `www.astro.caltech.edu/GOODS_morphs/`.

Some caution is required in comparing these morphological classifications over a range of redshifts. Surface brightness dimming can bias high redshift morphologies towards early-type classifications. We see evidence for this effect when we compare the 5 epoch, version-1.0 GOODS morphologies to previous determinations made by

RSE for the same sample of objects in a single epoch of the version-0.5 GOODS release. The overall agreement is excellent, with the more shallow, single-visit classes offset from the deeper stacked equivalent by only 0.1 types on the 12-class scheme defined above (see Treu et al. 2005b). The standard deviation of this comparison is 1.3 morphological classes, demonstrating that the effect on the broader morphological categories, which combine three classes into one, would be minimal. Furthermore, the $z_{AB} < 22.5$ limit is one magnitude brighter than the 80% completeness limit of the ACS data for objects with half-light radii less than $1\farcs0$ (Giavalisco et al. 2004). Thus the high signal-to-noise of the $z_{AB} < 22.5$ sample ensures robust classifications to $z \sim 1$.

Wavelength dependent morphological k-corrections are often more important for comparisons across different redshifts. The morphological classifications made here were carried out first in the z-band, in which the lowest redshift bin at $z \approx 0.3$ samples restframe R-band while the highest redshift bin at $z \approx 1$ samples restframe B-band. However, after the first pass, Viz color images were inspected and about 5% of the sample was corrected (by never more than one class) based on the color information. In this way, the galaxies suffering most from the morphological k-correction were accounted for.

We can gain a quantitative estimate for the remaining k-correction effect by referencing the "drift coefficients" tabulated in Table 4 of Brinchmann et al. (1998) and extrapolating them from the I-band to our z-band classifications. We would expect very small k-corrections until the highest redshift bin ($z \approx 1$) which is equivalent in wavelength to the $z = 0.7$ interval in Brinchmann et al. (1998). At this point, Brinchmann et al. (1998) estimate that ≈13% of Spirals are misclassified as Peculiars, while the Ellipticals and Spirals exchange ≈25% of their populations, leaving the relative numbers nearly the same.

The results of Brinchmann et al. (1998) were based on automated classifications carried out using the Asymmetry–Concentration plane, however, and may overestimate the magnitude of the k-correction. Many other groups have also investigated this effect (e.g., Kuchinski et al. 2000, 2001; Windhorst et al. 2002; Papovich et al.

2003) and suggest milder results. The k-corrections are found to be most severe when optical morphologies are compared to the mid-UV. None of the classifications in our sample were based on restframe mid-UV morphology. Furthermore, most studies have found that early-type spirals, with their mixture of star formation and evolved stellar populations, show the most drastic changes between red and UV wavelengths, while other types vary less because they are either completely dominated by young stars (late-type disks, Peculiars) or have little to no star formation at all (Ellipticals). Indeed, Conselice et al. (2005) compare visual classifications similar to those presented here in WFPC2 I and NICMOS H-band for 54 galaxies in HDF-N with $z < 1$ and find that only 8 disagree. Most of these were labeled as early-types in H-band and as early-type disks in I-band. Based on these various studies, we expect that the wavelength dependent k-corrections remaining in the sample are important only at the highest redshifts. Even then they are likely to be small because the z-band is still redward of the restframe UV. Although we choose not to explicitly correct for the morphological k-correction, we estimate that statistically over the redshift range 0.5-1, where the bulk of the evolutionary trends are seen, at most 5—10% of the populations are misidentified in our broad classification system.

3.2.3 Spectroscopic and Photometric Redshifts

Accurate redshifts are important not only for identifying members of a given redshift interval but for determining luminosities and stellar masses. Spectroscopic redshifts were taken from two sources. The Keck Team Redshift Survey (KTRS) provides redshifts for GOODS-N and was selected in R and carried out with DEIMOS on Keck II (Wirth et al. 2004). The KTRS is 53% complete to $R_{AB} < 24.4$, giving a sample of 1440 galaxy redshifts and providing redshifts for 761 galaxies (58%) in the GOODS-N morphological catalog described above. After our additional K_s-band requirement (see §3.4), this number reduces to 661 galaxies primarily because the K_s-band imaging covers only ≈70% of GOODS-N. Spectroscopic redshifts in GOODS-S were taken from the VIMOS VLT Deep Survey (Le Fèvre et al. 2004) which is 88% complete to

$I_{AB} = 24$ and accounts for 300 galaxies (25%) in the GOODS-S morphological catalog. We supplement this sample with 792 photometric redshifts (66%) from COMBO-17 (Wolf et al. 2004).

For more than half of the total morphological sample, published redshifts are not available and photometric redshifts have to be measured. In GOODS-S, 107 photometric redshifts were needed, while in GOODS-N the number was 343. The inclusion of these redshifts and the requirement of K_s-band photometry yields a final morphological sample that is complete to $z_{AB} < 22.5$ and $K_s < 22.4$ (AB). We also constructed a fainter sample with $z_{AB} < 23.5$ that is too faint for reliable morphological classification but allows for investigations of completeness (see §3.5.2). Photometric redshifts were estimated using the Bayesian Photometric Redshift (BPZ) Code described in Benítez (2000). Using the same priors that Benítez (2000) applies to the HDF-N, we ran the BPZ software on the 1.″0 diameter fixed-aperture ACS and K_s-band photometry, allowing for two interpolation points between templates. The KTRS and VIMOS spectroscopic redshifts were used to characterize the quality of a subset of the photometric redshifts (see Figure 3.1). The results were similar for both GOODS fields, with a combined mean offset of $\Delta z/(1 + z_{spec}) = -0.02$ and an rms scatter of $\sigma[\Delta z/(1+z_{spec})] = 0.12$, similar to the precision achieved by Mobasher et al. (2004), who used BPZ to estimate redshifts in GOODS-S. We did not, however, correct for the poorer resolution ($\sim$1.″0) of the K_s-band data.

The comparison between photo-z's and spec-z's in Figure 3.1 shows a tendency for photo-z's to be underestimated. There is a set of objects with spec-$z < 0.5$ that have photometric redshifts near 0.2. At spec-$z \approx 1$ there is another more mild deviation toward lower photo-z's that is likely due to the Bayesian prior (Benítez 2000) which assumes a decreasing redshift distribution at $z \sim 1$. In general, there appears to be more catastrophic outliers with photo-z underestimates. Much of this behavior is likely related to the lack of U-band photometry, which is crucial to ruling out false low-z photometric solutions.

Over the redshift range of interest, $0.2 < z < 1.4$, the final sample consists of 1906 galaxies, of which 893 (47%) have spectroscopic redshifts and 1013 (53%) have

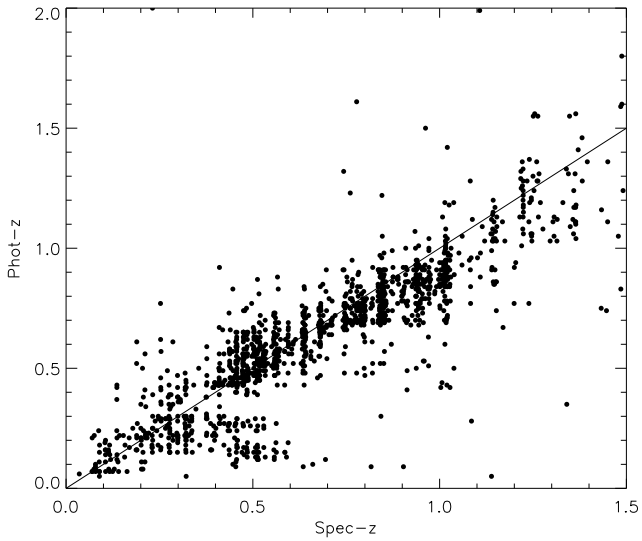

Figure 3.1 Results of the photometric redshift estimation using the BPZ code by Benítez (2000). The plot illustrates the difference between photo-z's and spectroscopic redshifts (where they exist).

photometric redshifts. We divide the sample into three redshift intervals, $0.2 < z < 0.51$, $0.51 < z < 0.8$, and $0.8 < z < 1.4$, chosen to balance the number of objects in each interval. The morphological breakdown (Ellipticals, Spirals, Peculiars) in each redshift bin is as follows: for $0.2 < z < 0.51$, (167, 353, 126); for $0.51 < z < 0.8$, (220, 326, 138); and for $0.8 < z < 1.4$ (131, 291, 154).

3.3 Determination of Stellar Masses

Estimating stellar masses using the combination of infrared imaging, multi-band photometry, and redshift information is now a widely applied technique first utilized by Brinchmann & Ellis (2000). In this work we use a Bayesian stellar mass code based on the precepts described in Kauffmann et al. (2003a) and discussed in detail in Chapter 2. Briefly, the code uses the multi-band photometry and redshift to compare the observed SED of a sample galaxy to a grid of synthetic SEDs (from Bruzual & Charlot 2003) spanning a range of star formation histories (parametrized as an exponential), ages, metallicities, and dust content. The K-band mass-to-light ratio

(M_*/L_K), stellar mass, χ^2, and the probability that the model represents the data are calculated at each grid point. The probabilities are then summed across the grid and binned by stellar mass, yielding a stellar mass probability distribution for each galaxy. We use the median of the distribution as an estimate of the final stellar mass. Photometry errors enter the analysis by determining how well the model SEDs can be constrained by the data. This is reflected in the stellar mass probability distribution which provides a measure of the uncertainty in the stellar mass estimate given by the width of the distribution. The largest systematic source of uncertainty comes from our assumed IMF, in this case that proposed by Chabrier (2003). Masses derived assuming this IMF can be converted to Salpeter by adding 0.3 dex.

Despite the large number of spectroscopic redshifts, when the stellar mass estimator is applied to galaxies with photometric redshifts, additional errors must be included to account for the much larger redshift uncertainty. At the same time, catastrophic photo-z errors (which are apparent in Figure 3.1) can significantly affect mass estimates. Redshift errors enter in two ways. First, they affect the determination of the galaxy's restframe SED because k-corrections cannot be as accurately determined. This can alter the best fitting model and the resulting mass-to-light ratio. Far more important, however, is the potential error in the luminosity distance from the increased redshift uncertainty. For the standard cosmology we have assumed, a redshift uncertainty of $\sigma[\Delta z/(1+z)] = 0.12$ can lead to an error of roughly 20% in luminosity distance. This can contribute to an added mass uncertainty of almost 50%.

The additional stellar mass uncertainty resulting from the use of photo-z's was discussed in §2.4.1. In light of the these uncertainties, we add an additional 0.3 dex of uncertainty to stellar masses gleaned from the photometric redshift sample.

3.4 Completeness and Selection Effects in the Sample

The final sample combines several data sets leading to complicated completeness and bias effects that must be carefully examined. First, as described in §3.2.2, because accurate morphological classifications are required, the sample was limited to $z_{AB} < 22.5$ to ensure the fidelity of those classifications. Second, reliable stellar mass estimates at redshifts near $z \approx 1$ require three key ingredients: 1) multi-band optical photometry, 2) K_s-band photometry, and 3) redshifts. The optical photometry comes from the GOODS ACS imaging. Since the ACS catalog was selected in the z-band, the $z_{AB} < 22.5$ limit applies to these data as well. The K_s-band imaging was described in §3.2.1. As illustrated in the color-magnitude diagram in Figure 3.2, this depth is adequate for detecting the vast majority (95%) of the objects that lie within the area covered by the infrared imaging and satisfy the $z_{AB} < 22.5$ criterion. Thus, with the sample already limited in the z-band, requiring an additional K_s-band detection does not introduce a significant restriction, and we can consider the final sample complete to $z_{AB} < 22.5$.

The third ingredient in the stellar mass estimate—the galaxy's redshift—comes from a combination of sources (§3.2.3). Figure 3.2 plots the location on the color-magnitude diagram of those galaxies with $z_{AB} < 22.5$ that do not have spectroscopic redshifts (open symbols). They account for 54% of the final sample and are assigned redshifts based on the photo-z technique described in §3.2.3. The fact that almost half of the galaxies in the sample have spectroscopic redshifts is an important advantage for precise mass functions. Relying entirely on photo-z's would blur the edges of the redshift intervals and introduce additional uncertainty to every galaxy in the survey, as discussed in §3.3.

Despite the limitations of the various data sets required for this study, the final sample suffers almost exclusively from the magnitude cut in the z-band. Because it is a magnitude limited sample, it is incomplete in mass, and, at the highest redshifts, the objects with the reddest $(z - K_s)$ colors will begin to drop out of the sample. This is

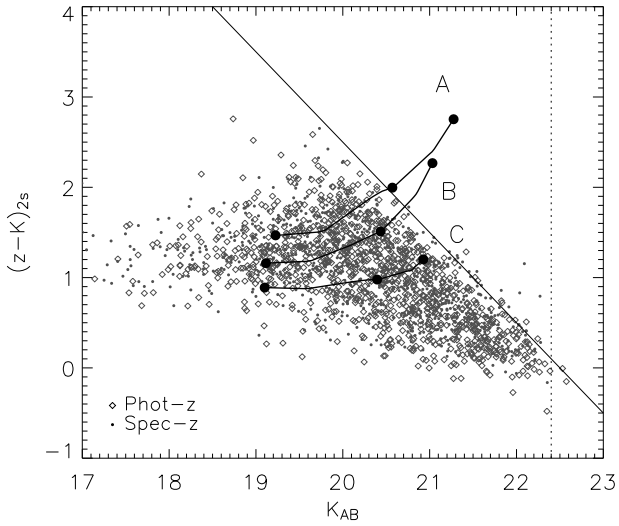

Figure 3.2 $(z - K_s)$ versus K_s color-magnitude relation. The small solid points are galaxies with spectroscopic redshifts. Open symbols denote those galaxies with photometric redshifts. The thin solid line illustrates the $z_{AB} < 22.5$ morphological classification limit, while the dotted line traces the completeness limit of the K_s-band data from Palomar and ESO. Three simple stellar population models, each with L_K^* luminosity and a formation redshift of $z_{form} = 10$, are also plotted. Models A and B have exponential SF timescales of $\tau = 0.4$ Gyr and metallicities of Z=0.05 for A and Z=0.02 (Z$\odot$) for B. Model C has $\tau = 4.0$ Gyr and solar metallicity. The large solid dots denote redshifts, from left to right, $z = 0.4$, 0.8, and 1.2.

illustrated by the expected location on the color-magnitude diagram of three different stellar population models, each with a luminosity of $L_K^* \approx -24$ at all redshifts (see Figure 3.2). Models A and B have exponential SF timescales of $\tau = 0.4$ Gyr and metallicities of Z=0.05 ($2.5Z\odot$) for A and Z=0.02 (Z$\odot$) for B. Model C has $\tau = 4.0$ Gyr and solar metallicity. The large solid dots denote redshifts $z = 0.4$, 0.8, and 1.2. In the highest redshift bin ($0.8 < z < 1.4$), the redder, passively evolving sources can be expected to suffer most from the z-band cut. As these are likely to be massive, we would expect their absence to also be reflected in the combined mass function.

Following previous work (e.g., Fontana et al. 2003), we can translate the z-band cut into a conservative mass completeness limit by estimating the mass corresponding to a reasonable maximum M_*/L_z ratio as a function of redshift. To do this, we calculate the mass of a near-instantaneous burst model with a formation redshift

of $z_{form} = 10$, no dust, sub-solar metallicity, and a luminosity corresponding to an observed magnitude of $z_{AB} = 22.5$ at all redshifts. The resulting mass completeness limits rise from 10^{10} $M_\odot$ at $z \sim 0.3$ to 10^{11} $M_\odot$ at $z \sim 1$. In §3.5.3, we further discuss how mass incompleteness impacts the derived mass functions at $0.8 < z < 1.4$.

3.5 Results

3.5.1 Methods and Uncertainties

Given the small area of the GOODS fields (0.1 square degrees), cosmic variance and clustering in these intervals will affect the mass functions we derive. Somerville et al. (2004) present a convenient way to estimate cosmic variance based on the number density of a given population and the volume sampled. Using these techniques, we estimate that uncertainties from cosmic variance range from ≈20% in the highest redshift bin to ≈60% in the lowest. This translates into an additional 0.1–0.3 dex of uncertainty in the final mass functions.

In deriving a mass or luminosity function in a magnitude limited survey, faint galaxies not detected throughout the entire survey volume must be accounted for. Many techniques exist to accomplish this while preventing density inhomogeneities from biasing the shape of the derived luminosity function (for a review, see Willmer 1997). However, there is no cure for variations from clustering and cosmic variance. With an expected uncertainty from cosmic variance of ∼40% on average, these variations will affect comparisons we might draw between redshift intervals. Given these limitations we adopt the simpler V_{max} formalism (Schmidt 1968). The V_{max} estimate is the volume corresponding to the highest redshift, z_{max}, at which a given galaxy would still appear brighter than the $z_{AB} = 22.5$ magnitude limit and would remain in the sample. For a galaxy i in a redshift interval, $z_{low} < z < z_{hi}$,

$$V_{max}^{i} = d\Omega \int_{z_{low}}^{\min(z_{hi}, z_{max})} \frac{dV}{dz} dz, \tag{3.1}$$

where $d\Omega$ is the solid angle subtended by the survey and dV/dz is the comoving

volume element.

The stellar mass estimator fits a model spectrum to each galaxy. By redshifting this model spectrum and integrating it over the z-band filter response function, we can calculate the apparent z-band magnitude as a function of redshift, implicitly accounting for the k-correction. The quantity, z_{max}, is determined by the redshift at which the apparent magnitude becomes fainter than $z_{AB} = 22.5$.

Once V_{max} is estimated, we calculate the comoving number density of galaxies in a particular redshift bin and stellar mass interval, $(M_* + dM_*)$, as,

$$\Phi(M_*)dM_* = \sum_i \frac{1}{V_{max}^i} dM_*, \tag{3.2}$$

where the sum is taken over all galaxies i in the interval.

The V_{max} formalism is appealing because it is easy to apply and makes no assumptions on the form of the luminosity or mass function. It can be biased by clustering since it assumes galaxies are uniformly distributed through the survey volume. This bias is best understood through the observed redshift distributions (Figure 3.3). In the lowest redshift bin, the concentration at the high end of the redshift interval near $z = 0.47$ leads to an underestimate in the mass function, especially for the number densities of fainter galaxies that cannot be detected at the furthest distances in this interval. In the highest redshift bin, the redshift spikes at the low-z end have the opposite effect. In this case, clustering increases the resulting mass function by causing an overestimate of galaxies that would not be detected if the redshift distribution was more uniform. Clustering can also affect the type-dependent stellar mass functions because early-type galaxies are expected to be more strongly clustered than later types.

Other uncertainties in deriving the mass function are greatly reduced by utilizing spectroscopic redshifts. The effect on the mass functions caused by uncertainty in photo-z estimates and stellar mass errors is estimated in the following way. We use a Monte Carlo technique to simulate 100 realizations of our data set, utilizing the resulting variation in the observed mass functions to interpret the errors. For a given

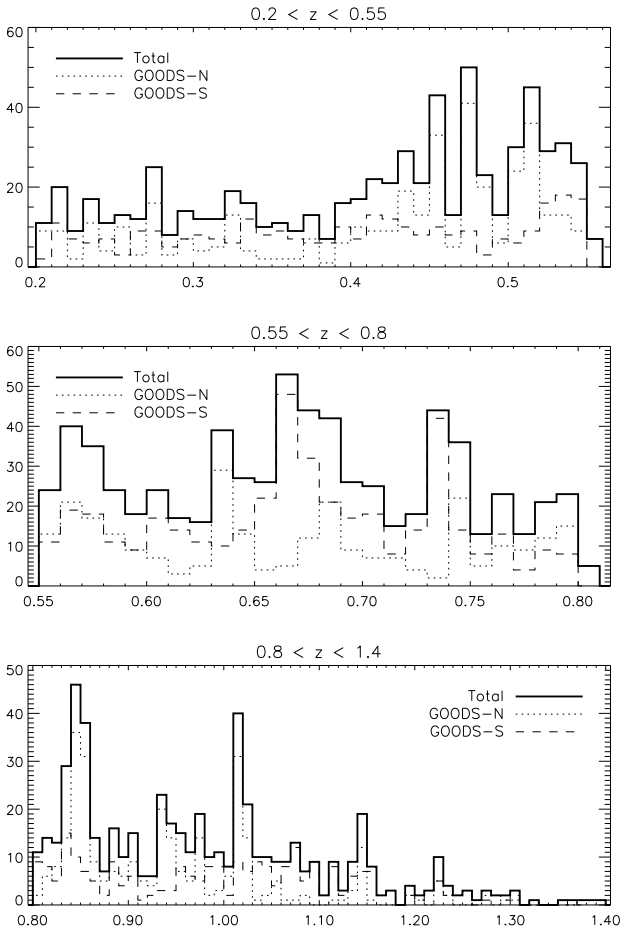

Figure 3.3 Redshift distributions for the primary GOODS sample with $z_{AB} < 22.5$.

realization, the stellar mass of each galaxy is drawn randomly from the stellar mass probability distribution determined by the mass estimator (see §3.3), thus avoiding any assumption about the form of the estimated mass distribution. Galaxies with photometric redshifts tend to smear out the edges of the redshift intervals. In the simulations, the realized redshift for these galaxies is drawn from a Gaussian distribution with $\sigma = \sigma[\Delta z/(1 + z_{spec})] = 0.12$, the same rms measured for galaxies with both spectroscopic and photometric redshifts. The effect of this redshift uncertainty on the luminosity distance is also included in the stellar mass error budget (see §3.3).

3.5.2 Galaxy Stellar Mass Functions

We plot the resulting galaxy stellar mass functions for all types in Figure 3.4. The solid lines trace the best fit to the local mass function measured by Cole et al. (2001) (we do not plot the results of Bell et al. (2003) which are consistent with Cole et al. (2001)). The redshift dependent mass functions derived by Drory et al. (2004a) (also plotted as "plus" symbols) come from a larger photo-z sample that is most complete at higher masses. Results from the spectroscopic K20 survey are shown as squares (Fontana et al. 2004). We note that the lower result from Fontana et al. (2004) in the high-z bin may be caused by mismatched redshift intervals. Their result for $1.0 < z < 1.5$ is plotted, but their $0.7 < z < 1.0$ mass function (shown in the middle plot of Figure 3.4) may provide a more adequate comparison considering that our high-z bin includes many galaxies in the range $0.8 < z < 1.0$.

Also plotted in Figure 3.4 are the combined mass functions for a larger, unclassified, photometric sample where the z-band magnitude cut has been increased to $z_{AB} = 23.5$. Though reliable visual morphological classification is not feasible for objects in the ACS data with $z_{AB} > 22.5$, the fainter sample demonstrates the effects of incompleteness in the primary ($z_{AB} = 22.5$) catalog, which become particularly important in the highest redshift bin. The point at which the morphological sample begins to show a deficit with respect to the fainter sample is consistent with the mass completeness limits calculated based on the maximum M_*/L_z ratio (see §3.4). For the three redshift intervals, the estimated mass incompleteness limits are, in order of increasing redshift, 10^{10} $M_\odot$, 4×10^{10} $M_\odot$, and 10^{11} $M_\odot$. As discussed in §3.5.1, in addition to completeness, cosmic variance and clustering dominate the small GOODS area and make interpretations of the mass function difficult.

We fit Schechter functions to the binned data, including fits to separate morphological populations (see §3.5.3), and show the resulting parameters in Table 3.1. The primary and extended samples are quite similar in the first two redshift intervals, with incompleteness in the primary sample becoming significant in the third ($0.8 < z < 1.4$). Across the full redshift range, the combined mass function shows

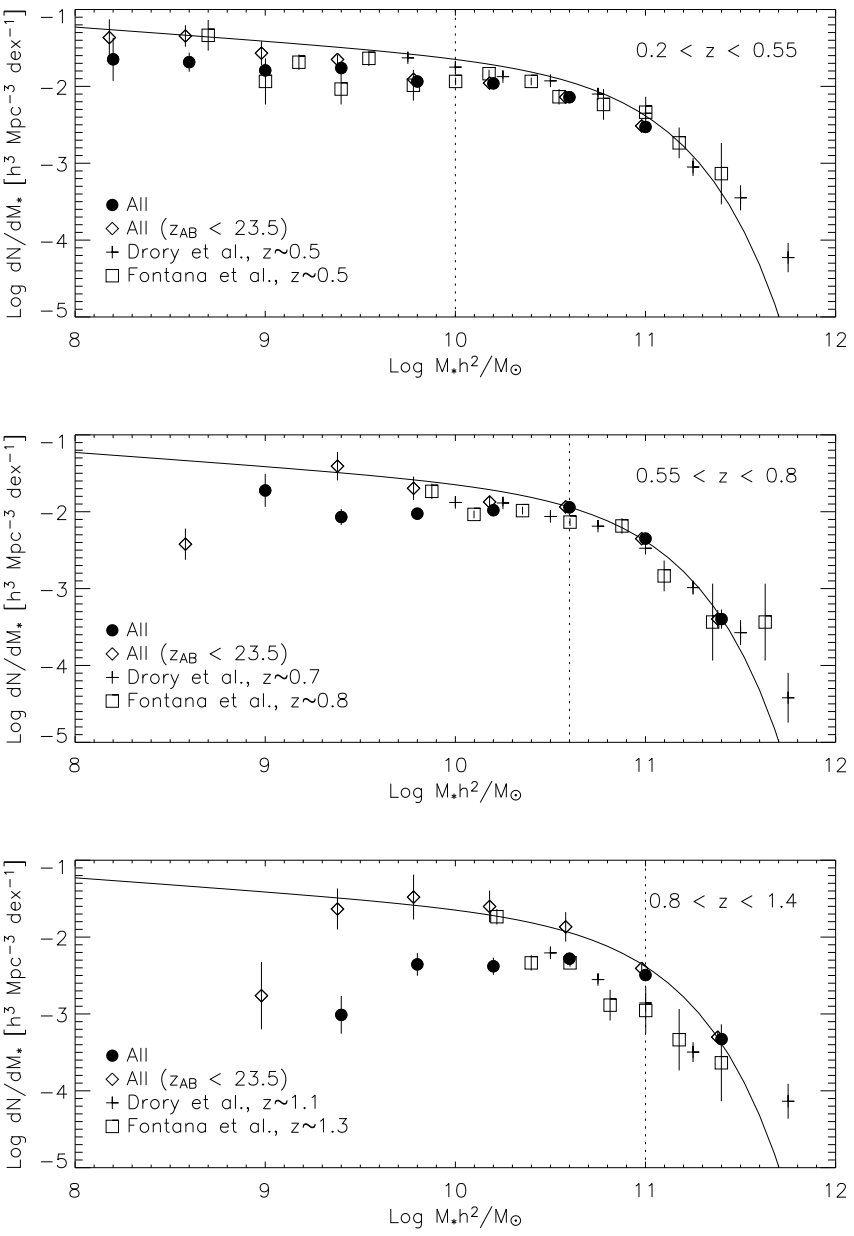

Figure 3.4 Total galaxy stellar mass functions in three redshift intervals. The solid line is the best fit to the $z = 0$ mass function from Cole et al. (2001). Results from Drory et al. (2004a) and the "best–fit" stellar mass functions from Fontana et al. (2004) are shown after correcting for different choices of the IMF and Hubble Constant. For the brighter, $z_{AB} < 22.5$ sample, mass completeness limits based on a maximum reasonable M_*/L_K ratio (see §3.4) are indicated by the dotted lines. The error bars are calculated from Monte Carlo simulations that account for uncertainties arising from the photometry, stellar mass estimates, photo-z estimates, and Poisson statistics.

little evolution and remains similar in shape to its form at $z = 0$.

These results are consistent with previous work. Fontana et al. (2004) find little evolution out to $z \sim 1$ in the mass function derived from the K20 survey (also plotted). The K20 sample (Cimatti et al. 2002) has good spectroscopic coverage (92%) but is slightly shallower (0.5 mag in K) and roughly one quarter of the size of the sample studied here. The MUNICS survey (Drory et al. 2001), in contrast, contains 5000 galaxies spread over several fields, covering a much larger area. It is roughly one and a half magnitudes shallower in K and consists primarily ($\approx$90%) of photometric redshifts. Drory et al. (2004a) argue that the MUNICS combined mass function exhibits significant evolution to $z = 1.2$, with a decrease in the characteristic mass and steepening of the faint–end slope. Considering the uncertainties, we feel the MUNICS result is consistent with the work presented here, although we differ in the interpretation.

Theoretical models currently yield a variety of predictions for the combined galaxy stellar mass functions. Fontana et al. (2004) compare predictions from several groups with various techniques including semi–analytic modeling and numerical simulations. In general, semi–analytic models (e.g., Cole et al. 2000; Somerville et al. 2001; Menci et al. 2004) tend to produce mass functions that evolve strongly with redshift, with decreasing normalization and characteristic masses that together underpredict the observed number of massive, evolved galaxies at high redshift. Rapid progress in addressing this problem is currently underway. Numerical models (e.g., Nagamine et al. 2004) better reproduce a mildly evolving mass function and more easily account for high mass galaxies at $z \sim 1$, but sometimes overpredict their abundance (see the discussion in §3.5.3 on massive galaxies). Observations of the galaxy stellar mass function and its evolution thus provide key constraints on these models.

3.5.3 Type-Dependent Galaxy Mass Functions

In Figure 3.5 we show the galaxy stellar mass functions for the three broad morphological populations derived using the V_{max} formalism described in §3.5.1. As a check,

we also calculated mass functions after applying a z-band absolute magnitude limit of $M_z < -20.3$, to which nearly every galaxy can be detected at every redshift. Absolute magnitudes are determined through SED fitting as part of the stellar mass estimator (§3.5.1). Though less complete, the general characteristics of the mass functions with $M_z < -20.3$ agree well at high stellar masses with those derived using the V_{max} method.

All three redshift bins in Figure 3.5 are complete at $M_* > 10^{11}$ $M_\odot$, and little difference is seen in the combined mass function between the morphological sample (with $z_{AB} < 22.5$) and the fainter sample ($z_{AB} < 23.5$). This allows for a comparison of the morphological makeup of the high-mass population. In the highest redshift bin, we find that Spirals are slightly favored at $M_* \approx 10^{11}$ $M_\odot$ and are competitive with E/S0's at $M_* \approx 3 \times 10^{11}$ $M_\odot$. At the same time, Peculiars make a significant contribution at these masses. Both the Peculiar and Spiral populations drop at lower redshifts as E/S0's become increasingly dominant at high masses.

Turning now to the broader range of masses sampled by the data, the first redshift bin exhibits a transitional mass of $M_{tr} \approx 2$–3×10^{10} $M_\odot$ ($\log_{10} M_{tr} \approx 10.3$–$10.5$) below which the E/S0 population declines while the Spiral population rises, becoming the dominant contributor to the combined mass function. Across the three redshift bins studied here, it appears this transitional mass shifts to lower mass with time as the contribution of the E/S0 population to low mass galaxies increases. We caution that M_{tr} is close to the estimated mass completeness limit, especially in the $0.55 < z < 0.8$ redshift bin.

Tracing evolution at masses below M_{tr} is difficult because of incompleteness. As discussed in §3.4, we would expect early-type galaxies to be increasingly absent in the z-selected sample at higher redshifts. Thus, much of the more rapid decline in the E/S0 contribution at $0.8 < z < 1.4$ may be due to the z-band magnitude cut. When our cut is relaxed to $z_{AB} = 23.5$, we can expect that many of these missing E/S0's will re-enter the sample and that this would drive the combined mass function to levels more comparable to those observed at lower redshift. One line of evidence in support of this is the predominantly red $(V - K_s)$ color of the galaxies introduced

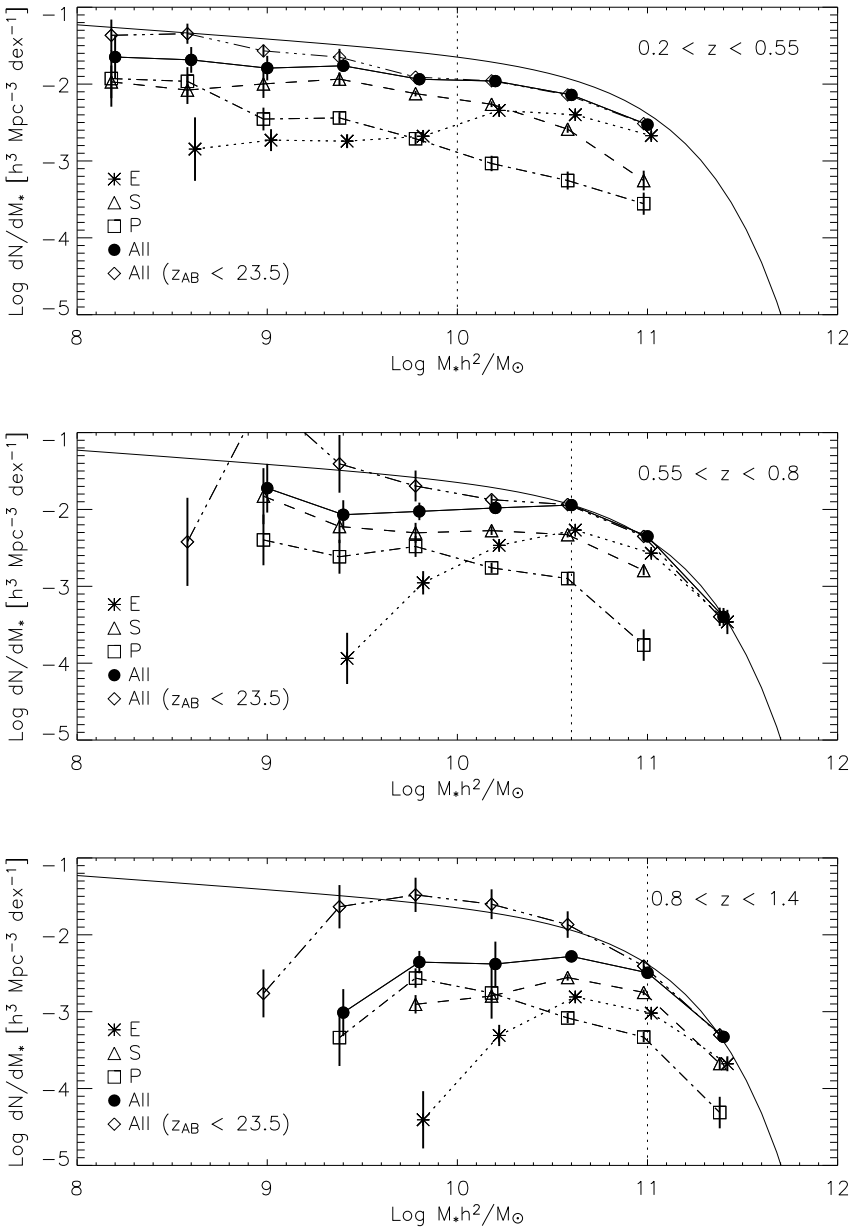

Figure 3.5 Galaxy stellar mass function in three redshift intervals split by morphology. The $z = 0$ mass function from Cole et al. (2001, solid line) and the total mass functions are also shown. Mass completeness limits based on a maximum reasonable M_*/L_K ratio (see §3.4) are indicated by the dotted lines. The error bars are calculated from Monte Carlo simulations that account for uncertainties arising from the photometry, stellar mass estimates, photo-z estimates, and Poisson statistics.

into the sample when the z_{AB} limit is relaxed to 23.5. For stellar masses greater than $\approx 10^{10}$ $M_\odot$, the $(V - K_s)$ distribution of these galaxies is very similar to the E/S0 population in the $z_{AB} < 22.5$ sample. Their low asymmetries, as measured through the CAS system (Conselice 2003), are also consistent with an E/S0 population. With decreasing stellar mass, the asymmetry values increase and the color distribution spreads towards the blue, suggesting that, at lower masses, other galaxy types enter the fainter, high-z sample as well.

Our suggestion that an E/S0 population is primarily responsible for adjusting the combined mass function (for $M_* \gtrsim 10^{10}$ $M_\odot$) is also consistent with the contribution of Spirals which, in the high-z bin, is a factor of $\sim$70% lower at $M_* = 1.6 \times 10^{10}$ $M_\odot$ ($\log_{10} M_*/M_\odot = 10.2$) than in the mid-$z$ bin. At this same mass in the high-z bin, however, the combined mass function increased by almost an order of magnitude when galaxies with $z_{AB} < 23.5$ are included. Much of this increase is likely to come from E/S0's that were previously missed.

Table 3.1. Stellar Mass Function Parameters

	Total			GOODS-N			GOODS-S		
Sample	ϕ^*	α	$\log_{10} M^*h^2$	ϕ^*	α	$\log_{10} M^*h^2$	ϕ^*	α	$\log_{10} M^*h^2$
				$0.2 < z < 0.55$					
All	5.4 ± 0.9	-1.04 ± 0.18	10.85 ± 0.10	5.8 ± 1.3	-1.03 ± 0.21	10.81 ± 0.10	4.9 ± 0.5	-1.05 ± 0.11	10.86 ± 0.06
All $z_{AB} < 23.5$	4.3 ± 0.7	-1.16 ± 0.16	10.94 ± 0.08	4.0 ± 0.5	-1.18 ± 0.11	10.99 ± 0.06	4.1 ± 1.2	-1.16 ± 0.27	10.92 ± 0.13
E/S0	4.5 ± 1.5	-0.42 ± 0.48	10.70 ± 0.15	3.8 ± 0.5	-0.56 ± 0.15	10.74 ± 0.06	5.6 ± 1.1	-0.16 ± 0.47	10.52 ± 0.09
Spiral	3.4 ± 0.7	-1.08 ± 0.25	10.58 ± 0.11	3.1 ± 0.5	-1.15 ± 0.16	10.69 ± 0.09	1.1 ± 0.1	-1.35 ± 0.06	10.90 ± 0.06
Peculiar	0.1 ± 0.0	-1.60 ± 0.12	11.52 ± 0.24	0.1 ± 0.0	-1.51 ± 0.06	11.45 ± 0.16	0.3 ± 0.0	-1.60 ± 0.13	10.71 ± 0.10
				$0.55 < z < 0.8$					
All	11.9 ± 1.5	-0.51 ± 0.33	10.67 ± 0.05	10.0 ± 1.0	-0.45 ± 0.26	10.65 ± 0.04	15.3 ± 1.1	-0.48 ± 0.20	10.70 ± 0.03
All $z_{AB} < 23.5$	8.6 ± 1.5	-1.09 ± 0.39	10.83 ± 0.06	6.2 ± 1.1	-1.15 ± 0.22	10.86 ± 0.07	9.6 ± 1.8	-1.18 ± 0.30	10.91 ± 0.06
E/S0	6.0 ± 0.4	0.22 ± 0.22	10.55 ± 0.02	4.4 ± 0.5	0.26 ± 0.45	10.52 ± 0.05	8.0 ± 0.6	0.00 ± 0.22	10.68 ± 0.03
Spiral	5.0 ± 2.3	-0.69 ± 1.04	10.66 ± 0.19	4.6 ± 0.7	-0.68 ± 0.37	10.66 ± 0.07	6.0 ± 0.7	-0.57 ± 0.40	10.62 ± 0.05
Peculiar	1.5 ± 1.3	-1.01 ± 1.19	10.55 ± 0.31	0.7 ± 0.2	-0.81 ± 0.29	11.18 ± 0.53	1.4 ± 0.5	-1.03 ± 0.31	11.03 ± 0.36
				$0.8 < z < 1.4$					
All	5.3 ± 0.5	-0.50 ± 0.36	10.80 ± 0.03	6.8 ± 0.3	-0.02 ± 0.16	10.72 ± 0.01	3.1 ± 0.3	-0.88 ± 0.33	10.84 ± 0.03
All $z_{AB} < 23.5$	6.2 ± 5.4	-1.19 ± 2.66	10.90 ± 0.28	9.1 ± 1.2	-0.99 ± 0.30	10.86 ± 0.02	3.5 ± 0.8	-1.50 ± 0.34	10.92 ± 0.06
E/S0	1.5 ± 0.2	0.11 ± 0.45	10.73 ± 0.04	1.8 ± 0.1	0.64 ± 0.23	10.62 ± 0.02	1.2 ± 0.3	-0.61 ± 0.64	10.83 ± 0.11
Spiral	3.1 ± 0.4	-0.24 ± 0.46	10.73 ± 0.04	4.0 ± 0.5	-0.14 ± 0.42	10.74 ± 0.05	1.1 ± 0.3	-0.75 ± 0.66	11.02 ± 0.17
Peculiar	0.7 ± 0.4	-1.23 ± 0.72	10.92 ± 0.21	0.6 ± 0.2	-0.52 ± 0.76	10.90 ± 0.14	1.4 ± 0.4	-0.74 ± 0.55	10.60 ± 0.07

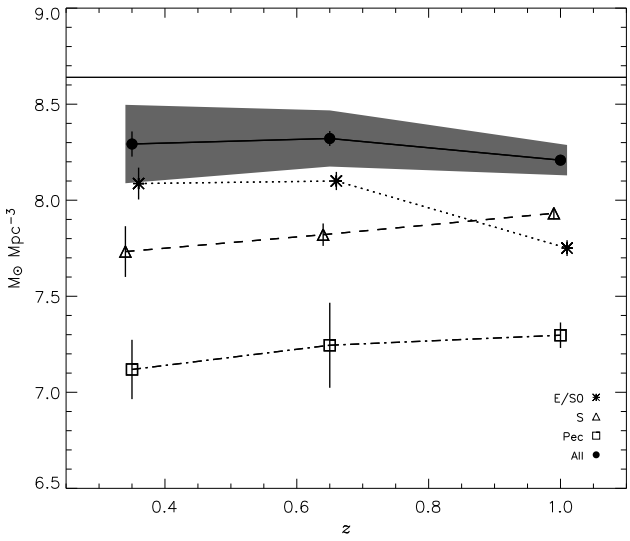

Figure 3.6 Integrated stellar mass density as a function of redshift, split by morphology and with a mass cut of $M_* > 10^{11}$ $M_\odot$. The straight, solid line at the top of the plot shows the local stellar mass density as measured by Cole et al. (2001). The shaded region illustrates the uncertainty from cosmic variance.

3.5.4 Integrated Stellar Mass Density

Following Brinchmann & Ellis (2000), in Figure 3.6 we show results for the type-dependent stellar mass density as a function of redshift. In this analysis we have implemented a mass limit of $M_* > 10^{11}$ $M_\odot$; thus we are mass complete in all three redshift bins. We find that the total stellar mass density grows by $\simeq$30% from $z \sim 1$ to $z = 0$, although the uncertainty from cosmic variance is large. The morphological breakdown of the increase in stellar mass density illustrates a demise in the contribution from Spirals and Peculiars accompanied by a rise in the density of Ellipticals. The error bars indicated on Figure 3.6 were calculated using the same Monte Carlo technique that was applied to the mass functions. In this way, the uncertainties account for errors in photometry, stellar mass estimates, and photometric redshifts. The shaded region in Figure 3.6 demonstrates the expected uncertainty due to cosmic variance.

The observed 30% increase in the integrated stellar mass density is consistent with measurements by other groups (e.g., Cohen 2002; Fontana et al. 2003; Dickinson

et al. 2003) and can be reconciled with the observed star formation rate over the same redshift range (e.g., Fontana et al. 2003). As shown in Figure 3.6, we find similar results for the morphological dependence of the growth of stellar mass as Brinchmann & Ellis (2000). The sample presented here is more complete because it was selected in z-band, not I-band, and is almost 7 times larger, resulting in smaller random errors. We note that Brinchmann & Ellis (2000) do not estimate the affect of cosmic variance on their sample, which we find to be the primary uncertainty, nor do they ensure that their sample is mass complete. As suggested by Brinchmann & Ellis (2000), the rise of the Elliptical population implies that other galaxies, including Peculiars and Spirals, transform into early-type galaxies with time.

3.6 Discussion

In broad terms, our results support two independent and consistent perspectives on the mass assembly history of galaxies since $z \sim 1$. On the one hand, global measures of the mass distribution, such as the combined galaxy stellar mass function, show little evolution in the distribution of massive galaxies from $z \sim 1$ to $z = 0$. This implies that much of the observed star formation and associated stellar growth over this interval occurs in lower mass galaxies. On the other hand, a more dynamic perspective emerges when the mass distribution is considered according to galaxy type. In this study we have shown that although the number density of massive galaxies is relatively fixed after $z \sim 1$, the morphological composition of this population is still changing such that the more balanced mix of morphological types at $z \sim 1$ becomes dominated by ellipticals at the lowest redshifts. Strikingly, this morphological evolution also appears to occur first at the highest masses, proceeding to rearrange the morphologies of lower mass galaxies as time goes on. In this section we explore how these two perspectives—little total stellar mass evolution overall accompanied by more substantial internal changes—lend insight into the mechanisms responsible for the growth of galaxies and the development of the Hubble Sequence.

As we discuss in §3.5.2, the observed stellar mass function, which is not affected

by incompleteness at high mass in our survey, shows little evolution from $z \sim 1$ to $z = 0$ in agreement with previous work (e.g., Drory et al. 2004a; Fontana et al. 2004; Bell et al. 2004). Although it appears that the stellar content of massive galaxies is relatively well established by $z \sim 1$, the nature of these galaxies continues to change. This effect can be seen in Figure 3.5 in the mass bin centered at 10^{11} $M_\odot$ ($10.8 < \log M_*/M_\odot < 11.2$) where, in all three redshift intervals, our sample is complete with respect to a maximum M_*/L_K ratio. Ellipticals, Spirals, and Peculiars contribute in similar numbers at the highest redshift, while at the lowest redshift Ellipticals clearly dominate. This trend is similar to the growth in stellar mass density of these morphological populations as observed by Brinchmann & Ellis (2000) and illustrated in Figure 3.6.

Studying this growth as a function of mass provides additional information on how Ellipticals come to dominate the massive galaxy population by $z \sim 0.3$. This growth of Ellipticals could arise from several processes including the formation of completely new galaxies, stellar mass accretion onto established systems of smaller mass, and the transformation of other established galaxies into ones with early-type morphologies. It is likely that all three processes contribute at some level, although the fact that the density of high-mass galaxies changes little since $z \sim 1$ places an important constraint on the amount of new growth—either through star formation or the build-up of smaller galaxies—that is possible. This growth is limited to at most a factor of $\sim$2, while the density of Ellipticals at $M_* \approx 10^{11}$ $M_\odot$ increases by a factor of $\sim$3. A more detailed examination of the effect of stellar mass accretion onto lower mass Ellipticals is difficult because of incompleteness in our survey. We estimate, however, that the typical stellar mass of an Elliptical with $M_* \approx 3 \times 10^{10}$ $M_\odot$ would have to at least triple in order to contribute significantly to the increasing proportion of high-mass Ellipticals. This spectacular growth in a just a few Gyr seems unlikely. Finally, Figure 3.5 shows that the rise of massive Ellipticals is accompanied by a *decline* in the other two populations. Thus, assuming that galaxies cannot be broken up or destroyed, morphological transformation of individual galaxies, whether through merging or some other mechanism like disk fading, must be a significant

driver in the evolution toward early-type morphologies.

At $z \sim 1$, the higher number of massive Peculiars—often associated with interacting systems—suggests that at least some of this morphological transformation is occurring through mergers, which are known to be more frequent at high-z (e.g Le Fèvre et al. 2000; Conselice et al. 2003). Indeed, Hammer et al. (2005) emphasize the importance of luminous IR galaxies (LIRGs), thought to be starbursts resulting from merging at these masses, and Bundy et al. (2004), examining galaxies with a broader range of stellar mass, used observations of the IR pair fraction to estimate that the total stellar mass accreted through merging since $z \sim 1$ is approximately $\Delta\rho_*^m \sim 10^8$ $M_\odot Mpc^{-3}$. As illustrated in Figure 3.6, this is close to the magnitude of the observed growth in the mass density of Ellipticals ($\Delta\rho_* \sim 8 \times 10^7$ $M_\odot Mpc^{-3}$), implying that merging may have an impact on the morphological transformation occurring among massive galaxies. However, significant rates of merging which would also affect the distribution of galaxies as a function of mass, are ruled out by the lack of strong evolution in the stellar mass function.

Turning now to the full range of stellar mass accessible in our sample, one of the key results of this work is the observation of a transitional mass, M_{tr}, above which Ellipticals dominate the mass function and below which Spirals dominate. This phenomenon is observed in studies at low redshift. Bell et al. (2003) find a cross-over point at $M_{tr} \approx 3 \times 10^{10}$ $M_\odot$ between the local stellar mass functions of early and late type galaxies, as classified by the concentration index (see the g-band derived stellar mass functions in their Figure 17). Analysis of the Sloan Digital Sky Survey (SDSS) reveals a similar value for M_{tr} (Kauffmann et al. 2003b; Baldry et al. 2004) which also serves as the dividing line in stellar mass for a number of bimodal galaxy properties separating early from late types. These include spectral age diagnostics (like $D_n(4000)$ and $H\delta_A$), surface mass densities, size and concentration, and the frequency of recent star bursts.

Theoretical work by Dekel & Birnboim (2004) suggests that, in addition to mergers, the effects of shock heating and supernova (SN) feedback weigh heavily on the evolution of galaxies, and both set characteristic scales that correspond to a stellar

mass of 3×10^{10} $M_\odot$ today. Galaxies form in halos below the M_{shock} threshold. If they remain below the SN feedback threshold, then SN feedback regulates star formation, leading to young, blue populations and a series of well defined scaling relations. Galaxies with masses above M_{shock} are formed by the merging of progenitors. Their gas is shock heated and may be prevented from cooling by AGN feedback, leading to older, redder populations and a different set of scaling laws (see Birnboim & Dekel 2003). The SN characteristic scale is expected to decrease with redshift while the shock heating scale remains constant (Dekel, private communication), so it is unclear how these physical scales are related to the evolution of M_{tr} for $z \lesssim 1$.

Whatever the processes at work, the interplay of the morphological populations and the possible evolution in M_{tr} as traced by Figure 3.5 seem to echo patterns in the global star formation rate as observed at higher redshift; the most morphologically evolved galaxies appear first at the highest masses, and their dominance over other populations spreads toward lower masses—thereby reducing M_{tr} —as time goes on. This is similar to the concept of "downsizing" (Cowie et al. 1996) in which the highest mass galaxies stop forming stars at the earliest times while progressively less massive galaxies end their star formation later. Although the evolution of star formation and morphology both appear to proceed first at the highest masses, downsizing as it relates to star formation predates morphological transformation by at least 1–2 Gyr. As reported by Juneau et al. (2005), the SFR of high-mass galaxies ($M_* > 6 \times 10^{10}$ $M_\odot$) goes through a transition at $z \approx 1.5$, emerging from a "burst phase" (in which the SFR multiplied by the age of the universe becomes comparable to the stellar mass) to become quiescent. According to Figure 3.5, these same high-mass galaxies are still evolving morphologically at $z \approx 0.8$, more than 1 Gyr later. This implies that the timescale of the transformation process is $\sim$1 Gyr, similar to the merger timescale, which is often estimated at 0.5 Gyr (e.g., Patton et al. 2000).

Downsizing may apply not only to galaxies undergoing bursts of vigorous star formation on short timescales but also to relatively quiescent galaxies with continuing, modest star formation. Treu et al. (2005a), for example, find that while massive spheroidals have mostly completed their star formation by $z \sim 2$, low mass field ellip-

ticals exhibit continuing star formation from $z < 1$. Thus, the pattern of downsizing in both star formation and morphology is gradual and appears to operate over a large range in mass and extend to the lowest redshifts.

The growing evidence for downsizing and its morphological extension raises many questions. While mergers offer a natural explanation for the link between the continuing star formation and morphological transformations we present in this work, it is not clear what is driving this mass-dependent downsizing behavior. Most likely several competing physical processes, including mass-dependent galaxy mergers, are responsible for shaping the Hubble Sequence.

3.7 Summary

We have studied the redshift dependent mass functions for three distinct morphological populations in a sample of 2150 galaxies with $z_{AB} < 22.5$ in the GOODS fields. For 44% of the sample, spectroscopic redshifts from the KTRS and VLT VIMOS surveys are available. We use photometric redshifts from the COMBO17 survey in GOODS-S for 37% of the sample and estimate photometric redshifts based on *BViz* ACS photometry for the remaining 19%. We utilize K_s-band observations of GOODS-N taken with the WIRC camera at Palomar Observatory and public K_s-band imaging of GOODS-S from the EIS survey to estimate stellar masses for the whole sample based on fitted mass-to-light ratios.

We find very little evolution in the shape of the combined mass function, which we fit using Schechter functions with slope $\alpha \approx -1.2$ and $\log_{10} M^* h^2 \approx 10.8$—$11.0$ over the whole redshift range studied ($0.2 < z < 1.4$). This is consistent with Fontana et al. (2004) and appears similar to Drory et al. (2004a), though Drory et al. (2004a) interpret their results as evidence for stronger evolution. Cosmic variance resulting from the small size of the GOODS fields is our primary source of uncertainty. The lack of significant evolution in the observed mass function implies that much of the stellar growth occurring since $z \sim 1$ takes place at lower masses not yet accessible to high-z stellar mass surveys.

Our main result is the type-dependent galaxy stellar mass functions over three redshift intervals spanning the range $0.2 < z < 1.4$. The morphological breakdown of the most massive galaxies ($M_* \approx 10^{11}$ $M_\odot$) changes significantly with redshift. At $z \sim 1$, Ellipticals, Spirals, and Peculiars are present in similar numbers. By a redshift of 0.3, Ellipticals dominate the high-mass population, suggesting that merging or some other transformation process is active.

At all redshifts in our sample, Spirals and Peculiars dominate at lower masses while E/S0's become prominent at higher masses. The observed transition mass, $M_{tr} = 2$–3×10^{10} $M_\odot$, is similar to that apparent in lower redshift studies. There is evidence that M_{tr} was higher at early times, suggesting a morphological extension of the "downsizing" pattern observed in the star formation rate. Just as the most massive galaxies emerge from a phase of rapid star formation at the earliest times, massive galaxies are also the first to evolve into predominantly early-type morphologies. This morphological transformation is completed 1–2 Gyr after the galaxies leave their bursting phase.

Finally, we derive the integrated stellar mass densities of the three populations and find similar results as Brinchmann & Ellis (2000). We find further evidence for the transformation of Peculiars as well as Spirals into early-type galaxies as a function of time. Based on the observed mass functions, this transformation process appears to be more important at lower masses ($M_* \lesssim 10^{11}$ $M_\odot$) because the most massive E/S0's are already in place at $z \sim 1$.

In the future it will be possible to extend this kind of study with the primary aim of reducing statistical uncertainty and the effects of cosmic variance. Large galaxy surveys like DEEP2 (Davis et al. 2003) and COMBO-17 (Rix et al. 2004) are promising in this regard because they contain tens of thousands of galaxies spread over a wide area, although we note that stellar mass studies benefit greatly from spectroscopic redshifts. Extending the combined mass function to lower masses may help reveal the nature of star formation from $z \sim 1$ to $z = 0$. At the same time, reducing cosmic variance will allow for more detailed studies on the type-dependent evolution of the mass function and its relation to merging and star formation.

Acknowledgments

We wish to thank the referee for very valuable comments, Dr. Tommaso Treu for help developing the morphological classification scheme and for useful discussions, and Dr. Jarle Brinchmann for advice on the stellar mass estimator. We also thank Dr. Avishai Dekel for helpful discussions.

Supported by NSF grant AST-0307859 and NASA STScI grant HST-AR-09920.01-A.

Chapter 4

The Mass Assembly History of Field Galaxies: Detection of an Evolving Mass Limit for Star-Forming Galaxies[1]

We characterize the mass-dependent evolution of galaxies in a large sample of more than 8,000 galaxies using spectroscopic redshifts drawn from the DEEP2 Galaxy Redshift Survey in the range $0.4 < z < 1.4$ and stellar masses calculated from K-band photometry obtained at Palomar Observatory. This sample spans more than 1.5 square degrees in four independent fields. Using restframe $(U-B)$ color and [OII] line widths, we distinguish star-forming from passive populations in order to explore the nature of "downsizing"—a pattern in which the sites of active star formation shift from high mass galaxies at early times to lower mass systems at later epochs. Over the redshift range probed, we identify a mass limit, M_Q, above which star formation appears to be quenched. The physical mechanisms responsible for downsizing can thus be empirically quantified by charting the evolution in this threshold mass. We find that M_Q decreases with time by a factor of $\approx$5 across the redshift range sampled according to $M_Q \propto (1+z)^{4.5}$. We demonstrate that this behavior is quite robust to the use of various indicators of star formation activity, including morphological type. To further constrain possible quenching mechanisms, we investigate how this downsizing signal depends on the local galaxy environment using the projected 3^{rd}-

[1]Much of this chapter has been previously published as Bundy et al. (2005b)

nearest-neighbor statistic $D_{p,3}$, which is particularly well-suited for large spectroscopic samples. For the majority of galaxies in regions near the median density, there is no significant correlation between downsizing and environment. However, a weak trend is observed in the comparison between more extreme environments that are more than 3 times overdense or underdense relative to the median. Here, we find that downsizing is accelerated in overdense regions which host higher numbers of massive, early-type galaxies and fewer late-types as compared to the underdense regions. Our results significantly constrain recent suggestions for the origin of downsizing and indicate that the process for quenching star formation must, primarily, be internally driven, with little dependence on large scale structure. By quantifying both the time and density dependence of downsizing, our survey provides a valuable benchmark for galaxy models incorporating baryon physics.

4.1 Introduction

The redshift interval from $z \approx 1$ to $z = 0$ accounts for roughly half of the age of the universe and provides a valuable baseline over which to study the final stages of galaxy assembly. From many surveys spanning this redshift range, it is now well-established that the global star formation rate (SFR) declines by an order of magnitude (e.g., Broadhurst et al. 1992; Lilly et al. 1996; Cowie et al. 1999; Flores et al. 1999; Wilson et al. 2002). An interesting characteristic of this evolution in SFR is the fact that sites of active star formation shift from including high mass galaxies at $z \gtrsim 1$ to only lower mass galaxies subsequently. This pattern, referred to by Cowie et al. (1996) as "downsizing," seems contrary to the precepts of hierarchical structure formation, and so understanding the physical processes that drive it is an important problem in galaxy formation.

The observational evidence for downsizing is now quite extensive. The primary evidence comes from field surveys encompassing all classes of galaxies to $z \approx 1$ and beyond (Brinchmann & Ellis 2000; Bell et al. 2005b; Bauer et al. 2005; Juneau et al. 2005; Faber et al. 2005). However, the trends are also seen in specific populations such

as field spheroidals, both in their stellar mass functions (Fontana et al. 2004; Bundy et al. 2005a) and in more precise fundamental plane studies (Treu et al. 2005a; van der Wel et al. 2005) which track the evolving mass/light ratio as a function of dynamical mass. The latter studies find that massive spheroidals completed the bulk of their star formation to within a few percent prior to $z \simeq 1$, whereas lower mass ellipticals continue to grow by as much as 50% in terms of stellar mass after $z \sim 1$. Finally, detailed analyses of the spectra of nearby galaxies suggest similar trends (Heavens et al. 2004; Jimenez et al. 2005).

Downsizing is important to understand as it signifies the role that feedback plays in the mass-dependent evolution of galaxies. As a consequence, its physical origin has received much attention theoretically. Recent analytic work by Dekel & Birnboim (2004), for instance, suggests that the distinction between star-forming and passive systems can be understood via several characteristic mass thresholds governed by the physics of clustering, shock heating, and various feedback processes. Some of these processes have been implemented in numerical and semi-analytic models, including mass-dependent star formation rates (Menci et al. 2005), regulation through feedback by supernovae (e.g., Cole et al. 2000; Benson et al. 2003; Nagashima & Yoshii 2004), and active galactic nuclei (AGN) (e.g., Silk & Rees 1998; Granato et al. 2004; Dekel & Birnboim 2004; Hopkins et al. 2005a; Croton et al. 2005; De Lucia et al. 2005; Scannapieco et al. 2005). However, most models have, until now, primarily addressed the mass distinction between star-forming and quiescent galaxies as defined at the present epoch (e.g., Kauffmann et al. 2003b). Quantitative observational measures of the *evolving mass dependence* via higher redshift data have not been available.

This work is concerned with undertaking a systematic study of how the mass-dependent growth of galaxies progresses over a wide range of epochs. The goal is to quantify the patterns by which assembly proceeds as a basis for further modeling. Does downsizing result largely from the assembly history of massive early-type galaxies or is there a decline in the fraction of massive star-forming systems? In the quenching of star formation, what are the primary processes responsible and how are they related to the hierarchical framework of structure assembly as envisioned in the

CDM paradigm? Does downsizing ultimately result from internal physical processes localized within galaxies such as star formation and AGN feedback (Croton et al. 2005; De Lucia et al. 2005), or is it caused by external effects related to the immediate environment, such as ram pressure stripping and encounters with nearby galaxies in groups and clusters?

In this study we combine the large spectroscopic sample contained in the DEEP2 Galaxy Redshift Survey (Davis et al. 2003) with stellar masses based on extensive near-infrared imaging conducted at Palomar Observatory to characterize the assembly history and evolution of galaxies since $z \approx 1.2$. Our primary goal is to quantify the downsizing signal in physical terms and test its environmental dependence so that it is possible to constrain the mechanisms responsible. A plan of this chapter is as follows. Section §4.2 presents the observations and characterizes the sample, while §4.3 describes our methods for measuring stellar masses, star formation activity, and environmental density. We discuss how we estimate errors in the derived mass functions in §4.4 and present our results in §4.5. We discuss our interpretations of the results in §4.6 and conclude in §4.7. Where necessary, we assume a standard cosmological model with $\Omega_{\rm M} = 0.3$, $\Omega_\Lambda = 0.7$, $H_0 = 100h$ km s^{-1} Mpc^{-1} and $h = 0.7$.

4.2 Observations and Sample Description

To constrain the processes that govern downsizing requires a precise measure of the evolving stellar mass function of galaxies as a function of their physical state and environmental density. Achieving this ambitious goal requires multi-wavelength observations capable of revealing quantities such as the ongoing star formation rate in a large enough cosmic volume to reliably probe a range of environments. Among these requirements, two observational components are absolutely essential: a large spectroscopic survey and near-IR photometry.

Spectroscopic redshifts not only precisely locate galaxies in space and time, but enable the reliable determination of restframe quantities such as color and luminosity. This in turn allows for accurate comparisons to stellar population templates which

provide stellar mass-to-light ratios (M_*/L) and the opportunity to convert from luminosity to stellar mass. As demonstrated in §2.4, relying on photometric redshifts (photo-z) decreases the typical precision of stellar mass estimates by more than a factor of three, with occasional catastrophic failures that lead to errors as large as an order of magnitude.

Spectroscopic redshifts are also crucial for determining accurate environmental densities (Cooper et al. 2005). Even with the most optimistic photometric redshift uncertainties of $\sigma_z = 0.02$—COMBO-17 specifies $\sigma_z \approx 0.03$ (Wolf et al. 2003)—a comparison between photo-z density measurements and the real-space density in simulated data sets gives a Spearman ranked correlation coefficient of only $\rho = 0.4$ (where $\rho = 1$ signifies perfect correlation, see Cooper et al. 2005). This uncertainty has the effect of smearing out the density signal in all but the lowest density environments in photo-z samples. For the spectroscopic DEEP2 sample used in this study, $\sigma_z = 0.0001$ and $\rho = 0.8$.

Spectroscopic observations also provide line diagnostics that can discriminate the star formation activity occurring in galaxies. Given the various timescales involved, it is useful to identify ongoing or recent star formation activity by considering various independent methods including restframe $(U-B)$ color, the equivalent width of [OII] λ3727, and galaxy morphology. Comparisons between the different indicators highlight specific differences between early- and late-type populations defined in different ways.

In addition to spectroscopy, the second essential ingredient in this study is near-IR photometry. As suggested by Kauffmann & Charlot (1998) and first exploited by Brinchmann & Ellis (2000), near-infrared and especially K-band photometry traces the bulk of the established stellar populations and enables reliable stellar mass estimates for $z \lesssim 1.5$. The importance of K-band observations is highlighted for galaxies with $z > 0.75$, where the typical stellar mass uncertainty using the same technique applied to photometry with the z-band as the reddest filter would be worse by a factor of 3–4 (see §2.4.1). The combined lack of K-band photometry and spectroscopic redshifts can lead to stellar mass errors greater than factors of 5–10 with catastrophic

failures off by nearly two orders of magnitude.

Because of these factors, the combination of the DEEP2 Galaxy Redshift Survey with panoramic IR imaging from Palomar Observatory represents the ideal (and perhaps only) data set for tracing the evolution of accurately measured stellar masses and various indicators of star formation activity across different environments to $z \approx 1.4$. We provide details on the specific components of this data set below.

4.2.1 DEEP2 Spectroscopy and Photometry

The DEEP2 Galaxy Redshift Survey (Davis et al. 2003) utilizes the DEIMOS spectrograph (Faber et al. 2003) on the Keck-II telescope and aims to measure ∼40,000 spectroscopic redshifts with $z \lesssim 1.5$ for galaxies with $R_{AB} \leq 24.1$. The survey samples four widely-separated regions covering a total area of 3.5 square degrees. In three of these fields, Fields 2–4, targets were color-selected in $(B - R)$ vs. $(R - I)$ color space so that the survey galaxies lie predominantly at redshifts greater than 0.7. This successfully recovers 97% of the $R_{AB} \leq 24.1$ population at $z > 0.75$ with only ∼10% contamination from lower redshift galaxies (Cooper et al. 2006). The redshift survey in these three fields is now complete, providing a total of 21592 successful redshifts over 3 square degrees. The last field, the Extended Groth Strip (EGS), covers 0.5 square degrees and is currently 75% complete with a total of 9501 galaxies in the range $0 < z < 1.5$. Here, a different selection strategy was employed to target equal numbers of galaxies above and below $z = 0.7$. In both the EGS and Fields 2–4, the sampling rate of galaxies satisfying the target criteria is ∼60%. DEEP2 galaxies from all four fields are included in this study.

DEEP2 redshifts were determined by comparing various templates to observed spectra as well as fitting specific spectral features. This process is interactive and is described in Cooper et al. (in preparation). Spectroscopic redshifts are used in this study only when two or more features have been identified in a given spectrum (giving "zquality" values ≥ 3, Faber et al. 2005). The fraction of objects for which this process fails to give a reliable redshift is roughly 30% and is dominated by faint blue

galaxies, the majority of which are beyond $z \sim 1.4$, where the [OII] λ3727 feature is redshifted beyond the DEEP2 spectral wavelength range (Willmer et al. 2005). More details on the redshift success rate are provided in Willmer et al. (2005), and Coil et al. (2004) further discuss the survey strategy and spectroscopic observations.

The spectroscopic sample is based on BRI photometry obtained at the Canada–France–Hawaii Telescope (CFHT) with the 12K×8K mosaic camera (Cuillandre et al. 2001). Catalogs selected in the R-band were constructed using the IMCAT photometric package (Kaiser et al. 1995) and reach a limiting magnitude of $R_{AB} \sim 25.5$ (Coil et al. 2004). The photometric calibration was computed with respect to SDSS observations which overlap a portion of the CFHT sample. The observed colors, used to estimate the inferred restframe $(U - B)$ colors in this study, were measured using apertures defined by the object size in the R-band image. Further details on the CFHT photometry can be found in Coil et al. (2004).

4.2.2 Palomar Near-IR Imaging

Motivated largely by this study, we have conducted an extensive panoramic imaging survey of all four DEEP2 fields with the Wide Field Infrared Camera (WIRC, Wilson et al. 2003) on the 5m Hale Telescope at Palomar Observatory. Details on this survey were presented in Chapter 2, but we reproduce some the salient points here.

The Palomar survey commenced in fall 2002 and was completed after 65 nights of observing in October 2005. Using contiguously spaced pointings (each with a camera field-of-view of $8\farcm6 \times 8\farcm6$) tiled in a 3×5 pattern, we mapped the central third of Fields 2–4 to a median 80% completeness depth greater than $K_{AB} = 21.5$, with 5 pointings deeper than $K_{AB} = 22.5$. The imaging in Fields 2–4 accounts for 0.9 square degrees, or 55% of the Palomar K_s-band survey.

The remainder of the data was taken in the EGS where the K_s-band data covers 0.7 square degrees, but to various depths. The EGS was considered the highest priority field in view of the many ancillary observations—including HST, Spitzer, and X-ray imaging—obtained there. In total, 35 WIRC pointings were used to map the EGS in

the K_s-band. The deepest observations were obtained along the center of the strip where there is complete overlap between WIRC and the spectroscopically-surveyed area. In these regions, the typical depth is greater than $K_{AB} = 22.5$. The rest of the southern half of the EGS reaches $K_{AB} = 22.3$, while that for the northern half is complete to $K_{AB} = 21.7$. Additional Palomar J-band observations were obtained for most of the central strip of the EGS and for Fields 3 and 4. These provide J-band photometry for roughly half of the K_s-band sample and are useful in improving the stellar mass estimates and photometric redshifts.

At a given pointing, individual mosaics were often obtained on different nights and so may vary in terms of seeing, sky background levels, and transparency. Most K_s-band pointings consist of more than two independently-combined mosaics with the deepest pointings comprising as many as 6 independent mosaics. The final seeing FWHM in the K_s-band images ranges from $0\farcs8$ to $1\farcs2$ and is typically $1\farcs0$. Photometric calibration was carried out by referencing standard stars during photometric conditions, and astrometric registration was performed with respect to DEEP2 astrometry (see Coil et al. 2004) using bright stars from the CFHT R-selected catalog.

After masking out the low signal-to-noise perimeter of the final K_s-band images, we used SExtractor (Bertin & Arnouts 1996) to detect and measure the K_s-band sources. As an estimate of the total K_s-band magnitudes, which are used to derive the luminosity and stellar mass of individual galaxies (see §4.3.1), we use the MAG_AUTO output from SExtractor. We also use SExtractor to measure aperture photometry in diameters of $2''$, $3''$, $4''$, and $5''$. To determine the corresponding magnitudes of K_s-band sources in the CFHT BRI and Palomar J-band images, we applied the IDL photometry procedure, APER, to these data, placing apertures with the same set of diameters at sky positions determined by the K_s-band detections. This method was adopted with the aim of producing a K-selected catalog—about 25% of the K_s-band sources do not have optical counterparts in the CFHT IMCAT catalog. Experimentation with color-color diagrams and photometric redshifts demonstrated that the $2''$ diameter colors exhibited the least scatter. We therefore use the $2''$ aperture colors for fitting template spectral energy distributions (SEDs) to constrain stellar mass es-

timates as well as to estimate photo-z's for sources beyond the DEEP2 spectroscopic limit.

Photometric errors and the K_s-band detection limit of each image were estimated by randomly inserting fake sources of known magnitude into each K_s-band image and recovering them with the same detection parameters used for real objects. We define the detection limit as the magnitude at which more than 80% of the simulated sources are detected. Robust photometric errors based on simulations involving thousands of fake sources were also determined for the BRI and J-band data. These errors are used to determine the uncertainty of the stellar masses and in the determination of photometric redshifts where required.

4.2.3 The Primary Sample

Given the various ingredients necessary for the data set, it is helpful to construct separate samples based on the differing completeness limits for the R-limited spectroscopic sample and the K-limited Palomar catalog.

We will define the primary sample as that comprising galaxies with DEEP2 spectroscopic redshifts that are also detected in the Palomar K_s-band imaging. Redshift counterparts were found by cross-referencing the K_s-band catalog with the DEEP2 redshift catalog and selecting matches for which the separation between the K_s-band and DEEP2 positions is less than $1\farcs1$. The relatively low surface density of both catalogs assures that the number of spurious associations is less than 1–2 percent. The fraction of DEEP2 redshifts detected in the K_s-band varies from ≈65% for K_s-band depths near $K_{AB} = 21.7$ to ≈90% for $K_{AB} = 22.7$. After removing the redshift survey boundaries to allow for unbiased density estimates (see §4.3.3), Fields 2, 3, and 4 host 953, 1168, and 1704 sample galaxies, respectively, all with secure spectroscopic redshifts in the range $0.75 < z < 1.4$. The fourth field, the EGS, contains 4770 galaxies with redshifts in the range $0.2 < z < 1.4$.

In the analysis that follows, we divide this sample into three broad redshift intervals. The first, $0.4 < z < 0.7$, contains 943 galaxies drawn entirely from the EGS,

while the second ($0.75 < z < 1.0$, 2210 galaxies) and third ($1.0 < z < 1.4$, 1430 galaxies) draw from all four fields (see Table 4.1). Although the entire spectroscopic sample was selected to have $R_{AB} \leq 24.1$, the limiting K_s-band magnitude was chosen separately for each redshift interval. Because the Palomar K_s-band survey covers different areas to different depths, the area and volume of a given subsample depend on the K_s-band limit that is applied. This is advantageous and allows us to choose limits for each redshift bin that maintain adequate statistics and stellar mass completeness while producing subsamples that probe similar cosmological volumes—an important consideration for environmental comparisons and for limiting the effects of cosmic variance. In the three redshift bins we select galaxies with secured K_s-band detections brighter than 21.8, 22.0, and 22.2 (AB), respectively. In the standard cosmology we have adopted with $h = 0.7$, the areas sampled with these limits result in volumes of 0.5, 1.4, and 2.3 in units of 10^6 Mpc^3.

4.2.4 The Photo-z Supplemented Sample

As mentioned previously, photometric redshifts are insufficient for accurate density measurements (Cooper et al. 2005), do not offer [OII]-based SFR estimates, and significantly decrease the precision of stellar mass (§2.4) and restframe color estimates. However, photometric redshifts do offer the opportunity to augment the primary sample and extend it to fainter magnitudes, providing a way to test for the effects of incompleteness in the primary spectroscopic sample because of the various magnitude limits and selection procedures. With this goal in mind, we constructed a comparison sample using the optical+near-IR photometry described above to estimate both photometric redshifts and stellar masses. We discuss the importance of this comparison in interpreting our results in section §4.4.2.

Photometric redshifts were derived in two ways. First, because the DEEP2 multi-slit masks do not target every available galaxy, there is a substantial number of objects that satisfy the photometric criterion of $R_{AB} \leq 24.1$ without spectroscopic redshifts. These are ideal for neural network photo-z estimates because of the availability of a

Table 4.1. Sample statistics

	Primary Spec-z, $R_{AB} \leq 24.1$	Photo-z Supplemented, $R_{AB} \leq 25.1$			
Sample	Number	Number	$f_{\text{spec-}z}$	$f_{\text{ANN}z}$	f_{BPZ}
		EGS Field			
Full sample	2669	8540	36%	51%	13%
$0.4 < z < 0.7$	943	3026	36%	62%	2%
$0.75 < z < 1.0$	1003	2801	42%	46%	12%
$1.0 < z < 1.4$	723	2713	29%	43%	28%
		DEEP2 Fields 2–4			
Full sample	1914	10156	21%	68%	11%
$0.4 < z < 0.7$	—	4264	2%	97%	1%
$0.75 < z < 1.0$	1207	2865	42%	48%	10%
$1.0 < z < 1.4$	707	3027	27%	47%	26%

Note. — The listed values reflect cropping the DEEP2 survey borders to allow for accurate environmental density measurements (see §4.3.3) and, for the three redshift intervals, K_s-band magnitude cuts of 21.8, 22.0, and 22.2 (AB).

large spectroscopic training set. For these galaxies, we use ANNz (Collister & Lahav 2004) to measure photo-zs, training the network with the EGS spectroscopic sample so that the ANNz results cover the full range $0.2 < z < 1.4$. Based on comparisons to the spectroscopic samples in Fields 2–4, the ANNz results are in excellent agreement with $\Delta z/(1+z) \approx 0.07$.

While the $R_{AB} \leq 24.1$ ANNz photo-z results present a complete sample, they do not contain fainter galaxies because no spectroscopic sample is available to train them. We therefore define a second sample of galaxies with $24.1 < R_{AB} \leq 25.1$ and 3σ detections in the BIK bands. For these we use the BPZ photo-z package (Benítez 2000) and $2\farcs0$ diameter aperture photometry, including J-band where available. We first optimize BPZ by comparing to spectroscopic samples. These tests reveal a systematic offset in the BPZ results that likely arises from the assumed HDF-North prior (Benítez 2000). We fit a linear relation to this offset and remove it from all subsequent BPZ estimates. This improves the spectroscopic comparison to $\Delta z/(1+z) \approx 0.17$.

Using the ANNz and BPZ results, we construct photo-z supplemented samples in each redshift bin with an R-band limit of $R_{AB} \leq 25.1$. The first bin, with $0.4 < z < 0.7$, contains 7290 galaxies; 16% have spectroscopic redshifts (available in the EGS only), 83% have ANNz photo-zs, and only 1% have BPZ photo-zs. The second bin, with $0.75 < z < 1.0$, contains 5666 galaxies; 42% have spectroscopic redshifts, 48% have ANNz photo-zs, and 10% have BPZ photo-zs. The third bin, with $0.75 < z < 1.0$, contains 5740 galaxies; 28% have spectroscopic redshifts, 45% have ANNz photo-zs, and 27% have BPZ photo-zs. The sample statistics are summarized in Table 4.1.

4.3 Determining Physical Properties

The goal of this study is to derive key physical quantities that can be used to describe the stellar mass, evolutionary state, and environmental density of galaxies and to use these measures to understand the physical processes that drive the broad pat-

terns observed. In this section we discuss our methods for reliably determining these key variables by making use of the unique combination of spectroscopy and near-IR imaging offered by the DEEP2/Palomar survey described above. The uncertainties discussed below refer to the primary sample. Our full error analysis is described in §4.4.1.

4.3.1 Stellar Masses Estimates

The stellar mass estimator used in this work was described thoroughly in Chapter 2, but we repeat some of the key points here. Briefly, the code uses $BRIK$ colors (measured using $2\farcs0$ diameter aperture photometry matched to the K-band detections) and spectroscopic redshifts to compare the observed SED of a sample galaxy to a grid of 13440 synthetic SEDs (from Bruzual & Charlot 2003) spanning a range of star formation histories (parametrized as an exponential), ages, metallicities, and dust content. The J-band photometry was included in the fits where available. The K_s-band M_*/L_K, minimum χ^2, and the probability that the model accurately describes a given galaxy is calculated at each grid point. The corresponding stellar mass is then determined by scaling M_*/L_K ratios to the K_s-band luminosity based on the total K_s-band magnitude and redshift of the observed galaxy. The probabilities are then summed (marginalized) across the grid and binned by model stellar mass, yielding a stellar mass probability distribution for each sample galaxy. We use the median of the distribution as the best estimate.

Photometric errors enter the analysis by determining how well the template SEDs can be constrained by the data. Additional uncertainties in the K_s-band luminosity (from errors in the observed total K_s-band magnitude) lead to final stellar mass estimates that are typically good to 0.2–0.3 dex. The largest systematic source of error comes from the assumed IMF, in this case that proposed by Chabrier (2003). The stellar masses we derive using this IMF can be converted to Salpeter by adding 0.3 dex.

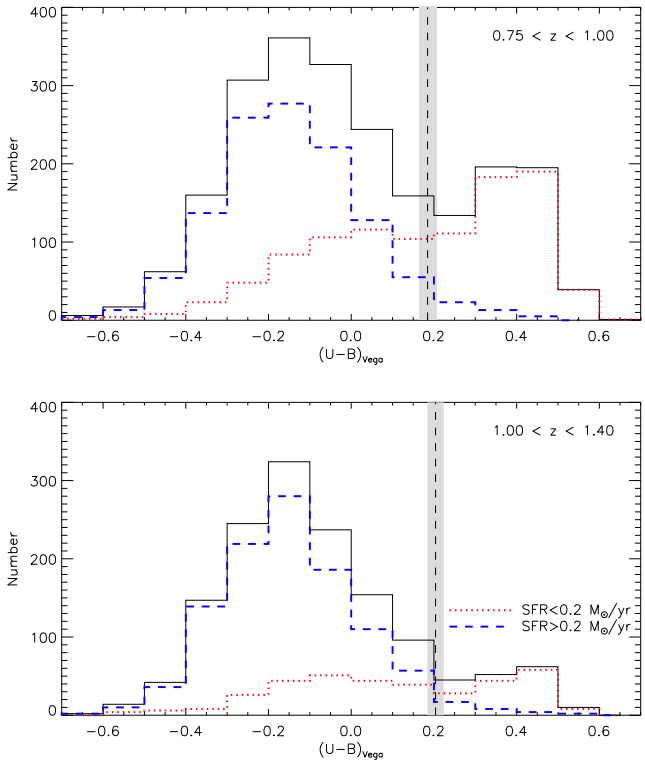

Figure 4.1 The restframe $(U-B)$ color distribution in the middle and high redshift bins. Overplotted are the distributions of galaxies whose star formation rate as derived from the [OII] equivalent width is greater than 0.2 $M_{\odot}$/yr (blue dashed line) and less than 0.2 $M_{\odot}$/yr (red dotted line). The $(U-B)$ bimodality discriminant and its 1σ scatter is indicated by the vertical dashed line and grey shading.

4.3.2 Indicators of Star Formation Activity

In this study we adopt two independent approaches for identifying those galaxies that are undergoing, or have recently experienced, active star formation. The first is the restframe $(U-B)$ color, estimated with the same methods as in Willmer et al. (2005) and based on the IMCAT photometry measured for the CFHT BRI data. The k-corrections which translate observed BRI colors into restframe $(U-B)$ values are determined by comparison to a set of 43 nearby galaxy SEDs from Kinney et al. (1996). Second-order polynomials were used to estimate $(U-B)$ and k-corrections as a function of observed color. Appendix A in Willmer et al. (2005) provides more details on this technique.

The $(U-B)$ color distribution exhibits a clear bimodality that is used to divide

our sample into "Blue" (late-type) and "Red" (early-type) subsamples using the same luminosity-dependent color cut employed by van Dokkum et al. (2000):

$$U - B = -0.032(M_B + 21.52) + 0.454 - 0.25 \ . \tag{4.1}$$

This formula, defined in the Vega magnitude system, divides the sample well at all redshifts (see Figure 4.1), and so we do not apply a correction for potential restframe evolution with redshift (Willmer et al. 2005). We note that the proportion of red galaxies at high-z in Figure 4.1 is in part suppressed by the R-band selection limit of $R_{AB} = 24.1$ (selection effects are discussed in detail in §4.4.2).

For galaxies with $z > 0.75$, the [OII] 3727 Å emission line falls within the spectroscopic range probed by the DEEP2 survey, and this can be used to provide a second, independent estimate of the SFR. For these galaxies, we measure the intensity of the [OII] emission line by fitting a double Gaussian—with the wavelength ratio constrained to that of the [OII] doublet—using a non-linear least squares minimization. We measure a robust estimate of the continuum by taking the biweight of the spectra in two wavelength windows each 80 Å long and separated from the emission line by 20 Å. We consider only spectra where the equivalent width of the feature is detected with greater than 3σ confidence.

Because the DEEP2 spectra are not flux calibrated, we use the following formula from Guzman et al. (1997) to estimate the [OII] SFR:

$$\mathrm{SFR}(\mathrm{M}_\odot\ \mathrm{yr}^{-1}) \approx 10^{-11.6-0.4(M_B - M_{B\odot})}\mathrm{EW}_{[\mathrm{OII}]} \tag{4.2}$$

This relation utilizes the restframe M_B estimated in the same way as the $(U - B)$ colors (see Willmer et al. 2005) and provides an approximate value for the SFR without correcting for metallicity effects which can introduce random and systematic errors of at least 0.3–0.5 dex in the SFR derived from $\mathrm{L}_{[\mathrm{OII}]}$ (Kewley et al. 2004). In addition, Equation 4.2 was optimized for a sample of compact emission line galaxies (see Guzman et al. 1997) which likely differs in the amount of extinction and typical [OII]/Hα ratio compared to the sample here, yielding SFR estimates that could be

systematically off by a factor of ∼3. Moreover, recent work by Papovich et al. (2005) demonstrates that SFR's based on re-radiated IR radiation can be orders of magnitude larger than optical/UV estimates, and studies of the AGN population in DEEP2 indicate that [OII] emission is often associated with AGN, further biasing [OII]-based SFR estimates (Yan et al., in preparation). Future efforts, especially those utilizing the multi-wavelength data set in the EGS, will be useful in refining the SFR estimates. In the present work we accept the limitations of Equation 4.2 for determining absolute SFR's, noting that our primary requirement is not a precision estimate of the SFR for each galaxy but only the broad division of the field population into active and quiescent subsets.

In support of this last point, Figure 4.1 compares the $(U - B)$ and [OII] star formation indicators directly in the two higher redshift bins where both diagnostics are available. The solid histogram traces the full $(U-B)$ distribution with the vertical dashed line (and shading) indicating the median and 1σ scatter of the color bimodality discriminant (Equation 4.1). Using the independent diagnostic of the [OII] equivalent width, we can similarly divide the population into high (blue dashed histogram) and low (red dotted histogram) star-forming populations using a cut of $\mathrm{SFR}_{[\mathrm{OII}]} = 0.2$ $\mathrm{M}_{\odot}$ yr^{-1}, which is the median SFR of galaxies with $0.75 < z < 1.0$. Figure 4.1 clearly shows the effectiveness of the $(U - B)$ color cut in distinguishing the populations in both cases. The fraction of red galaxies in the high $\mathrm{SFR}_{[\mathrm{OII}]}$ population is less than 8% in the middle redshift bin and less than 17% in the high-z bin. The fact that a non-zero fraction of blue galaxies is made up of the low $\mathrm{SFR}_{[\mathrm{OII}]}$ population is likely indicative of the 1–2 Gyr timescale required for galaxies to join the red sequence and suggests that even minor episodes of star formation can lead to blue restframe colors (Gebhardt et al. 2003). In addition, the median value of the measured [OII] SFR increases in the high-z bin. This means that galaxies satisfying the $\mathrm{SFR}_{[\mathrm{OII}]} = 0.2$ $\mathrm{M}_{\odot}$ yr^{-1} cut at high redshift are more vigorously forming stars and are therefore bluer.

Further details on the evolving SFR will be presented in Noeske et al. (in preparation). We also note that the $(U-B)$ and [OII] star formation indicators are consistent

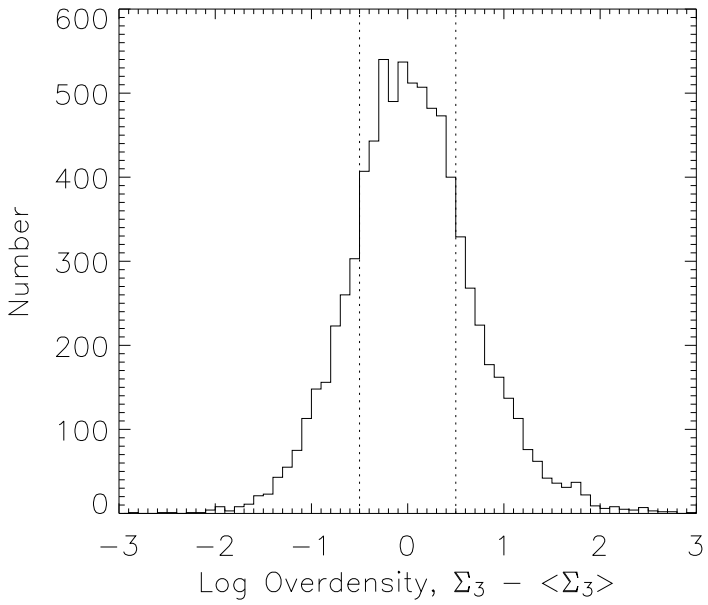

Figure 4.2 The distribution in the relative overdensity in log units as measured across the sample by the 3^{rd}-nearest-neighbor statistic introduced by Cooper et al. (2005). The vertical dotted lines at ± 0.5 dex divide the distribution into low, middle, and high density regimes (see text for details).

with the star formation histories recovered by the SED template fitting procedure used to refine stellar mass estimates and described in §4.3.1. This agreement is expected because the restframe color and SED fitting are both determined by the observed colors. Such consistency demonstrates that the measured physical properties that we use to divide the galaxy population are also reflected in the best-fit SED templates that determine stellar mass (see §4.3.1).

4.3.3 Environmental Density

Charting galaxy evolution over a range of environments represents a key step forward that can only be achieved through large spectroscopic redshift surveys such as in the DEEP2 survey. Cooper et al. (2005) rigorously investigate the question of how to provide precise environmental density estimates in the context of redshift surveys at $z \sim 1$. That work clearly shows, via comparisons to simulated samples, that large samples with photo-zs are very poorly suited to providing accurate density measures.

Specifically, Cooper et al. (2005) find that for environmental studies at high-z, the projected n^{th}-nearest-neighbor distance, $D_{p,n}$, offers the highest accuracy over the greatest range of environments. This measure is the field counterpart to projected density estimates first applied to studies of cluster environments (e.g., Dressler 1980). The statistic is defined within a velocity window ($\Delta v = \pm 1000$ km s^{-1}) used to exclude contaminating foreground and background galaxies. It is therefore particularly robust to redshift space distortions in high density environments without suffering in accuracy in underdense environments. In addition, the effect of survey boundaries on $D_{p,n}$ is easily understood and mitigated by excluding a small strip around survey edges.

In this work we utilize the projected 3^{rd}-nearest-neighbor distance, $D_{p,3}$, excluding galaxies closer than 1 h^{-1} Mpc ($\sim 3'$) from a survey boundary. The choice of $n = 3$ does not significantly affect $D_{p,n}$, which has a weak dependence on n in both high and low density environments for $n < 5$ (Cooper et al. 2005). The effects of survey target selection must be carefully considered because they can introduce biases as a function of redshift. Cooper et al. (2005) find that the sampling rate in the DEEP2 survey equally probes all environments at $z \sim 1$ in a uniform fashion. Although the DEEP2 survey secures redshifts for roughly 50% of galaxies at $z \sim 1$, its sparse selection algorithm does not introduce a significant environment-dependent bias. However, the absolute value of $D_{p,3}$ will increasingly underestimate the true density with increasing redshift as the sampling rate declines. To handle this effect, we first convert $D_{p,3}$ into a projected surface density, Σ_3, using $\Sigma_3 = 3/(\pi D_{p,3}^2)$. We then calculate the *relative* overdensity at the location of each galaxy by subtracting the observed value of Σ_3 by the median surface density calculated in bins of $\Delta z = 0.04$. The relative overdensity is thus insensitive to the DEEP2 sampling rate, providing a reliable statistic that can be compared across the full redshift range of the sample. The typical uncertainty in the measurement of the relative overdensity is a factor of ~ 3. Further details are provided in Cooper et al. (2006).

The distribution of the relative overdensity for our primary sample is plotted in Figure 4.2. In the analysis that follows, we consider two ways of dividing the sample

by environmental density. In the first, we separate galaxies according to whether they lie in regions above or below the median density (corresponding to a measured overdensity of zero in Figure 4.2). This is the simplest criterion but does mean the bulk of the signal is coming from regions which are not too dissimilar in their environs. In the second approach, we divide the density sample into three bins as indicated by the vertical dotted lines in Figure 4.2. The thresholds of 0.5 dex, or 0.77σ, above and below the median density were chosen to select the extreme ends of the density distribution where the field sample begins to probe cluster and void-like environments that are 10–100 times more or less dense than average. The conclusions presented in §4.5 are not sensitive to the precise location of these three thresholds.

4.4 Constructing the Galaxy Stellar Mass Function

The DEEP2/Palomar survey presents a unique data set for constraining the galaxy stellar mass function at $z \sim 1$. Previous efforts have so far relied on smaller and more limited samples, often without spectroscopic redshifts. The K20 Survey (Fontana et al. 2004) used mostly spectroscopic redshifts (92%) but was a factor of 10 smaller in sample size. The MUNICS study (Drory et al. 2004a) relies mostly on photo-zs, spans roughly half the surveyed area, and has a K-band limit roughly 1 magnitude brighter than the sample presented here. The mass functions in Bundy et al. (2005a) utilize data with similar K-band limits and spectroscopic completeness, but probe an area 10 times smaller than the current sample. Only via the combination of size, spectroscopic completeness, and depth does the current sample enable us to study the evolving relationships between stellar mass, star formation activity, and local environment in a statistically robust way. Our primary tool in this effort is charting the galaxy stellar mass function of various populations.

Deriving the stellar mass function in a magnitude-limited survey requires corrections for the fact that faint galaxies are not detected throughout the entire survey

volume. The V_{max} formalism (Schmidt 1968) is the simplest technique for handling this problem but does not account for density inhomogeneities that can bias the shape of the derived mass function. While other techniques address this problem (for a review see Willmer 1997), they suffer from other uncertainties such as the total normalization. For sufficiently large samples over significant cosmological volumes, density inhomogeneities cancel out and the V_{max} method produces reliable results. Considering this and the fact that we wish to use our data set to explicitly test for the effects of density inhomogeneities, we adopt the V_{max} approach, which offers a simple way to account for both the R and K_s-band limits of our sample. For each galaxy i in the redshift interval j, the value of V^i_{max} is given by the minimum luminosity distance at which the galaxy would leave the sample, becoming too faint for either the R or K_s-band limit. Formally, we define

$$V^i_{max} = d\Omega_j \int_{z_{low}}^{z_{high}} \frac{dV}{dz} dz, \tag{4.3}$$

where $d\Omega_j$ is the solid angle subtended by the sample defined by the limiting K_s-band magnitude, K^j_{lim}, for the redshift interval j and dV/dz is the comoving volume element. The redshift limits of the integral are

$$z_{high} = \min(z^j_{max}, z^j_{K_{lim}}, z_{R_{lim}}) \quad \text{and} \tag{4.4}$$

$$z_{low} = z^j_{min}, \tag{4.5}$$

where the redshift interval, j, is defined by $[z^j_{min}, z^j_{max}]$, $z^j_{K_{lim}}$ refers to the redshift at which the galaxy would still be detected below the K_s-band limit for that particular redshift interval, and $z_{R_{lim}}$ is the redshift at which the galaxy would no longer satisfy the R-band limit of $R_{AB} \leq 24.1$. We use the SED template fits found by the stellar mass estimator to calculate $z^j_{K_{lim}}$ and $z_{R_{lim}}$, thereby accounting for the k-corrections necessary to compute accurate V_{max} values.

In constructing the V_{max} mass functions, we also weight the spectroscopic sample to account for incompleteness in the target selection and redshift success rate. We

closely follow the method described in Willmer et al. (2005), but add an extra dimension to the reference data cube which stores the number of objects with a given K_s-band magnitude. Thus, for each galaxy i we count the number of objects from the photometric catalog sharing the same bin in the $(B-R)/(R-I)/R_{AB}/K_s$-band parameter space as well as the fraction of these with attempted and successful redshifts. As mentioned in §4.2.1, ≈30% of attempted DEEP2 redshifts are unsuccessful, mostly because of faint, blue galaxies beyond the redshift limit accessible to DEEP2 spectroscopy (Willmer et al. 2005). Failed redshifts for red galaxies are more likely to be within the accessible redshift range but simply lack strong, identifiable features. We therefore use the "optimal" weighting model (Willmer et al. 2005), which accounts for the redshift success rate by assuming that failed redshifts of red galaxies (defined by the $(U-B)$ color bimodality) follow the same distribution as successful ones, while blue galaxies with failed redshifts lie beyond the redshift limit ($z \approx 1.5$) of the sample. The final weights are then based on the probability that a successful redshift would be obtained for a given galaxy. They also account for the selection function applied to the EGS sample to balance the fraction of redshifts above and below $z \approx 0.7$. With the weight, χ_i, calculated in this way, we determine the differential galaxy stellar mass function:

$$\Phi(M_*)dM_* = \sum_i \frac{\chi_i}{V_{max}^i} dM_* \ . \tag{4.6}$$

4.4.1 Uncertainties and Cosmic Variance

To estimate the uncertainty in our mass distribution we must account for several sources of random error and model their combined effect through Monte Carlo simulations. Different error budgets are calculated for the primary spectroscopic and photo-z supplemented samples via 1000 realizations of our data set in which we randomized the expected errors. In both samples we model uncertainties in V_{max} arising from photometric errors and simulate the error on the stellar mass estimates, which, as described in §4.3.1, is typically 0.2 dex and is encoded in the stellar mass probability

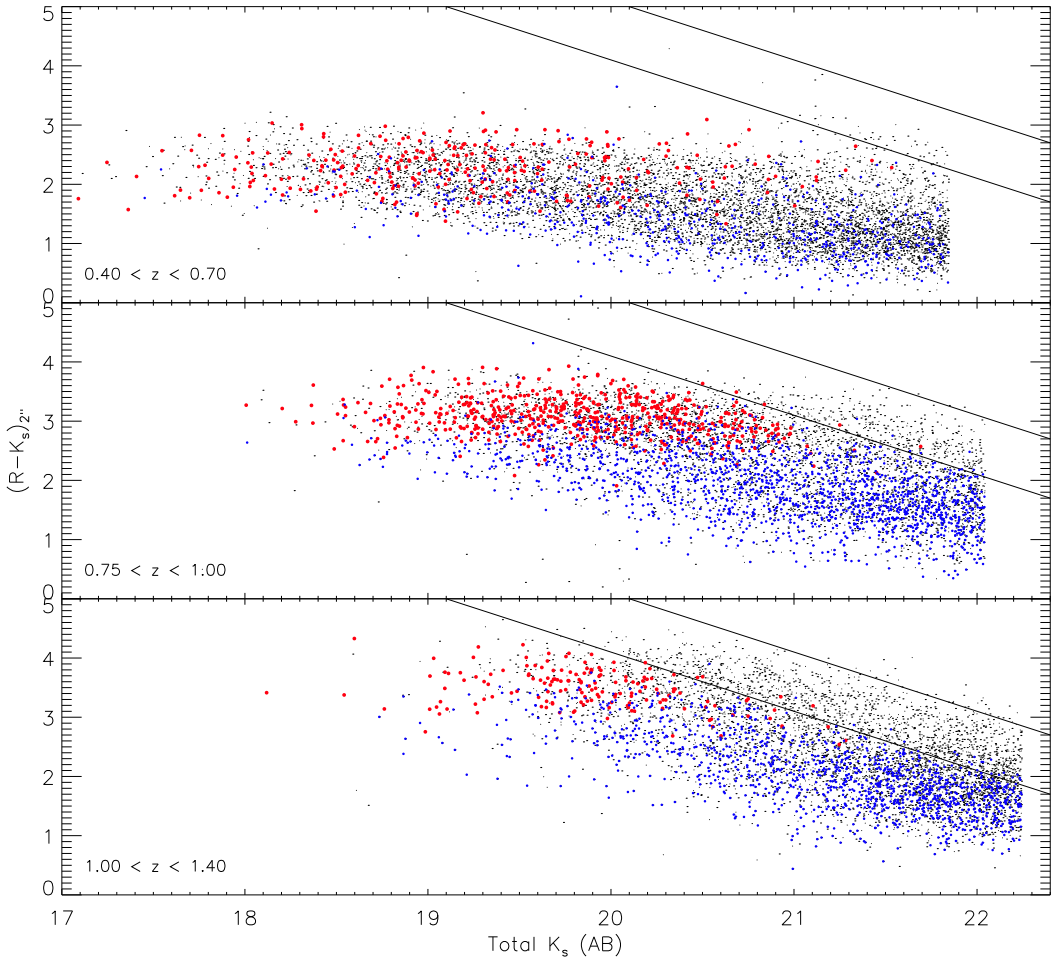

Figure 4.3 Apparent color-magnitude diagrams used to illustrate sample completeness. The plots show the distribution of $(R-K_s)$ vs K_s for the primary spectroscopic redshift sample with $R_{AB} \leq 24.1$ (solid color circles) compared to the $R_{AB} \leq 25.1$ sample, which has been supplemented with photometric redshifts (small black dots). The spectroscopic sample is colored according to location in the bimodal restframe $(U-B)$ distribution as described in the text. The $R_{AB} = 24.1$ and $R_{AB} = 25.1$ magnitude limits are indicated by the solid diagonal lines.

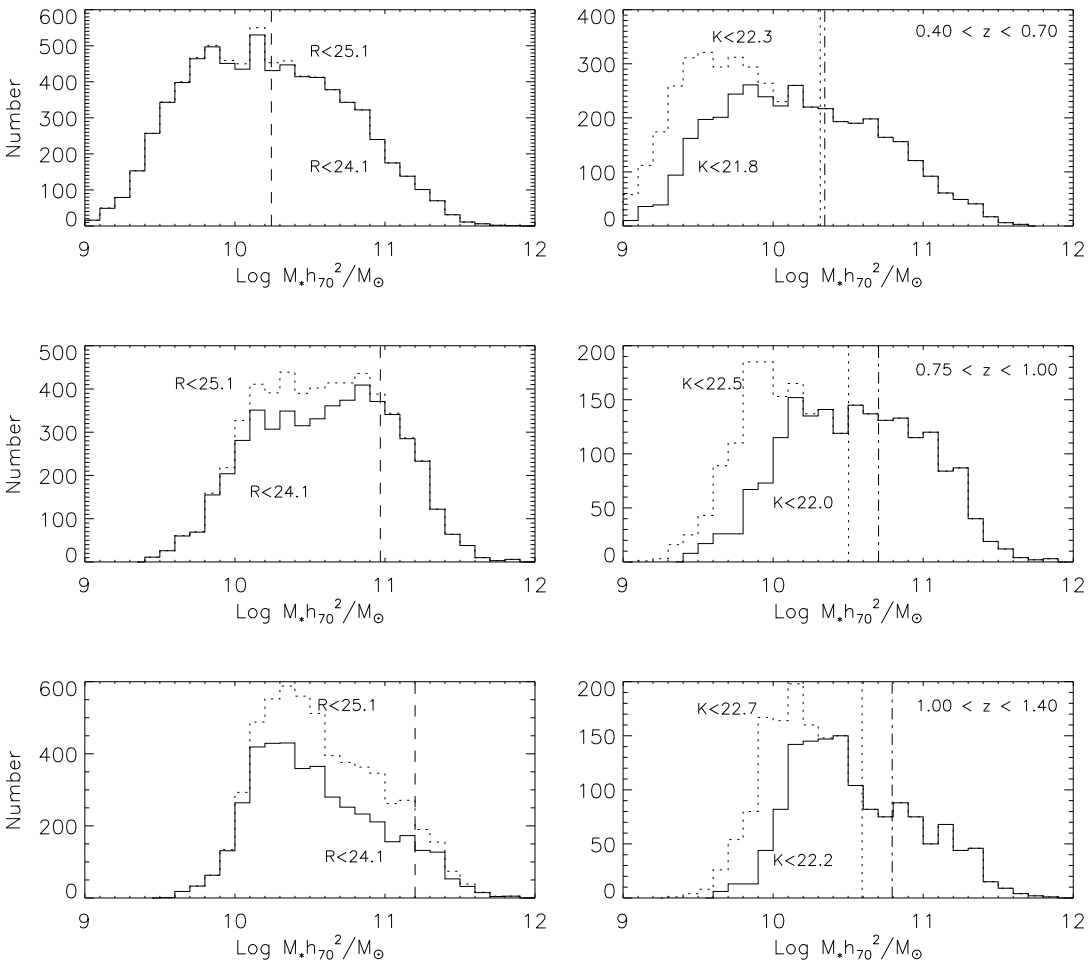

Figure 4.4 Completeness of the mass distribution in the primary spectroscopic sample taking into account the R-band and K_s-band magnitude cuts. The left-hand panels show stellar mass histograms derived from the deeper $R_{AB} \leq 25.1$ photo-z sample (dashed histogram) compared to that restricted to $R_{AB} \leq 24.1$ (solid histogram). Vertical dashed lines indicate the corresponding mass completeness limit for the latter sample. The right-hand panels, also drawn from the $R_{AB} \leq 25.1$ sample, show the effect of a K_s-band limit 0.5 magnitudes fainter than that adopted in a given z-bin (K^j_{lim}). Vertical dash-dot lines designate the model estimate of incompleteness from the K_s-band magnitude limits. The vertical dotted lines show the limits adopted for this analysis.

distribution of each galaxy.

For the primary spectroscopic sample, errors on the restframe $(U-B)$ colors are estimated by noting the photometric errors for a given galaxy. We do not model the uncertainty in the [OII] SFR because unaccounted systematic errors are likely to be greater than the random uncertainty of measurements of the [OII] linewidth. We stress again that these diagnostics are only used to separate the bimodal distribution into active and quiescent components.

For the photo-z supplemented sample, we model redshift uncertainties using $\Delta z/(1+z) = 0.07$ for the $R_{AB} \leq 24.1$ ANNz subsample and $\Delta z/(1+z) = 0.18$ for the $R_{AB} \leq 25.1$ BPZ subsample. The BPZ uncertainty is slightly higher than measured in the comparison to the spectroscopic sample because we expect a poorer precision of BPZ on objects with $R_{AB} > 24.1$. These redshift uncertainties affect the distribution of objects in our redshift bins as well as the Monte Carlo realizations of stellar mass estimates in the photo-z sample. The final uncertainty at each data point in the stellar mass functions from both the spectroscopic and photo-z supplemented samples is determined by the sum, in quadrature, of the 1σ Monte Carlo errors and the Poisson errors.

We now turn to cosmic variance. Because our sample is drawn from four independent fields, it is possible to estimate the effects of cosmic variance by comparing the results from different fields in each of our three redshift bins: $0.4 < z < 0.7$, $0.75 < z < 1.0$, and $1.0 < z < 1.4$. For the spectroscopic sample with $z > 0.75$, we can compare the EGS to the sum of Fields 2, 3, and 4, yielding two subsamples with roughly equal numbers of galaxies. We compare the total and color-dependent stellar mass functions of these two subsamples and divide the median of the differences measured at all data points by $\sqrt{2}$ to estimate the cosmic variance. Unfortunately, galaxies with $z < 0.75$ come only from the EGS. The cosmic variance estimate here is derived by performing the same calculation on three subsets of the EGS sample and dividing it by $\sqrt{3}$. Of course, cosmic variance on the scale of the EGS itself is not included in this estimate. For the three redshift intervals, this method provides 1σ systematic cosmic variance uncertainties of 29%, 12%, and 26%.

In addition to these rough estimates, we have checked that the observed density distribution is not affected by cosmic variance. Based on the density-dependent mass functions from different fields, there is no evidence of a single structure or overdensity in one of the fields that would bias our results. We also note that the type-dependent mass functions are, to first order, affected by cosmic variance in the same way as the total mass functions. Thus, while absolute comparisons between different redshift intervals must account for cosmic variance errors, comparisons using the relative or fractional abundance of a given population are much less susceptible to this uncertainty.

4.4.2 Completeness and Selection Effects

We now turn to the important question of the redshift-dependent completeness of the stellar mass functions in our sample. We adopt two approaches to determine how incompleteness affects this derived quantity.

First, we consider the likelihood of observing model galaxies of known mass and color based on the R and K_s-band magnitude limits of the primary spectroscopic sample. We follow previous work (e.g., Fontana et al. 2003) and track the stellar mass of a template galaxy placed at the leading edge of each redshift interval. We assume it has a reasonable maximum M_*/L ratio determined by models with short bursts of star formation (parametrized by an exponential with $\tau = 0.5$ Gyr at $z_{form} = 2.5$), moderate dust, solar metallicity, and luminosities corresponding to the observed R and K_s-band limiting magnitudes. The maximum stellar masses of these model galaxies provide conservative estimates of our completeness limits and are indicated in Figure 4.4.

Our second approach is to measure the effects of incompleteness directly by comparing our primary spectroscopic sample with $R_{AB} \leq 24.1$ to the fainter sample with $R_{AB} \leq 25.1$, supplemented by photometric redshifts. This approach is particularly useful for investigating the way in which the R-band limit introduces a bias against red galaxies, especially at $z \gtrsim 1$. This bias could mimic the effect of downsizing by

suppressing the fraction of red galaxies at $z \gtrsim 1$. The behavior of model galaxies (described above) as well as the comparison to a fainter sample both yield consistent estimates for the sample completeness, which we will show does not compromise our results.

Figure 4.3 compares the distribution in $2\farcs0$ diameter $(R - K_s)$ vs total K_s color-magnitude space of the primary spectroscopic sample with $R_{AB} \leq 24.1$ (solid color circles) to that for the fainter $R_{AB} \leq 25.1$ sample (small black dots) supplemented with photometric redshifts. As expected, in the low redshift bin, the majority of the $R_{AB} \leq 25.1$ sample is contained within the spectroscopic limit of $R_{AB} = 24.1$ (although the photo-z sample includes many more galaxies with $R_{AB} \leq 24.1$ that were not selected for spectroscopy). At high redshift, however, the primary sample is clearly incomplete, with a substantial number of galaxies having $R_{AB} > 24.1$. While the full range of $(R - K_s)$ colors is included in the primary sample, a color bias is introduced because the reddest galaxies are no longer detected at $K_{AB} \gtrsim 20$.

To demonstrate how this color bias affects the mass completeness of the sample, the left-hand panels in Figure 4.4 compare the stellar mass distribution taken from the photo-z supplemented sample limited to $R_{AB} \leq 24.1$ (solid histogram) with that for the full sample with $R_{AB} \leq 25.1$ (dashed histogram). With increasing redshift, the fraction of galaxies satisfying $R_{AB} \leq 24.1$ decreases. Using the distributions in each redshift interval, the mass completeness of the spectroscopic sample is estimated as that mass above which the brighter sample includes more than ≈90% of the fainter one. This mass completeness estimate, based on photometric redshifts, agrees well with the estimate from the colors and M_*/L-ratios of model galaxies, which are indicated by the vertical dashed lines.

For galaxies with $z < 1.0$, Figure 4.4 indicates that the R-band limit has only a small effect on the spectroscopic sample. Galaxies with $R_{AB} \leq 24.1$ constitute the vast majority of the total distribution in the first two redshift bins, with a minimum completeness of ≈85% in the middle redshift bin. The R-band limit has a greater effect in the high-z bin, where the $R_{AB} \leq 24.1$ distribution accounts for just over ≈50% of the $R_{AB} \leq 25.1$ sample over most of the mass range. In section §4.5, we

correct for this incompleteness and show that it does not affect our conclusions.

The right-hand panels of Figure 4.4 illustrate the effect of the K_s-band limit on the mass completeness of the spectroscopic sample. Using our deepest Palomar observations, we construct stellar mass distributions from the photo-z supplemented sample with $R_{AB} \leq 25.1$. Again, for each redshift interval, we compare the mass distribution of a subsample with a K_s-band limit equal to 0.5 magnitudes fainter than the limit imposed on the spectroscopic sample at that redshift, K^j_{lim}. This is plotted as the dashed histogram in Figure 4.4 and is compared to the same subsample with an imposed limit of K^j_{lim} (solid histogram). As in the left-hand panels of Figure 4.4, the point at which these two histograms diverge yields an estimate of the K_s-band mass completeness limit. In this case, the model estimates (vertical dash-dot lines) appear too conservative in the middle and high redshift bins, suggesting that the K_s-band M/L ratio for the chosen model is more extreme than typical galaxies at this redshift. For the analysis to follow, we conservatively adopt the limits indicated by the dotted lines instead. For each redshift bin, the K_s-band cut introduces incompleteness below masses of 10.1, 10.5, and 10.6 in units of log $M_\odot$.

4.5 Results

4.5.1 The Mass Functions of Blue and Red Galaxies

In Figure 4.5 we present in three redshift intervals the galaxy stellar mass function partitioned into active and quiescent populations according to the bimodality observed in the restframe $(U - B)$ color. The lowest redshift interval draws only from the EGS, while the two higher bins utilize data from all four DEEP2 survey fields. We also plot the stellar mass functions from the deeper, $R_{AB} \leq 25.1$ sample supplemented with photo-zs when spectroscopic redshifts are not available. The vertical dotted lines represent estimates of the mass completeness originating from the K_s-band magnitude limit (see §4.4.2). The width of the shaded curves corresponds to the final 1σ errors using the Monte Carlo techniques discussed earlier.

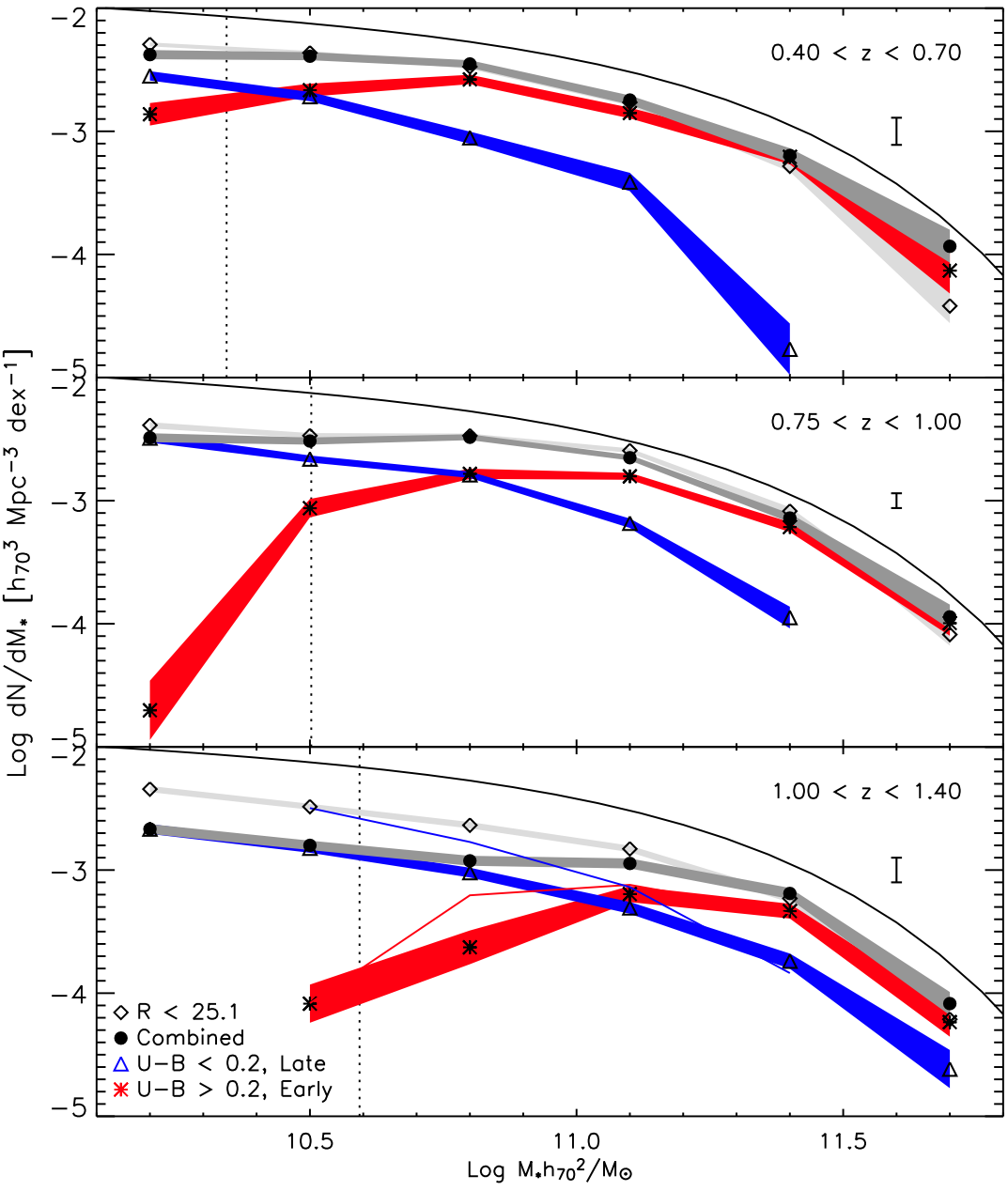

Figure 4.5 Mass functions in three redshift bins partitioned by restframe $(U - B)$ color as described in the text. Shading indicates the width of 1σ error bars. The mass function for all galaxies in the primary spectroscopic sample is designated by solid circles. That for the deeper, $R_{AB} \leq 25.1$ sample, supplemented by photo-zs, is indicated by open diamonds. Vertical dotted lines show estimates for mass incompleteness resulting from the K_s-band magnitude limit. In the high-redshift bin (bottom panel), thin red and blue lines trace the expected increase in the red and blue populations if the spectroscopic limit of $R_{AB} = 24.1$ were extended by one magnitude. The isolated error bar in the upper right-hand portion of each plot indicates the estimated systematic uncertainty due to cosmic variance. The locally measured stellar mass function from Cole et al. (2001) is shown as the solid curve.

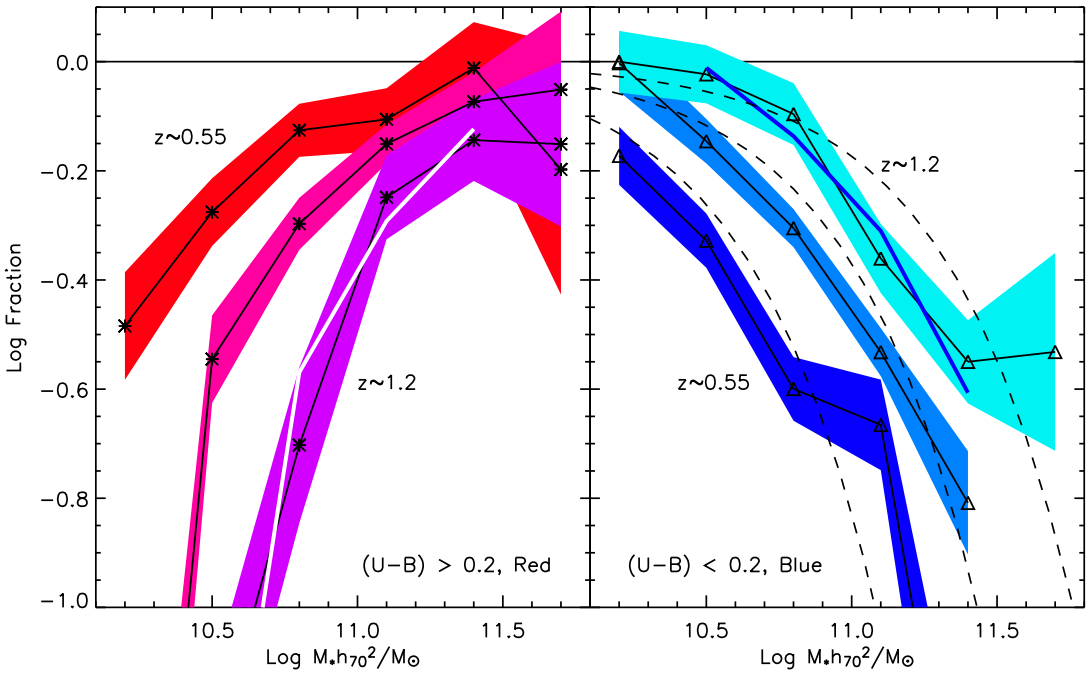

Figure 4.6 Log fractional contribution of the red and blue populations to the total stellar mass function at various redshifts. The relative contribution of red galaxies (left plot) increases with cosmic time, while that for blue galaxies decreases (right plot). The expected high-z fraction of red and blue types after correcting for R-band completeness (as in Figure 4.5) is shown by a thin white line for the red population and a thin blue line for the blue population. The corrected fractions from the $R_{AB} \leq 25.1$ sample are entirely consistent with those observed in the primary $R_{AB} \leq 24.1$ spectroscopic sample. Dashed lines in the right-hand panel show approximate fits to the quenching mass cut-off, as defined by M_Q (see §4.5.3).

As discussed in §4.4.2, the mass functions of the primary sample presented in Figure 4.5 are affected by incompleteness because of the $R_{AB} = 24.1$ spectroscopic limit. The degree of incompleteness is apparent in the comparison between the total mass functions of the spectroscopic and $R_{AB} \leq 25.1$ samples. As expected from Figure 4.4, the first two redshift bins are only mildly affected by R-band incompleteness, but the effect is significant in the high redshift bin where the comoving number density in the deeper sample is larger by a factor of ≈2 (0.3 dex) for $M_* < 10^{10.8}\mathrm{M}_\odot$.

To mitigate this effect we derive a color-dependent completeness correction for the high-z bin based on the photo-z supplemented $R \leq 25.1$ sample. Inferring the restframe $(U - B)$ color for this sample is difficult because of photometric redshift

uncertainties. Instead, we adopt the simpler approach of applying a color cut in observed $(R-K)$, which, as shown in Figure 4.3, maps well onto the restframe $(U-B)$ color for the high-z spectroscopic sample. We tune the $(R-K)$ cut so that the resulting color-dependent mass functions of the $R_{AB} \leq 25.1$ sample match the spectroscopic ($R_{AB} \leq 24.1$) mass functions above $M_* = 10^{11.3}\mathrm{M}_\odot$ where the spectroscopic sample is complete. This yields a value of $(R-K_s)_{2''} = 3.37$, consistent with the $(U-B)$ bimodality apparent in the color-magnitude diagram shown in Figure 4.3.

Using this observed $(R-K)$ color cut for the high-z bin only, we show the color-dependent mass functions for the $R_{AB} \leq 25.1$ sample in Figure 4.5 as thin red and blue lines. While these curves suffer from their own uncertainties, such as photo-z errors and a less precise measure of color, they are useful for illustrating the nature of the R-band incompleteness in the spectroscopic sample. It is important to note that while the deeper sample yields higher mass functions for both the red and blue populations below $M_* \approx 10^{11.1}\mathrm{M}_\odot$, the relative contribution of each one to the total mass function is similar to what is observed in the spectroscopic sample. This is shown more clearly in Figure 4.6. It should also be noted that the $R_{AB} \leq 25.1$ sample itself is not complete, although the decreasing density of points near the $R_{AB} = 25.1$ limit in Figure 4.4 suggests it is largely complete over the range of stellar masses probed.

Figure 4.5 reveals several striking patterns. By comparing to the locally measured galaxy stellar mass function from Cole et al. (2001), reproduced in each redshift bin, it is apparent that the total mass function does not evolve significantly since $z \sim 1.2$. In the high mass bin centered at $\log(M_*/M_\odot) = 11.7$, the total mass function of the spectroscopic sample varies by less than 0.15 dex, or $\sim$40%, which is within the uncertainty from cosmic variance. Meanwhile, a clear trend is observed in which the abundance of massive blue galaxies declines substantially with cosmic time, with the remaining bulk of the actively star-forming population shifting to lower mass galaxies. As the abundance of the blue population declines, red galaxies, which dominate the highest masses at all redshifts, become increasingly prevalent at lower masses. The two populations seem therefore to exchange members so that the total number density

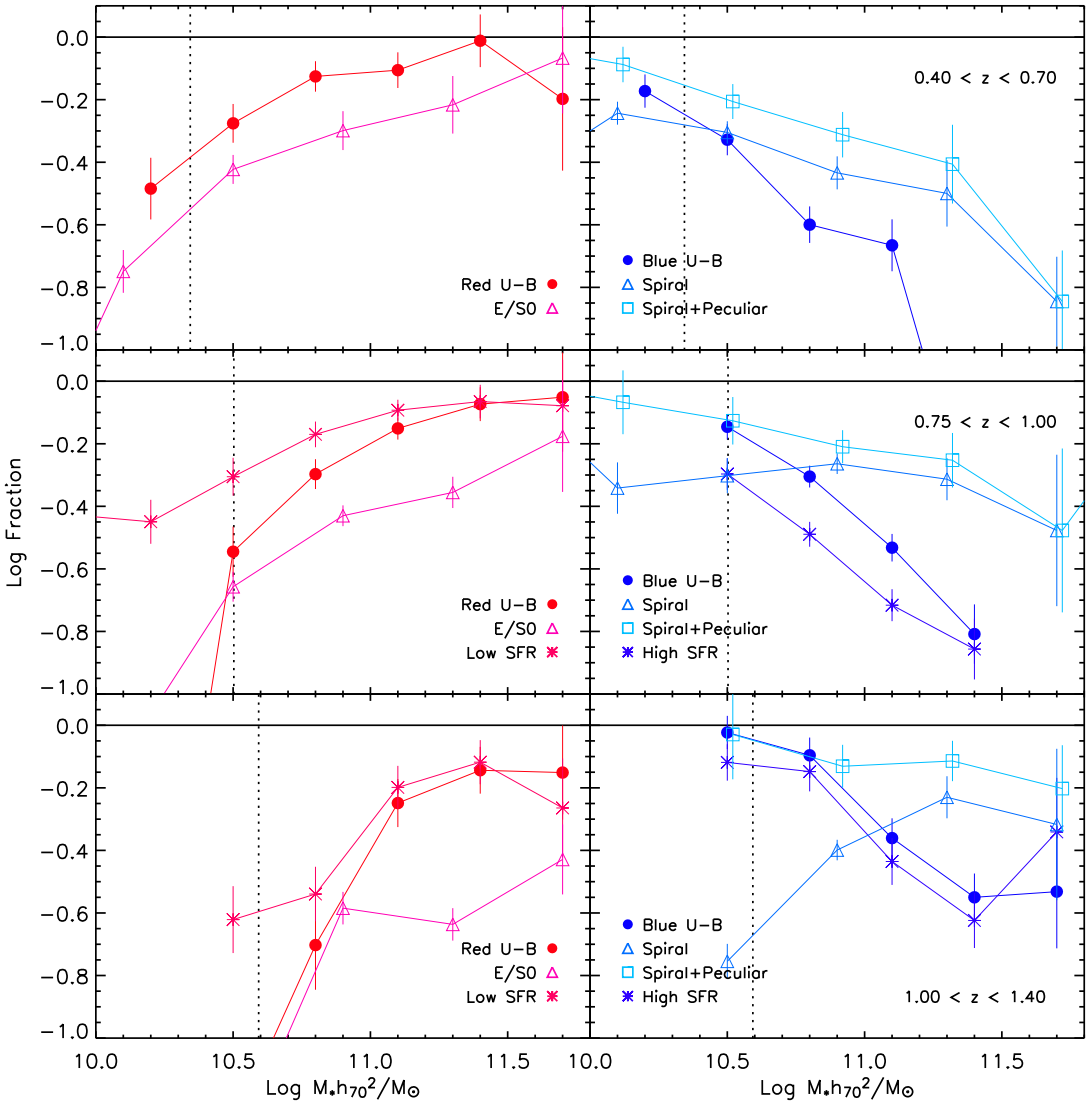

Figure 4.7 Fractional contribution in log units to the total mass function from quiescent (left-hand plots) and active populations (right-hand plots) defined by restframe $(U-B)$ color, [OII] star formation rate, and morphology (see text for details). Star formation rates based on [OII] are only available for galaxies with $z > 0.75$. The morphological mass functions are those of Bundy et al. (2005a). The K_s-band completeness limits are indicated as in Figure 4.5.

of galaxies at a given stellar mass remains fixed. We also note the clear downward evolution of the cross-over, or transitional mass, M_{tr}, where the mass functions of the two color populations intersect. Above M_{tr}, the mass function is composed of primarily red galaxies, and below it, blue galaxies dominate. We return to this behavior in §4.5.3.

Figure 4.6 shows these results in a different way. Here, the log fractional contribution from the red and blue populations are plotted in the same panel so that the redshift evolution is clearer. The completeness-corrected color-dependent mass functions (with $R \leq 25.1$) are shown as the solid red and blue lines. Their overlap with the shaded curves from the high-z spectroscopic sample is remarkable and indicates that unlike absolute quantities, relative comparisons between mass functions drawn from the spectroscopic sample are not strongly biased by the R-band mass completeness limit. As noted previously, plotting the relative fraction also removes the first order systematic uncertainty from cosmic variance, making comparisons across the redshift range more reliable.

The downsizing evolution in Figure 4.5 is now more clearly apparent in Figure 4.6. The relative abundance of red galaxies with $M_* \approx 6 \times 10^{10} \mathrm{M}_\odot$ increases by a factor of ≈6 from $z \sim 1.2$ to $z \sim 0.55$. At the same time, the abundance of blue, late-type galaxies, which are thought to have experienced recent star formation, declines significantly.

4.5.2 Downsizing in Populations Defined by SFR and Morphology

The patterns in Figure 4.5 and 4.6 are also apparent when the galaxy population is partitioned by other indicators of star formation. This is demonstrated in Figure 4.7, which shows the fractional contribution (in log units) of active and quiescent populations to the total mass function. The "blue" and "red" samples defined by restframe $(U - B)$ color and shown in Figure 4.5 are reproduced here and indicated by solid circles.

For the two redshift intervals with $z > 0.75$, we have plotted contributions from samples with high and low [OII]-derived SFRs. We divide this sample at 0.2 $M_\odot$ yr^{-1}, which is the median SFR of the star-forming population at $0.75 < z < 1.0$. This imposes a more stringent criterion than the restframe $(U-B)$ cut, which counts galaxies with only moderate or even recent star formation as "late-type." Not surprisingly, the middle redshift bin contains fewer high-SFR galaxies compared to blue $(U-B)$ systems and more low-SFR galaxies than red systems, although the mass-dependence observed with either criterion is qualitatively similar.

In the high-z bin, the populations defined by color and [OII] track each other more closely. Not only does this confirm that the mass-dependent evolution seen in Figure 4.5 is reproduced when the sample is divided by the [OII] SFR, but it also indicates that the average star formation rate is *higher* in this redshift bin. More of the "blue" population is now above the SFR cut as compared to the middle redshift bin. This evolution in the observed SFR will be discussed in detail in Noeske et al. (in preparation).

It is helpful also to understand how these trends relate to early work motivated by understanding the role of morphology in downsizing. Figure 4.7 also plots the contribution from morphologically-defined populations, drawing from the sample of Bundy et al. (2005a), which has been adjusted to the $h = 0.7$ cosmology used here (we note that the recent addition of HST/ACS imaging in the EGS provides an opportunity to extend this morphological comparison in the future). In Bundy et al. (2005a), morphologies were determined visually using HST/ACS imaging data from the GOODS fields (Giavalisco et al. 2004) and were divided into three broad classes: E/S0, spirals, and peculiars. The fractional contribution from the spiral and spiral+peculiar samples are plotted in Figure 4.7 for comparison to the late-type populations described above. The E/S0 fraction is compared to the early-types. It should be noted that the smaller sample size of the Bundy et al. (2005a) data leads to greater uncertainties and larger effects from cosmic variance.

With these caveats, there is quite good agreement in the mass-dependent evolutionary trends between the morphological and color/SFR selected samples. In detail,

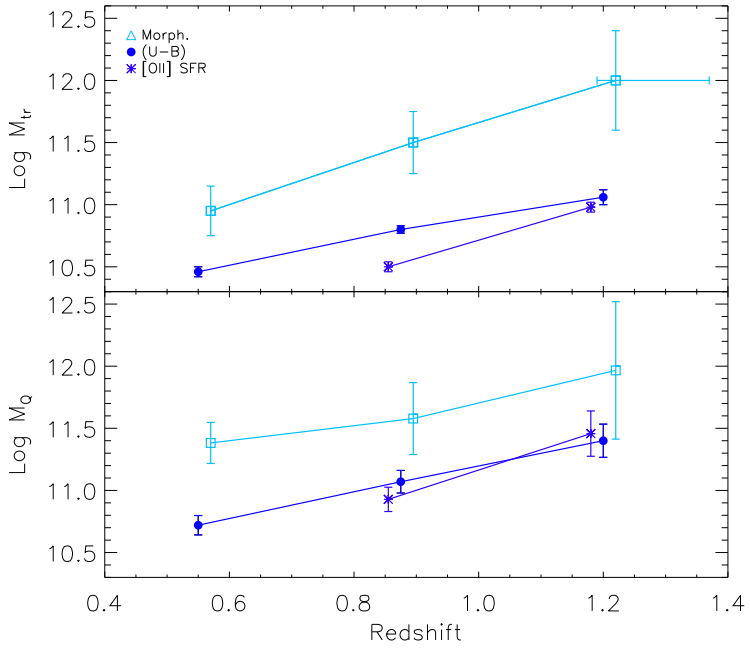

Figure 4.8 Redshift evolution of the characteristic transitional mass, M_{tr} (top plot), as well as the quenching mass, M_Q (bottom plot). In both plots, the observed behavior is shown for the population partitioned according to morphology (light, open squares), restframe $(U-B)$ color (solid circles), and [OII] SFR (asterisks).

the fraction of ellipticals is systematically lower than the red/low-SFR populations while the fraction of spirals+peculiars is systematically higher than the blue/high-SFR galaxies. This suggests that the process that quenches star formation and transforms late-types into early-types operates on a longer timescale for morphology than it does for color or SFR. We return to this point in §4.6. We also note that spiral galaxies do not always exhibit star formation and can be reddened by dust, while some ellipticals have experienced recent star formation (e.g., Treu et al. 2005a) that could lead to bluer colors.

4.5.3 Quantifying Downsizing: the Quenching Mass Threshold, M_Q

Several authors have identified a characteristic transition mass, M_{tr}, which divides the galaxy stellar mass function into a high-mass regime in which early-type, quiescent

galaxies are dominant and a low-mass regime in which late-type, active galaxies are dominant (e.g., Kauffmann et al. 2003b; Baldry et al. 2004; Bundy et al. 2005a). Using our various criteria, the downward evolution of this transitional mass with time is clearly demonstrated in the upper panel of Figure 4.8. The morphological sample is taken from Bundy et al. (2005a), where we have grouped spirals and peculiars into one star-forming population and compared its evolution to E/S0s. In the high-z bin, M_{tr} for the morphological sample occurs beyond the probed stellar mass range, and so we have extrapolated to higher masses to estimate its value (this uncertainty is reflected in the horizontal error bar at this data point).

The color-defined M_{tr} shows a redshift dependence of $M_{tr} \propto (1+z)^4$, similar to that for the morphological sample. Stronger evolution is seen for the the [OII]-defined samples as expected if evolution is more rapid for the most active sources. As discussed in §4.5.2, the mass scale of morphological evolution is approximately 3 times larger (≈0.5 dex) than that defined by color or [OII]. We also note from Figure 4.5 that M_{tr} does not change appreciably when the R-band mass incompleteness is corrected in the high-z bin.

While the evolution in M_{tr} is illustrative of downsizing, since its definition is completely arbitrary (equality in the relative mass contributions of two populations), its physical significance is not clear. We prefer to seek a quantity that clearly describes the physical evolution taking place. Accordingly, we introduce and define a *quenching mass limit*, M_Q, as that mass above which star formation is suppressed in galaxies. This threshold is a direct byproduct of the mechanism that drives downsizing. We consider an additional exponential cut-off applied to the Schechter function, describing the total mass function, whose shape reflects the decline in the fraction of star-forming galaxies (Figure 4.6) and is defined by

$$\Phi_{late} = \Phi_{total} \times \exp\left(M_*/M_Q\right) . \tag{4.7}$$

The resulting fitted values of M_Q are plotted in the bottom panel of Figure 4.8 and listed in Table 4.2. The relative behavior of differently classified populations is

Table 4.2. The Quenching Mass Threshold, M_Q

Redshift	Blue $(U-B)$	High SFR	Spirals+Peculiars
$0.4 < z < 0.7$	10.72 ± 0.08	—	11.38 ± 0.16
$0.75 < z < 1.0$	11.07 ± 0.09	10.93 ± 0.10	11.58 ± 0.29
$1.0 < z < 1.4$	11.40 ± 0.13	11.46 ± 0.18	11.97 ± 0.55

Note. — M_Q is given in units of $\log(Mh_{70}^2/M_\odot)$. Morphology data comes from Bundy et al. (2005a).

similar to the top panel, but the physical mass scale associated with M_Q is a factor of 2–3 higher than that of M_{tr}. We find an approximate redshift dependence of $M_Q \propto (z+1)^{4.5}$, similar to the dependence of M_{tr}.

M_Q is a useful quantity because it reveals the masses at which quenching operates effectively as a function of redshift. As we discuss below, its quantitative evolution strongly constrains what mechanism or mechanisms quench star formation and also provides a convenient metric for testing galaxy formation models.

4.5.4 The Environmental Dependence of Downsizing

We have so far considered the mass-dependent evolution of late- and early-type populations integrated over the full range of environments probed by the DEEP2 Redshift Survey. We now divide the sample by environmental density to investigate how this evolution depends on the local environment.

In Figure 4.9 we plot galaxy stellar mass functions for the samples shown in Figure 4.5, split into low-density environments on the left-hand side and high-density environments on the right-hand side. The density discriminant is simply the median density (indicated by an overdensity of zero in Figure 4.2), so all galaxies are included. We find only small differences in the combined mass functions. The high density mass functions contain more massive galaxies by roughly a factor of 2, but exhibit little evolution with redshift as seen in Figure 4.5. Crucially, the relative contribution of

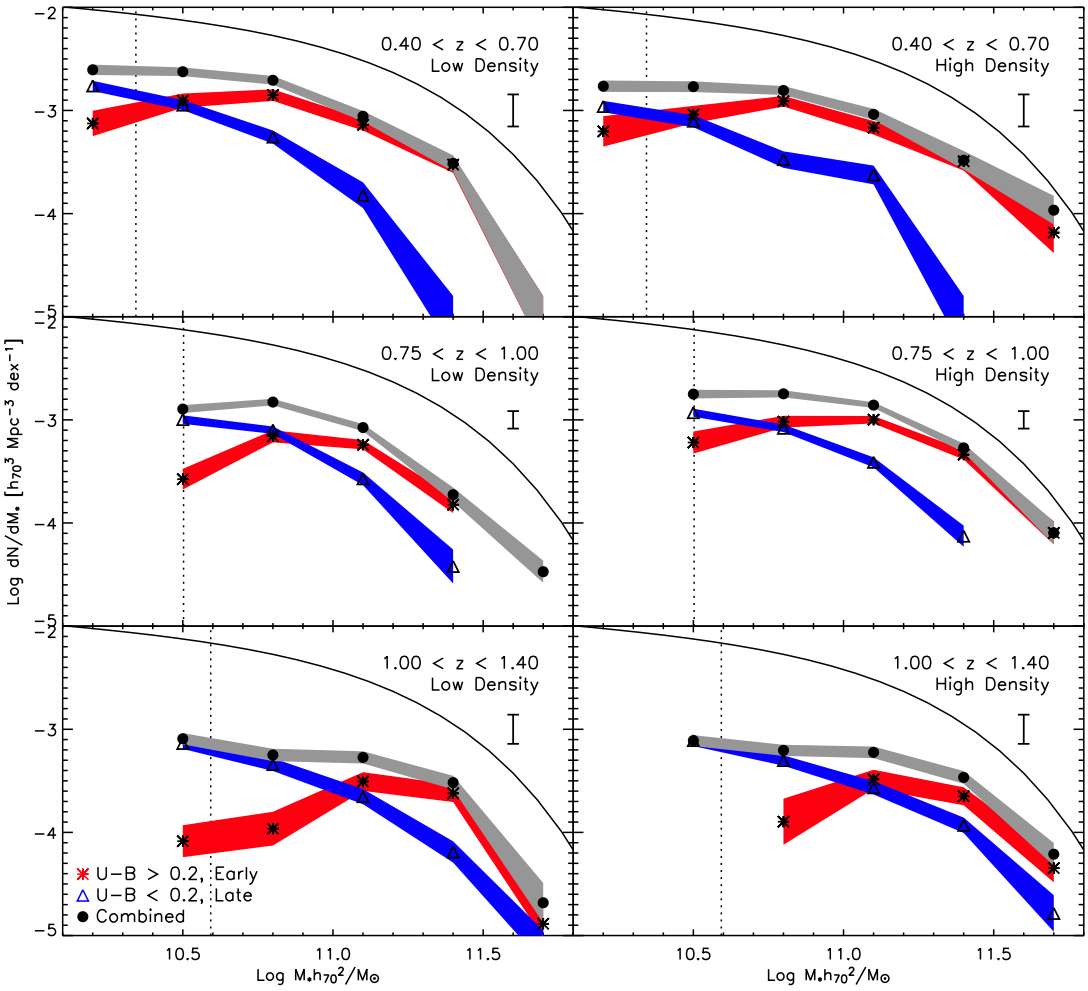

Figure 4.9 Stellar mass functions in the three redshift bins at above- and below-average density partitioned by restframe $(U - B)$ color. The vertical dotted lines show the K_s-band magnitude completeness limits. The estimated cosmic variance is designated by the isolated error bar. Significant incompleteness from the R-band limit is expected in the high redshift bin, but it is not possible to apply corrections as in Figure 4.5 because the local density can only be measured in the spectroscopic sample. The locally measured stellar mass function from Cole et al. (2001) is shown as the solid curve.

active and quiescent galaxies follows the same mass-dependent trends as for the earlier analyses.

The absence of a strong environmental trend in the downsizing pattern of massive galaxies is a surprising result that warrants further scrutiny. Although no strong dependence was seen in the Fundamental Plane analysis of Treu et al (2005), their density estimates were much coarser and based on photometric redshifts. Since our comparison above is inevitably dominated by galaxies near the median density (Figure 4.2), we adopt a second, more stringent approach that divides the distribution into three, more extreme density bins. In this way, we can sample the full dynamic range of our large survey. As described in §4.3.3, we define a second set of density thresholds at ± 0.5 dex from the median density and construct mass functions for the extreme high- and low-density regimes. We plot the results in Figure 4.10, which again shows the fractional contribution of the red and blue populations to the total mass function. This time the samples are also divided by density, with the high density points connected by solid lines and the low density points connected by dotted lines.

Figure 4.10 illustrates a modest environmental effect in the mass-dependent evolution in the low and middle redshift bins, whereas in the high-z bin no statistically-significant trend is seen. In the two lower bins, the rise of the quiescent population and the evolution of M_{tr} appears to be accelerated in regions of high environmental density. This effect does not depend on the particular choice of the density threshold, although the differences between the two environments grow as more of the sample near the median density is excluded from the analysis. The difference in M_{tr} between these two environments is roughly a factor of 2–3. We caution that interpreting the results in the high-z bin is difficult because the effects of completeness and the importance of weighting are most important here. However, the lack of a trend in high-z bin suggests that the structural development that leads to the density dependence at lower redshift does not begin until after $z \sim 1$.

The environmental dependence observed in Figure 4.10 is not dominated by the high-density regime, as one might expect given the potential presence of dense structures in the sample. The environmental effect is less strong but still apparent in

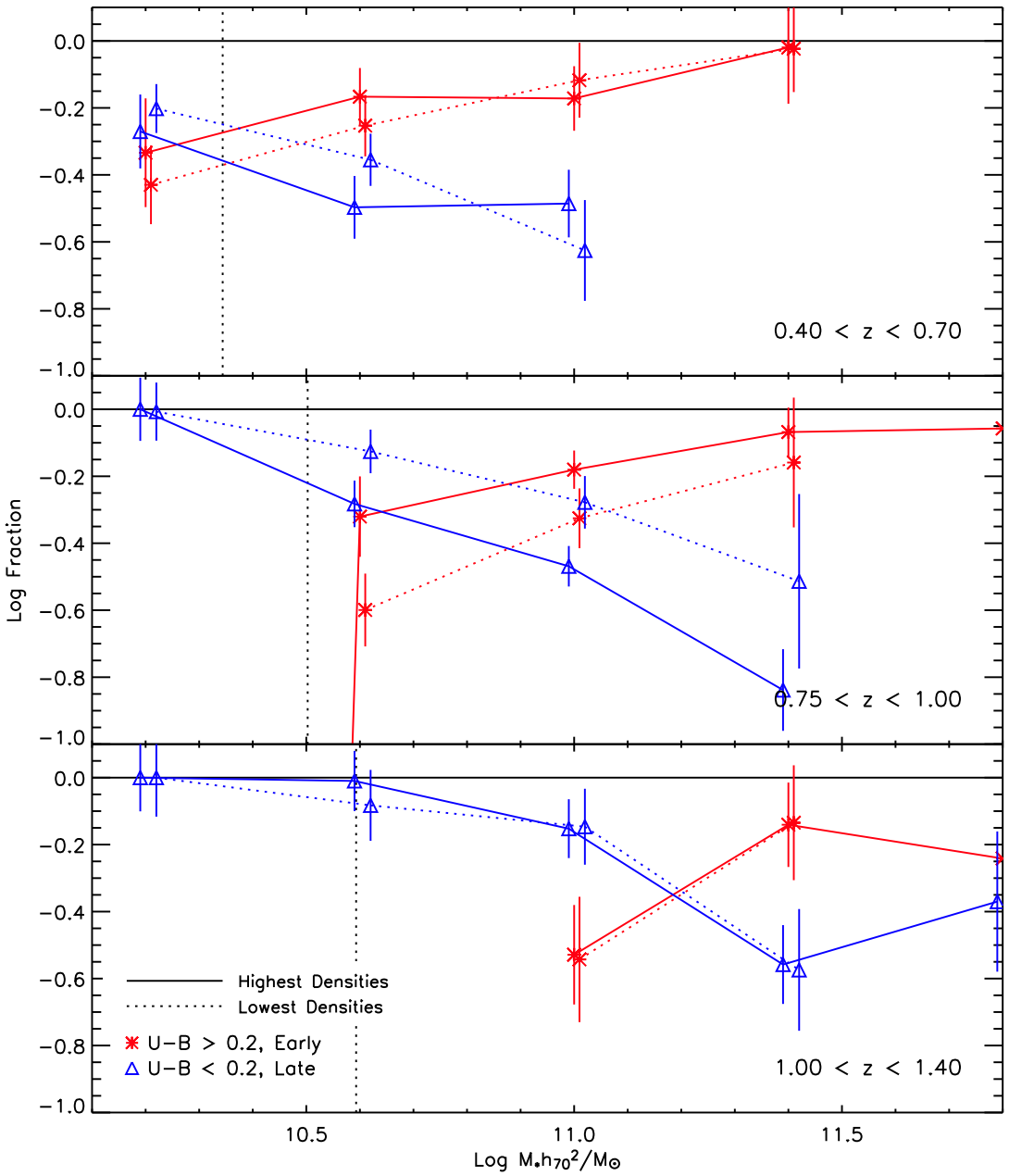

Figure 4.10 Fractional contribution in log units to the total mass function. In each of three redshift bins solid lines connect points representing the extreme high-end of the density distribution, while dotted lines indicate the extreme low-end. The K_s-band completeness limits are indicated as in Figure 4.9.

comparisons between the high and middle density regimes as well as between the middle and low density regimes (there is also evidence for the effect in the middle-z bin in Figure 4.9).

In summary, our various measures of downsizing, M_{tr} and M_Q, depend strongly on redshift but weakly on environmental density. The latter result is particularly striking and serves to emphasize that galaxy mass, not environmental location, is the primary parameter governing the suppression of star formation and, hence, producing the signature of downsizing.

4.6 Discussion

4.6.1 The Rise of Massive Quiescent Galaxies

Figures 4.5 and 4.7 demonstrate a clear feature of the downsizing signal observed since $z \sim 1$, namely the increase in the number density of massive quiescent galaxies. Although our results are consistent with previous studies which found a rise in the red galaxy abundance of a factor of $\approx$2–6 depending on mass (Bell et al. 2004), the present work represents a significant step forward not only in its statistical significance and precision by virtue of access to the large spectroscopic and infrared data set, but also in clearly defining the mass-dependent trends.

In discussing our results we begin by considering the processes that might explain the present-day population of early-type galaxies. In order to reconcile the significant ages of their stellar populations implied by precise Fundamental Plane studies (e.g., Treu et al. 2005a; van der Wel et al. 2005) with hierarchical models of structure formation, Bell et al. (2005a), Faber et al. (2005), van Dokkum (2005), and others have introduced the interesting possibility of "dry mergers"—assembly preferentially progressing via mergers of quiescent sub-units.

While dry mergers clearly occur (Tran et al. 2005; van Dokkum 2005), our results suggest that they cannot be a substantial ingredient in the assembly history of massive quiescent galaxies. As shown in Figure 4.5, the observed increase in the number of

quiescent systems is almost perfectly mirrored by a decline in star-forming galaxies such that the total mass function exhibits little evolution overall for $0.4 < z < 1.4$. A simple transformation of one into the other is sufficient to high precision. For example, simply interchanging the numbers of red and blue galaxies in the high-z bin in the mass range $10^{11.2} < \log M_*/M_\odot < 10^{11.8}$ leads to a prediction for the number density in the middle-z bin that is accurate to within $\sim$25%, well within the cosmic variance uncertainty.

It is conceivable that the dry merger rate is mass-dependent and conspires to move galaxies along the mass function in a way that leaves its shape preserved. This would imply the presence of massive galaxies at low redshift that are not seen in our sample. For example, using the approximate dry merger rate estimate from Bell et al. (2005a) of 1.3 mergers every 6.3 Gyr, $\sim$25% of red galaxies would have to experience a major dry merger (in reality, this rate, calculated over $0 < z < 0.7$, might be expected to be higher at $z \sim 1$) between the high-z and middle-z bins. If we apply this rate of assembly to the red population in our high-z bin at $\log(M_*/M_\odot) = 11.4$, we find that the total mass function in the middle-z bin at $\log(M_*/M_\odot) = 11.7$ should be higher by approximately 30% compared to what is observed. While this one data point represents only a $\approx 1.4\sigma$ result, similar arguments apply across the mass function and between the middle-z and low-z bins. More detailed modeling of the effect of merger rates on the mass function will be presented in a further paper (Bundy et al., in preparation).

Most difficult for the dry merger hypothesis as a key feature of galaxy formation is the very weak environmental dependence we observe in the downsizing signal. Given that a mechanism has to be found to preferentially bring quiescent sub-units together, one would expect a strong density dependence in the dry merger rate. By contrast, in our large sample it is clear that the majority of quiescent galaxies residing in environments whose density lie within $\sim 1\sigma$ of the median value were assembled in a manner that is not sensitive to environment.

Finally, our results show that downsizing is not only a feature of the star formation histories of massive quiescent galaxies (e.g., Treu et al. 2005a; van der Wel et al.

2005), but is also apparent in their stellar mass *assembly* histories. This observation is of particular interest for galaxy formation models based on the hierarchical ΛCDM framework. By incorporating AGN feedback effects into the semi-analytic models from the Munich group, De Lucia et al. (2005) predict star formation histories for massive ellipticals that follow the downsizing trend in which more massive galaxies host older stellar populations. However, interpretations of these models are difficult. For example, the distributions of assembly ages of ellipticals in Figure 5 from De Lucia et al. (2005) seem to predict a hierarchical, "bottom-up" mass assembly history for ellipticals while the observations presented here reveal the opposite picture. It should be noted that this comparison is problematic because De Lucia et al. (2005) define ellipticals by their morphology at $z = 0$ whereas observations trace the morphology of galaxies at a given redshift. Still, it should be emphasized that the results here suggest that in addition to forming stars earlier, massive early-type galaxies also assembled their stellar mass earlier than less massive systems.

4.6.2 The Origin of Downsizing

The results of this study reveal important clues as to the nature of downsizing and, via a clear measurement of the trends, will assist in constraining and ruling out several of the popular explanations. A detailed comparison with such models is beyond the scope of the current study, but we discuss some of the key issues here.

First we wish to dismiss a possible suggestion that our discovery of the quenching mass threshold is somehow an artifact of our selection process. For example, it might be argued that our result could arise from a uniform decrease in the incidence of star formation at all masses combined with a survey selection effect in which rare, massive objects are seen only at higher redshifts because of the larger volumes probed. Our results exclude this possibility. First, our sampled volumes are relatively similar (only a factor of $\sim$4 difference between low-z and high-z), and we demonstrate that the fraction of star-forming galaxies depends not only on redshift but mass as well. Figure 4.11 illustrates this point. Here we divide the sample into smaller

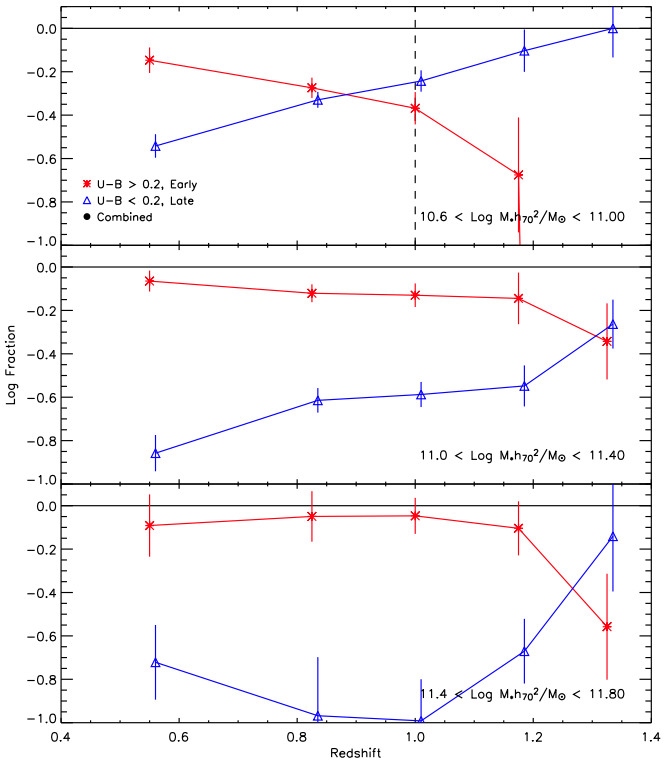

Figure 4.11 Fractional contribution in log units to the total mass function divided into stellar mass bins and plotted as a function of redshift. 4.9.

redshift intervals and follow the evolution of the red and blue populations in the three largest stellar mass bins, charting the fractional contribution of the two populations to the combined mass function. The highest mass bin contains the largest fraction of quiescent galaxies at almost every redshift, and the transformation of the active population into passively-evolving systems occurs first in the high mass bin and later at lower masses. The rate of chance in the incidence of star formation is clearly mass-dependent.

Turning now to physical explanations, we have shown in §4.5.3 that the quenching mass threshold, parametrized by M_Q, provides a very useful description of how the fraction of star-forming galaxies evolves. The question then is what mechanism is responsible for this quenching? Can it adequately reproduce the quantitative trends observed, for example the weak environmental dependence? Merging may provide a starting point for answering this question and explaining the transformation of

late-types into early-types. Merging between disk systems has long been thought to be an important mechanism by which ellipticals form (e.g., Toomre 1977; Barnes & Hernquist 1991; Springel et al. 2005b), and the similar behavior of the morphological and color-defined values of M_Q in Figure 4.8 suggests that the same process governing the growth of ellipticals may also broadly explain the rise of quiescent galaxies in general. However, as argued above, significant merging is likely to affect the *shape* of the total mass function, which does not appear to evolve strongly in our sample. Merging may be occurring at masses below our completeness limit, but the observed evolution in the relative mix of early- and late-type galaxies suggests a process that quenches star formation on timescales that are shorter than the merger timescale. This would lead to higher values for M_Q in the morphological samples, as observed.

Merger-triggered quenching has further difficulties. Fundamentally, the hierarchical merging of dark matter halos is expected to proceed from low mass to high mass, not the other way around. One solution to this difficulty would be to appeal to the fact that merging and assembly rates are accelerated in regions of high density (e.g., De Lucia et al. 2004), which also host the most massive systems. Over a range of environments, downsizing could arise naturally from the fact that massive galaxies live in these accelerated environments. However, we find no significant density dependence in the bulk of our sample (Figure 4.9) and only a weak dependence in the extremes of the density distribution. This suggests that density-dependent merger rates are not the answer and that an internal feedback process on galactic scales is largely responsible for driving the downsizing pattern.

Many groups have recently suggested that internal AGN feedback may be the missing ingredient. Triggered perhaps by merging, radio heating of the available gas effectively quenches further star formation, eventually transforming late-type galaxies into early-types (e.g., Silk & Rees 1998; Granato et al. 2004; Dekel & Birnboim 2004; Hopkins et al. 2005a; Croton et al. 2005; De Lucia et al. 2005; Scannapieco et al. 2005). The effectiveness of the AGN feedback is tied to the halo cooling time (e.g., Croton et al. 2005; De Lucia et al. 2005), resulting in greater suppression in lower mass halos as a function of time. This hypothesis produces older stellar populations in more

massive galaxies but, as it is currently implemented, does not reproduce observations of the decline in M_Q (Croton, priv. communication). Moreover, some environmental dependence is apparently expected as the triggering of AGN is accelerated in dense environs (De Lucia et al. 2005).

The model described in Scannapieco et al. (2005) presents a hybrid solution that combines internal AGN feedback with properties of the immediate environment. Here the AGN feedback efficiency also depends on the density of the local intergalactic medium (IGM). As the IGM density decreases with the expansion of the universe, smaller AGN in less massive halos become capable of quenching star formation, thereby producing a downsizing signal. With this cooling mechanism, Scannapieco et al. (2005) find a redshift dependence of $(1+z)^{3/4}$, significantly less than the observed dependence of $M_Q \propto (1+z)^{4.5}$. In addition to this problem, a key question is how the IGM density relates to the environmental density we use in this study. The answer is likely to be quite complicated, but if the two are proportional, then downsizing in this scenario would be slowed in overdense regions and accelerated in underdense regions. The predicted trend seems to work in the opposite sense to that observed (Figure 4.10).

Regardless of the physical explanation (and several may be necessary), it is clear that precise quantitative measures of the evolving mass distribution and its dependence on the basic parameters explored here will provide the ultimate test of these theories.

4.6.3 Reconciling Downsizing with the Hierarchical Structure Formation

Over the past decade there has been strong confirmation from many independent observations that the large-scale structure of the universe matches the basic predictions of the cold dark matter (CDM) model. In this model, dark matter dominates the mass density of the universe, and visible galaxies trace the distribution of dark matter "halos", dense aggregations of CDM formed by gravitational instability from

the small fluctuations present in the early universe. In the CDM model halos grow through constant, hierarchical merging with other halos. Both the masses of individual systems and the total amount of matter in halos over a given mass increase monotonically with time. At any epoch, halos are growing and merging most actively on the largest mass scales, and the most massive halos are also the most recently assembled ones. Thus, at first examination downsizing seems completely at variance with the CDM picture.

Several processes contribute to reversing the bottom-up trend in structure formation, producing what appears to be to a top-down pattern to galaxy formation. The first is simply the gradual effect of the dark energy, or cosmological constant, which causes halo growth rates to slow once the universe reaches a scale factor $(1+z)^{-1} > \Omega_m$. The second is the physics of gas cooling, which has been known since well before the CDM model was introduced to select out a characteristic mass scale for galaxy formation (Rees & Ostriker 1977; Silk 1977; White & Rees 1978). Gas cannot cool rapidly, and by implication stars cannot form efficiently, until structure formation produces virial temperatures in excess of 10^4 K within halos. This sets the epoch for the onset of galaxy formation at $z \sim 15$–20. Once gas temperatures reach 10^6–10^7 K, cooling again becomes inefficient, turning off star formation in the most massive halos. This then marks the end of the era of galaxy formation, as more and more mass builds up in group and cluster halos over this cooling limit.

More detailed numerical or semi-analytic models of galaxy formation show that the cooling delay alone is insufficient to reduce star formation to observed levels, particularly in massive halos, and that other forms of feedback are required, although the exact details remain controversial (e.g., Benson et al. 2003). Nonetheless, the net effect of this feedback is to place an upper limit on the range of halo mass over which active star formation can take place. This limit, taken together with the decline in the global structure formation rate at late times, can certainly explain why star formation in galaxies is rarer at the present-day than it was at $z \sim$1–2. As discussed in §4.6.2, it is less obvious how to explain the observed decline in the *mass scale* of star-forming objects.

To help gain insight into this question, we can attempt to relate various galaxies in our sample to dark matter halos. Models of halo occupation, or similar attempts to reconcile observed luminosity functions and correlation functions with theoretical halo mass functions, predict that galaxies with the range of stellar masses sampled here ($\log(M/M_{\odot}) \sim 10$–$12$, corresponding to $\log L_{b_J} \sim 10$–11.2) should reside in dark matter halos of mass 10^{12}–$10^{15} M_{\odot}$ (e.g., Yang et al. 2003; Cooray & Milosavljević 2005a) and furthermore that 75-80% of these galaxies will be "central," that is the dominant galaxies within their halo rather than satellites of a brighter galaxy (Cooray & Milosavljević 2005b). Thus, these models suggest that the objects in the three mass bins in Figure 4.11 correspond approximately to central galaxies in galaxy, group, and cluster halos.

In the top panel of Figure 4.12 we show the comoving number density of halos of mass $\log(M/M_{\odot}) = 12.5, 13.5$, and 14.5 as a function of redshift (three lines from top to bottom). The numbers are roughly consistent with the comoving number densities of galaxies in our three mass bins, although the most massive stellar objects are more abundant than $10^{14.5} M_{\odot}$ halos and may therefore reside in slightly less massive systems. The bottom panel shows the mean ages of halos in the three mass bins as a function of observed redshift. The mean age here is defined as the time elapsed since half of the halos in that mass range had first built up 90% or 50% of their current mass in a single progenitor (solid and dashed curves respectively), calculated using equation 2.26 from Lacey & Cole (1993).

Regardless of which criterion one uses for defining the formation epoch, the timescales for the low-mass halos are roughly twice those for the massive systems, and the change in age between $z = 1.4$ and $z = 0.4$ is roughly 2.5 times that between $z = 1.4$ and $z = 1.0$. Combining these results, we conclude that if the observed decline in star formation is related to or triggered by halo growth, then the timescale for this process is at least 5 times longer in the low-mass systems than it is in the high-mass systems. Since global dynamical timescales should be independent of halo mass at a given redshift, this suggests that the quenching mechanism is strongly mass-dependent with the potential for different physical processes acting in different

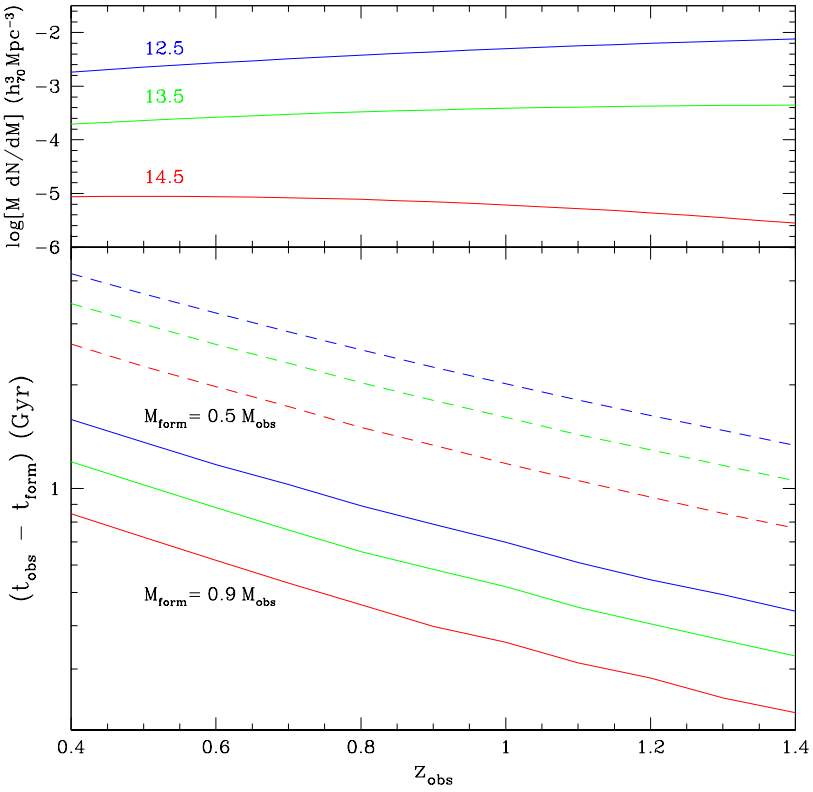

Figure 4.12 (Upper panel) The abundance of halos likely to host central galaxies in the three mass ranges plotted in Figure 4.11 versus redshift. The curves are labeled with $\log(M/M_{\odot})$. (Lower panel) Mean age of these systems as a function of their observed redshift. The mean age is defined as the time elapsed since half of the systems had built up a fraction f of the mass they have at z_{obs}. Solid curves show the age for $f = 0.9$ and dashed curves $f = 0.5$.

mass ranges. As discussed previously, we note that environment is normally the most obvious explanation for downsizing, with numerical simulations of structure formation indicating that dense environments evolve somewhat like high-density, high-σ_8 universes, producing older and more massive halos at any given epoch, while structure formation in voids is retarded (e.g., Gottlöber et al. 2001). The lack of a strong environmental dependence in our results, however, suggests that environment alone cannot be responsible for the observed trends in the quenching timescale with mass.

4.7 Conclusions

Using a large sample that combines spectroscopy from the DEEP2 Galaxy Redshift Survey with panoramic near-IR imaging from Palomar Observatory, we have investigated the mass-dependent evolution of field galaxies over $0.4 < z < 1.4$. We have constructed stellar mass functions for active and quiescent populations, defined in several ways, and divided into different samples according to accurate measures of the environmental density determined from the extensive spectroscopic data. We summarize our conclusions below:

- The mass functions of active and quiescent galaxies integrated over all environments conclusively demonstrate a downsizing signal. We quantify this by charting the evolution in a "quenching mass," M_Q, which describes the mass scale above which feedback processes suppress star formation in massive galaxies. We find that $M_Q \propto (1+z)^{4.5}$ with a factor of $\approx$5 decrease across the redshift range probed.

- The *assembly* of quiescent or "early-type" galaxies occurs first at the highest masses and then proceeds to lower mass systems. The relative abundance with $M_* \sim 10^{10}\mathrm{M}_\odot$ has increased by a factor of $\approx$6 from $z \sim 1.2$ to $z \sim 0.55$, whereas the total mass function exhibits little evolution (less than 0.1–0.2 dex). This implies that early-type systems result largely via the transformation of active star-forming galaxies, indicating that "dry mergers" are not a major feature of their assembly history.

- Alternative ways of dividing active and quiescent galaxies, including the use of [OII] line widths and HST-derived morphologies, show qualitatively similar mass-dependent evolution and quenching. Interestingly, we observe that morphological evolution appears to take place on longer timescales than changes in the apparent star formation rate which operate at lower mass scales at each redshift.

- For the majority of galaxies living in regions within $\sim 1\sigma$ of the median environmental density, downsizing shows little or no dependence on environment. An environmental signal is apparent when the ends of the density distribution are compared. In this case, downsizing in high-density regimes appears moderately accelerated compared to low-density ones, with values of M_{tr} lower by a factor of ~ 2.

- We discuss several possibilities for the origin of downsizing based on our results. We clearly rule out a scenario in which the incidence of star formation decreases uniformly for galaxies at all masses. The weak density dependence also argues against explanations that rely on the accelerated assembly of structure in dense environments, favoring internal mechanisms instead.

- Through comparisons to the expected behavior of dark matter halos, we argue that the dynamical timescale resulting from the growth of structure is at least 5 times longer in galaxies hosted by halos with $\log M/M_{\odot} \approx 12.5$ ($\log M_*/M_{\odot} \approx 10.8$) compared to $\log M/M_{\odot} = 14.5$ ($\log M_*/M_{\odot} \approx 11.6$). Because global dynamical scales are also independent of halo mass at a given redshift, it is suggested that the quenching mechanism is strongly mass-dependent with the potential for different physical processes acting in different mass ranges.

There are two obvious avenues for further studies of downsizing. In a forthcoming paper (Bundy et al., in preparation) we discuss the constraints on merging and the growth of galaxies determined by our observations of the total mass function. This will help dissect the role of merging in driving downsizing. In the near future it will also be possible to chart the incidence of AGN among the galaxy population and compare it to the incidence of star formation to probe the link between quenching and AGN. The significant Chandra follow up observations currently underway in the EGS will make that field particularly exciting for such work. Other efforts from the DEEP2 collaboration will focus on precise measures of the evolving star formation rate (Noeske et al., in preparation) and will detail the dependence of other galaxy properties on specific environments (Cooper et al., in preparation).

Acknowledgments

The Palomar Survey was supported by NSF grant AST-0307859 and NASA STScI grant HST- AR-09920.01-A. Support from National Science Foundation grants 00-71198 to UCSC and AST 00-71048 to UCB is also gratefully acknowledged. We wish to recognize and acknowledge the highly significant cultural role and reverence that the summit of Mauna Kea has always had within the indigenous Hawaiian community. It is a privilege to be given the opportunity to conduct observations from this mountain.

Chapter 5

The Merger History of Field Galaxies[1]

Using deep infrared observations conducted with the CISCO imager on the Subaru Telescope, we investigate the field-corrected pair fraction and the implied merger rate of galaxies in redshift survey fields with Hubble Space Telescope imaging. In the redshift interval, $0.5 < z < 1.5$, the fraction of infrared-selected pairs increases only modestly with redshift to $7\% \pm 6\%$ at $z \sim 1$. This is nearly a factor of three less than the fraction, $22\% \pm 8\%$, determined using the same technique on Hubble Space Telescope (HST) optical images and as measured in a previous similar study. Tests support the hypothesis that optical pair fractions at $z \sim 1$ are inflated by bright star-forming regions that are unlikely to be representative of the underlying mass distribution. By determining stellar masses for the companions, we estimate the mass accretion rate associated with merging galaxies. At $z \sim 1$ we estimate this to be $2 \times 10^{9\pm0.2}$ $M_\odot$ galaxy^{-1} Gyr^{-1}. Although uncertainties remain, our results suggest that the growth of galaxies via the accretion of pre-existing fragments remains as significant a phenomenon in the redshift range studied as that estimated from ongoing star formation in independent surveys.

[1]Much of this chapter has been previously published as Bundy et al. (2004)

5.1 Introduction

The hierarchical growth of dark matter halos is thought to govern the assembly history and morphological evolution of galaxies. Nearby examples of interacting and merging galaxies are well known, and many attempts to survey the merging and mass accretion rate at various redshifts have been made by several groups (Burkey et al. 1994; Carlberg et al. 1994; Yee & Ellingson 1995; Patton et al. 1997; Le Fèvre et al. 2000; Patton et al. 2000, 2002; Conselice et al. 2003). Strong evolution of the global merger rate was used to explain the observed faint galaxy excess (Broadhurst et al. 1992), the evolution of the luminosity function (Lilly et al. 1995a; Ellis et al. 1996), and that of galaxy morphologies (Giavalisco et al. 1996; Brinchmann et al. 1998). Evolution of the merger rate can also be used to place constraints on structure formation (Baugh et al. 1996; Kauffmann 1996).

Le Fèvre et al. (2000) used Hubble Space Telescope (*HST*) F814W images of redshift survey fields to measure the pair fraction to $z \sim 1$. They found an increase in the field-corrected pair fraction to 20% at $z \sim$ 0.75-1. However, as Le Fèvre et al. (2000) discuss, various biases affect this result. For example, in the restframe blue, bright star-forming regions, possibly triggered by interactions, might inflate the significance of pair statistics and give a false indication of the mass assembly rate.

Infrared observations are less biased by star formation and serve as a better tracer of the underlying stellar mass in galaxies (Broadhurst et al. 1992). Dickinson et al. (2003) employed this in their investigation of the global stellar mass density for $z < 3$. They find that 50 to 70% of the present-day stellar mass was in place by $z \sim 1$. A second line of evidence, the decline from $z \sim 1$ to 0 in the global star formation rate (e.g., Lilly et al. 1996), provides further support for the contention that galaxy growth was not yet complete at $z \sim 1$. Though a chronological picture of stellar mass assembly is emerging, the processes driving it are not understood. Are star-formation and stellar mass assembly induced mainly through the gradual accretion of gas converted quiescently into stars, or does assembly occur through merging, potentially accompanied by tidally-induced star formation? Characterizing the continued growth of galaxies,

and specifically the contribution from galaxy mergers since $z \sim 1$, is the major goal of this work.

5.2 Observations

In addition to high resolution infrared imaging, this study relies on optical HST data to facilitate the comparison between infrared and optical pair statistics and constrain stellar M/L_K ratios used to infer the stellar mass accretion rate. We therefore selected fields for our K_s-band imaging campaign that contain a combination of statistically-complete redshift surveys and archival *HST* F814W imaging. Target galaxies of known redshift were selected from the RA=10hr field of the CFRS (Lilly et al. 1995a), which spans the apparent magnitude range $17.5 < I_{AB} < 22.5$, and the Groth Strip area, surveyed by the Deep Extragalactic Evolutionary Probe (DEEP: Koo 1995) and selected according to $(R + I)/2 < 23$ (Koo 2000, private communication).

Archival *HST* images of the Groth Strip, retrieved from two programs (GTO 5090, PI: Groth; GTO 5109, PI: Westphal), reach $I \approx 24$ (Groth et al. 1994), a depth sufficient for our study. The deeper *HST* images of the CFRS fields ($I < 24.5$) are described by Brinchmann et al. (1998).

K_s-band observations were performed using the CISCO imager (Motohara et al. 2002) on the Subaru telescope during two campaigns in 2002 April and 2003 April. The camera has a field of 108 arcsec on a side with a pixel size of 0.11 arcsec and is thus fairly well-matched to that of WFPC2. Field centers were chosen to maximize the number of galaxies of known redshift falling within the CISCO field of view. Given that we are concerned with counting satellites around individual hosts, our primary results will not be biased by this maximization.

In total, six Groth Strip and four CFRS fields were imaged to a depth ($\sim$2.6 ks) deemed adequate for locating galaxies at least 2 magnitudes fainter than most of the hosts (see below). In total, 190 redshift survey galaxies were sampled in the K_s-band (151 fully overlap with HST images and are bright enough for the comparison to the optical pair fraction). The infrared data were reduced using the AUTOMKIM

pipeline developed at the Subaru facility by the CISCO group.

The limiting depth for locating faint satellites was estimated by performing photometry on artificial stars inserted into each image and by comparing the observed galaxy number counts to those published by Djorgovski et al. (1995). Both techniques agree, demonstrating that the CISCO data are complete at the 90% level at $K = 22.5$. Object detection and photometry in both the optical and infrared were carried out using the SExtractor package (Bertin & Arnouts 1996).

5.3 Optical versus Infrared-Selected Pair Fractions

First, we compare the optical and infrared pair fractions, closely following the precepts of Le Fèvre et al. (2000), though we adopt the cosmology—$\Omega_M = 0.3, \Lambda = 0.7$, and $h = 0.7$—instead of $q_0 = 0.5$ and $h = 0.5$ as used by Le Fèvre et al. (2000). Pairs are identified as companions to a limit no more than 1.5 magnitudes (independently in both optical and K_s-band) fainter than their host galaxy within a separation radius of $r_p = 20$ kpc. Satellites within this radius are expected to strongly interact with the halo of the host and merge in less than $\sim$1 Gyr due to dynamical friction (Patton et al. 1997). Multiple satellites around the same host are counted as separate pairs, and a field correction is applied to the pair counts based on the observed number density. Throughout, we assume that the pair fraction is independent of the intrinsic properties of the host galaxies and the way they were selected.

The field-corrected optical and infrared pair fractions for a sample of 151 host galaxies of known redshift with $K < 21$ and $I < 23$ are presented in Figure 1 and Table 1 and contrasted with the results using the same optical procedure as derived from Table 3 of Le Fèvre et al. (2000). Our first redshift bin ($0.2 < z < 0.5$) contains too few hosts for useful comparisons, but in the two higher redshift bins ($0.5 < z < 0.75$ and $0.75 < z < 1.5$), the statistical significance is adequate. There, although we find optical results comparable to Le Fèvre et al. (2000), the infrared pair fraction is a factor of 2-3 less. See Figure 2 for some examples.

To examine the possibility that our comparison with an equivalent *HST* analysis

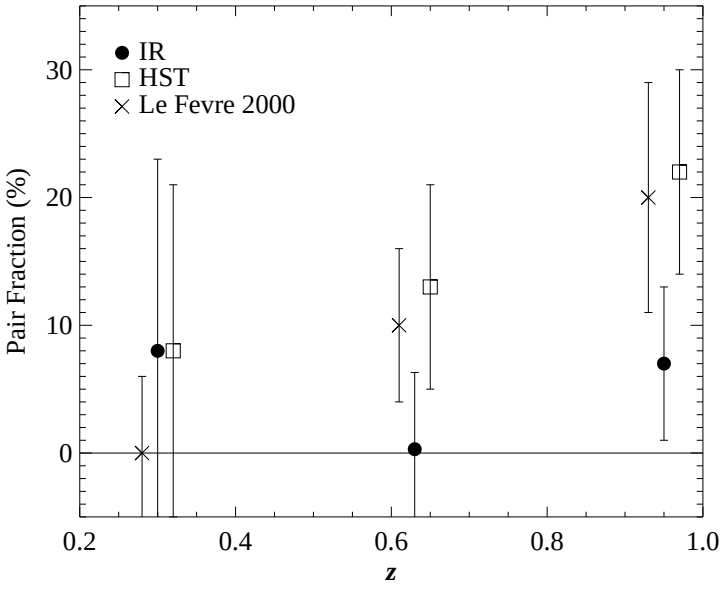

Figure 5.1 The field-subtracted pair fraction as measured in the infrared and optical. K_s-band measurements appear as filled circles and *HST* F814W measures as squares. The new results are compared with those of Le Fèvre et al. (2000).

may be biased by resolution effects, we convolve each 0.″1 *HST* image to the corresponding CISCO resolution, which varies from 0.″35 to 0.″5. We then repeat the detection and analysis, including the background number counts. The *HST* pair fraction decreases by only ∼30%, remaining a factor of two above the infrared pair fractions in the two highest redshift bins. We also investigate the separation distribution between each optical companion and its host. The smallest separation is just above 0.″5, implying that the majority of optically-identified pairs would be readily resolved in the CISCO images but were simply too faint in the infrared to be counted. Both results suggest that resolution is not the primary difference between the two samples; rather it is the bluer colors of the satellite galaxies. In general, observed satellite galaxies tend to be bluer in $(V - K)$ than hosts, though the detection in IR favors redder companions.

Table 5.1. Pair Fraction

Sample	z	N_{gal}	N_{maj}	N_{proj}	Pair Fraction (%)	Merger Fraction (%)
CISCO	0.2–0.5	22	6 (0.27)	4.4 (0.20)	8 ± 14	4 ± 10
CISCO	0.5–0.75	47	4 (0.09)	3.8 (0.08)	0.3 ± 6	0.2 ± 5
CISCO	0.75–1.5	74	11 (0.15)	5.8 (0.08)	7 ± 6	7 ± 6
HST F814W	0.2–0.5	22	5 (0.23)	3.3 (0.15)	8 ± 13	5 ± 8
HST F814W	0.5–0.75	47	10 (0.21)	4.0 (0.09)	13 ± 8	11 ± 7
HST F814W	0.75–1.5	74	25 (0.34)	8.5 (0.11)	22 ± 8	21 ± 8
Le Fèvre	0.2–0.5	98	11 (0.11)	19 (0.19)	0	0
Le Fèvre	0.5–0.75	89	21 (0.24)	12.2 (0.14)	9.9 ± 6	8 ± 5
Le Fèvre	0.75–1.3	62	21 (0.34)	8.4 (0.14)	20.3 ± 9	19.4 ± 9

Note. — N_{gal} is the total number of galaxies drawn from the redshift sample. N_{maj} is the number of companions fitting the pair criteria described in the text. N_{proj} is the expected number of contaminating field galaxies. The pair fraction is defined as $(N_{maj} - N_{proj})/N_{gal}$, and the merger fraction is the pair fraction corrected by a factor of $0.5(1 + z)$, where $(1 + z)$ corresponds to the mean redshift of the bin. Numbers appearing in parentheses are the averages per host galaxy, printed for comparison to N_c^D and N_c^R in Table 5.2. Results from "All CFRS+LDSS" in Table 3 of Le Fèvre et al. (2000) are also reproduced. Errors are calculated using counting statistics.

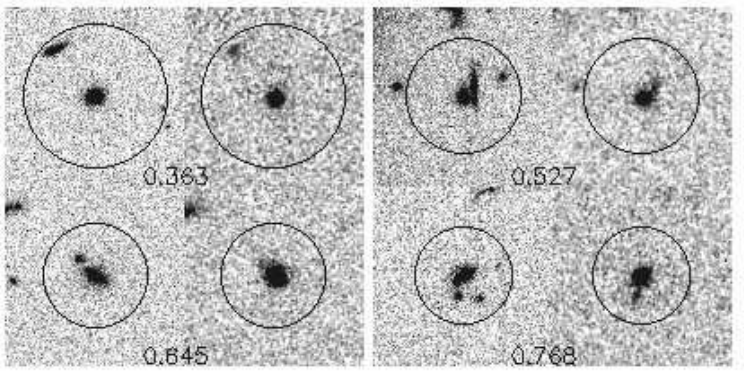

Figure 5.2 Examples of pairs identified in the optical but not in the infrared. In each set the left postage stamp is from *HST* I_{814}, and the right is from CISCO K_s-band images. The 20 kpc radius and redshifts are indicated.

5.4 Weighted Infrared Pair Statistics

We now explore a more detailed formalism for investigating the merger history as laid out by Patton et al. (2000). Rather than applying a differential magnitude cut linked to the host galaxy, we select companions in a fixed absolute magnitude range, $-24 \leq M_{K'} \leq -19$, regardless of the host. This will increase the number of observed pairs since we include fainter companion galaxies. Our sample for this analysis also grows to 190 hosts because host galaxies with $21.0 < K' < 22.5$ are now included.

As in §3, the companion search radius is set to $r_p = 20$ kpc and field subtraction implemented as before. Absolute magnitudes are calculated using k-corrections for the K'-band tabulated by Poggianti (1997) (using the Sa model), assuming that each companion galaxy is at the same redshift as its host.

A volume-limited estimate of the pair fraction as a function of redshift can be achieved by applying weights to both companions and hosts. As it is easier to detect intrinsically fainter galaxies nearby, higher redshift companions must be given more weight. The opposite is true for host galaxies because the observed number of pairs per host is less certain at higher redshift. Following Patton et al. (2000), these weights are based on the comoving density of companions observed in a hypothetical volume-limited survey compared to that in a flux-limited survey. We calculate these weights by integrating K' (or K_s) band luminosity functions from Cole et al. (2001) for $z < 0.6$

Table 5.2. Weighted Pair Statistics

z	N_{gal}	N_c^D	N_c^R	N_c	Average M_K	Merger Fraction
0.2–0.5	30	0.18	0.04	0.14 ± 0.07	-17.9	12 ± 5
0.5–0.75	57	0.11	0.04	0.08 ± 0.06	-18.3	8 ± 5
0.75–1.5	93	0.29	0.03	0.26 ± 0.10	-20.5	24 ± 10

Note. — N_{gal} is the total number of galaxies drawn from the redshift sample. N_c^D is the raw, weighted number of companions per host, while N_c^R is the projected fraction from the field. The corrected average is N_c. The average M_K is the associated K_s-band luminosity in companions averaged over every host in the sample. The merger fraction is calculated as before. Errors are determined using weighted counting statistics.

and Kashikawa et al. (2003) for $0.6 < z < 1.5$.

The results are given in Table 5.2. At $z \sim 1$, the merger fraction of $24\% \pm 10\%$ is expectedly higher because of the inclusion of fainter galaxies. The errors are derived from counting statistics, and as in §3, we expect the true pair fraction to be slightly higher (about 1%) than observed because some faint companions may be obscured by large hosts. The implied merger rate suggests that 35% of typical L^* galaxies have undergone a merger with a companion in this luminosity range since $z \sim 1$.

5.5 Mass Assembly Rates

We have applied two pair counting methods and found that the Patton et al. (2000) method delivers a pair fraction higher than the technique of Le Fèvre et al. (2000) because the former includes fainter companions. To reconcile these two different results with a single mass assembly history, we estimate the stellar mass accretion rate associated with merging galaxies. Because it is not known which companions are physically associated with their host, the stellar mass of companions can only be determined in a statistical sense. We first fit our *VIK′* photometry of host galaxies

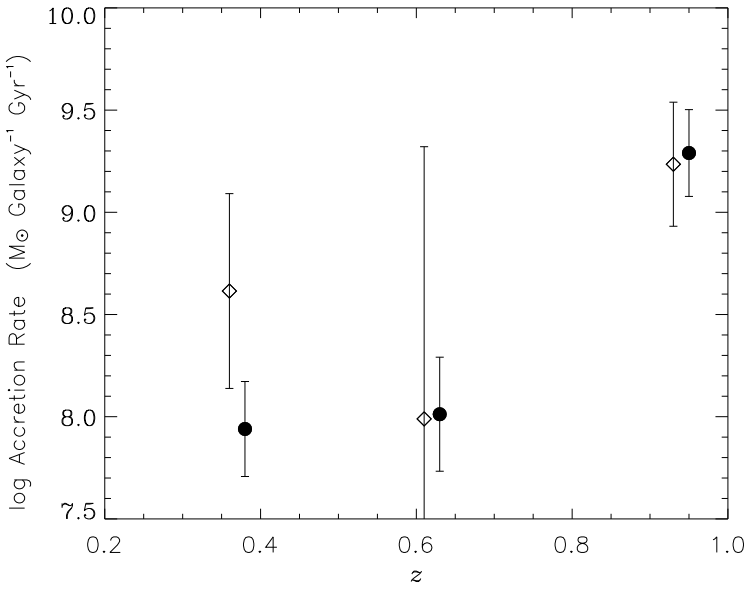

Figure 5.3 Stellar mass accretion rate per galaxy in three redshift bins. Filled symbols are the results from the Patton et al. weighted analysis. Open symbols are the results of the Le Fèvre et al. (2000) technique. The first redshift bin is again the least significant since it contains the fewest host galaxies.

(with redshifts) to template SEDs spanning a range of ages, star formation histories and metallicities, assuming a Salpeter IMF (with the range $0.1 - 100 M_{\odot}$, Bruzual & Charlot 2000, private communication). We then scale to the K_s-band luminosity to estimate the stellar mass (see Brinchmann et al. 2000). We assume the companions follow the same distribution of $M_*/L_{K'}$ vs. $L_{K'}$ as the hosts and use this distribution to estimate the stellar mass of companion galaxies. Finally, though the merging timescale depends on the details of the interaction, we follow previous studies (e.g., Patton et al. 2000) and assume an average value of 0.5 Gyr for galaxies separated by $r_p < 20$ kpc.

With these assumptions, we demonstrate that the two very different pair statistics are consistent with a similar merger history in terms of the accreted stellar mass. In Figure 5.3, open symbols are the mass accretion rate from the Le Fèvre et al. (2000) method, and solid symbols are that from the Patton et al. method. The large error bars include both statistics and 50% uncertainties in $M_*/L_{K'}$. Both methods illustrate

a rise in the stellar mass accretion rate at the highest redshifts, with the Patton et al. method giving a value of $2 \times 10^{9\pm0.2}$ $M_\odot$ galaxy^{-1} Gyr^{-1} at $z \sim 1$. This mass corresponds to ≈4% of the average stellar mass of host galaxies at these redshifts. The result may be compared with an estimate made by Conselice et al. (2003) of $6.4 \times 10^{8\pm0.1}$ $M_\odot$ galaxy^{-1} Gyr^{-1} at $0.8 < z < 1.4$ using morphological indicators to distinguish merger remnants.

We contrast our assembly rate from pre-existing stellar systems with the *integrated* stellar mass density (Dickinson et al. 2003), which reflects the growth of galaxies from newly-formed stars. While not necessarily completely independent (for example if merging triggers new star formation), the relative magnitudes of the two phenomena are interesting to consider. Using the luminosity functions of Kashikawa et al (2003) to determine the comoving number density of host galaxies, we integrate the mass accretion rate to estimate the stellar mass assimilated by galaxies in the host K-band luminosity range, finding $\Delta\rho_*^m \approx 3 \times 10^{8\pm0.2}$ $M_\odot$ Mpc^{-3}. For a Salpeter IMF, we deduce that 30% of the local stellar mass in luminous galaxies was assimilated via merging of pre-existing stars since $z \sim 1$, comparable to the build-up deduced by Dickinson et al. (2003) from ongoing star formation.

Acknowledgments

We thank Dr. Chris Simpson and Dr. Kentaro Aoki for their help during our observations at the Subaru Telescope. RSE and MF acknowledge the generosity of the Japanese Society for the Promotion of Science.

Chapter 6

The Relationship Between the Stellar and Total Masses of Disk Galaxies[1]

Using a combination of Keck spectroscopy and near-infrared imaging, we investigate the K-band and stellar mass Tully-Fisher relation for 101 disk galaxies at $0.2 < z < 1.2$, with the goal of placing the first observational constraints on the assembly history of halo and stellar mass. Our main result is a lack of evolution in either the K-band or stellar mass Tully-Fisher relation from $z = 0 - 1.2$. Furthermore, although our sample is not statistically complete, we consider it suitable for an initial investigation of how the fraction of total mass that has condensed into stars is distributed with both redshift and total halo mass. We calculate stellar masses from optical and near-infrared photometry and total masses from maximum rotational velocities and disk scale lengths, utilizing a range of model relationships derived analytically and from simulations. We find that the stellar/total mass distribution and stellar-mass Tully-Fisher relation for $z > 0.7$ disks is similar to that at lower redshift, suggesting that baryonic mass is accreted by disks along with dark matter at $z < 1$ and that disk galaxy formation at $z < 1$ is hierarchical in nature. We briefly discuss the evolutionary trends expected in conventional structure formation models and the implications of extending such a study to much larger samples.

[1]Much of this chapter has been previously published as Conselice et al. (2005)

6.1 Introduction

In the currently popular hierarchical picture of structure formation, galaxies are thought to be embedded in massive dark halos. These halos grow from density fluctuations in the early universe and initially contain baryons in a hot gaseous phase. This gas subsequently cools, and some fraction eventually condenses into stars. Much progress has been made in observationally delineating the global star formation history and the resulting build-up of stellar mass (e.g., Madau et al. 1998; Brinchmann & Ellis 2000; Dickinson et al. 2003; Bundy et al. 2005a). However, many of the physical details, particularly the roles played by feedback and cooling essential for a full understanding of how galaxies form, remain uncertain. Models (e.g., van den Bosch 2002; Abadi et al. 2003) have great predictive power in this area but only by assuming presently untested prescriptions for these effects. Obtaining further insight into how such processes operate is thus an important next step not only in understanding galaxy evolution, but also in verifying the utility of popular models as well as the hierarchical concept itself. One approach towards understanding this issue is to trace how the stellar mass in galaxies forms in tandem, or otherwise, with its dark mass.

The first step in this direction began with studies of scaling relations between the measurable properties of disk galaxies, specifically the relation between luminosity and maximum rotational velocity (Tully & Fisher 1977). Studies utilizing roughly a thousand spiral galaxies have revealed a tight correlation between absolute magnitude and the maximum rotational velocity for nearby galaxies (Haynes et al. 1999). The limited data at high redshift suggests the TF relation evolves only modestly, equivalent to at most 0.4 - 1 magnitudes of luminosity evolution to $z \sim 1$ (Vogt et al. 1997; Ziegler et al. 2002; Böhm et al. 2004). How the Tully-Fisher relation evolves with redshift is still controversial, although it appears that fainter disks evolve the most (Böhm et al. 2004) and that selection effects are likely dominating the differences found between various studies. Furthermore, it has been difficult for modelers to reproduce the Tully-Fisher relation to within 30% (e.g., Cole et al. 2000), making it an important constraint on our understanding of the physics behind galaxy formation.

Unfortunately, any interpretation of the TF relation is complicated by the fact that both luminosity and virial mass might be evolving together. A more physically motivated comparison would be between stellar and virial mass. Not only does this relation break potential degeneracies in the TF technique, but it also samples more fundamental quantities. In this study we begin this task by investigating the evolution in the fraction of the total mass in stars. This can be accomplished with some uncertainty by contrasting the *stellar mass* of a galaxy with its *halo mass*. We selected disk galaxies for this effort since these two quantities can be effectively probed observationally for such galaxies with various assumptions (e.g., van den Bosch 2002; Baugh et al. 2005).

This study presents the first investigation of the near-IR TF relation, as well as a comparison between stellar and halo masses, for 101 disk galaxies within the redshift range $0.2 < z < 1.2$ drawn mostly from the DEEP1 redshift survey (Vogt et al. 2005). Our goal is to address several questions relating to the mass assembly history of disks. As our sample is not formally complete in any sense, we cannot derive general conclusions concerning the history of *all* present-day disks. However, we can determine whether the disks selected from the DEEP1 survey in the sampled redshift range are still accreting matter and converting baryons into stellar disks at a significant rate. We construct the stellar mass Tully-Fisher and stellar mass/halo mass relation for our sample and find that there is little evolution in either from $z \sim 0 - 1.2$. This suggests that the dark and stellar components of disk galaxies grow together during this time.

This chapter is organized as follows: §6.2 contains a description of the sample including the fields used, the different data products, and a discussion of uncertainties. §6.3 describes how various quantities such as the halo and stellar masses are derived from the data. §6.4 presents our results and §6.5 presents our conclusions. We assume the following cosmology throughout this work: $H_0 = 70$ km s^{-1} Mpc^{-1}, $\Omega_\Lambda = 0.7$, and $\Omega_m = 0.3$.

6.2 Data

6.2.1 The DEEP1 Extended Sample

Our sample consists of 101 galaxies, 93 of which are drawn from the DEEP1 survey (see Vogt et al. 2005; Simard et al. 2002; Weiner et al. 2005), and 8 of which were obtained independently. Each of these systems, with redshifts between $z \sim 0.2$ and $z \sim 1.2$, has a resolved rotation curve which was obtained at Keck Observatory using LRIS (Oke et al. 1995). The additional data presented in this work, which enables stellar masses to be compared with virial masses, consists of near-infrared imaging and is described in §6.2.2.

Full details of the sample selection are discussed in DEEP1 papers (Vogt et al. 1996, 1997, 2005), to which the interested reader is referred. Moreover, the necessary assumptions implicit in the derivation of rotation curves are also detailed in those papers. Briefly, galaxies were selected morphologically as elongated disks in Hubble Space Telescope (HST) F814W (I_{814}) images with $I_{814} < 23$. The inferred inclination was chosen to be greater than 30deg to facilitate a measurement of the rotational velocity. The optical images used for both photometric and morphological analyses come from HST Wide Field Planetary Camera-2 (WFPC2) observations of the Groth Strip (Groth et al. 1994; Vogt et al. 2005), the Hubble Deep Field (Williams et al. 1996), and CFRS fields (Brinchmann et al. 1998). Using I_{814} images, structural parameters were determined for each galaxy using the GIM2D and GALFIT packages (Simard et al. 2002; Peng et al. 2002). We fit a two-component model to the surface brightness distribution, assuming a de Vaucouleurs law for the bulge and an exponential for the disk component. Based on these fits, the disk scale length, R_d, and bulge-to-disk ratio (B/D) were determined. The uncertainties in the R_d values determined through this method are possibly underestimated, as has been explored through careful 2-D fitting (e.g., de Jong 1996). To be inclusive of possible effects, we will incorporate an additional 30% uncertainty for our overall error on the measured values of R_d.

Details of the observations, reductions, and extraction of maximal rotational ve-

locities $V_{\rm max}$ from the LRIS spectroscopy are presented in Vogt et al. (1996, 1997, 2005). Briefly, each disk galaxy was observed along its major axis, as determined from the HST images (Simard et al. 2002). The maximum velocity, $V_{\rm max}$, is determined by fitting a fixed form for the rotation curve scaled according to the I_{814} disk scale length, $R_{\rm d}$. The assumed rotation curve has a linear form which rises to a maximum at 1.5× $R_{\rm d}$ and remains flat at larger radii. Our assumption that 1.5× $R_{\rm d}$ is the radius where the rotation curves for disks reach their maximum is reasonable based on a similar behavior for local disk systems of similar luminosity (Persic & Salucci 1991; Sofue & Rubin 2001). Our rotation curves are also visible out to several scale lengths, or roughly 2-5″ (e.g., Vogt et al. 1997), adequate for measuring $V_{\rm max}$. This model form is then convolved with a seeing profile that simulates the conditions under which the observations were taken, and $V_{\rm max}$ is determined by iterative fitting. Effects from the width of the slit, slit misalignment with the galaxy's major axis, and uncertainties in the inclination angle were taken into account when performing these fits and estimating the resulting errors. Typically, $V_{\rm max}$ is determined to a precision of 10-20% (e.g., Vogt et al. 1997).

6.2.2 Near-Infrared Imaging

The new data we present in this work consist of deep near-infrared observations of the DEEP1 extended sample. Precision near-infrared photometry is the critical ingredient for determining stellar masses for our sample (Brinchmann & Ellis 2000). Photometry was acquired in the K_s filter with three different instruments: the Keck Near Infrared Camera (NIRC, Matthews & Soifer 1994), the UKIRT Fast-Track Imager (UFTI, Roche et al. 2003), and the Cooled Infrared Spectrograph and Camera for OHS (CISCO, Motohara et al. 2002) on the Subaru 8.4 meter telescope (see Bundy et al. 2004). NIRC has a field of view of 38″ and a pixel scale of 0.15″ pixel^{-1}. The equivalent numbers for UFTI are: 96″ field of view with a pixel scale of 0.091 ″pixel^{-1}. The CISCO camera has a field of view of 108″ with a pixel scale of 0.105″ pixel^{-1}. The typical depths for these images is K_s = 20.5-21 (Vega) with a typical seeing of

$\sim 0.8''$.

In each case, the infrared data were taken with a dither pattern whose step size exceeded the typical size of the galaxies of interest. The data were reduced by creating sky and flat-field images from sets of deregistered neighboring science frames. Standard stars were observed for calibration purposes during the observations. Some images taken in good seeing but through thin cloud were subsequently calibrated in photometric conditions via shallower exposures taken with the Wide Field Infrared Camera (WIRC, Wilson et al. 2003) on the Hale 5 meter telescope.

6.2.3 Restframe Quantities

We measure our photometry in the K_s-band and HST I_{814} and V_{606} bands within a scale-length factor, either $1.5R_d$ or $3R_d$, both of which are generally large enough to avoid seeing effects from the K_s imaging. We then extrapolate the total magnitudes within each band out to infinite radius by using the fitted parameters for an exponential disk derived in the HST I_{814} band. To compare observables over a range in redshift, it is necessary to reduce all measures to a standard restframe. Galactic extinction corrections were applied using the formalism of Schlegel et al. (1998), and internal extinction was accounted for according to measured inclinations and luminosities using the precepts of Tully et al. (1998). It is debatable whether internal extinction corrections derived for nearby spirals are applicable to higher redshift disks. Our sample is mostly composed of systems with $M_B > -22$, where extinction could be a cause for concern. However, direct extinction measurements in moderate redshift disks, determined through overlapping pairs, find a modest overall extinction (White et al. 2000).

To derive absolute magnitudes and restframe colors, we estimated non-evolutionary k-corrections. The K-band k-corrections were computed from spectral energy distributions determined alongside the stellar mass fits. We experimented with both the original algorithm developed by Brinchmann & Ellis (2000) and also an independent one developed by Bundy et al. (2005a). Both methods agree very well. The ap-

proach is similar to that used by Vogt et al. (1996, 1997), where k-corrections were calculated from model SEDs from Gronwall & Koo (1995) based on various star formation histories. We also note that our derived k-correction values are very similar to non-evolutionary k-corrections derived by Poggianti (1997) using SEDs from.

6.3 Mass Estimators

6.3.1 Virial and Halo Masses

The virial mass of a galaxy - that is, the combination of the dark, stellar, and gaseous components - is perhaps its most fundamental property. However, obtaining an accurate estimate from observed quantities is difficult because there is no *a priori* agreed model for the relative distributions of the various components. Our approach to this challenge will be to use both analytical techniques and semi-analytical simulations to investigate the relationship between the total halo mass and our dynamical and structural observables. Although necessarily approximate and debatable in terms of the assumptions made, we will attempt, where possible, to investigate the uncertainties involved by contrasting the two approaches in the context of our data.

For a simple virialized system such as a circularly rotating disk, we can place constraints on the total mass within a given radius R independent of model assumptions. If $R > 1.5 \times \mathrm{R_d}$, where we estimate the maximum rotational velocity $\mathrm{V_{max}}$ is reached, the mass within R is given by

$$\mathrm{M_{vir}}(< \mathrm{R}) = \mathrm{V_{max}^2} R/\mathrm{G}, \tag{6.1}$$

where $R > 1.5 \times \mathrm{R_d}$. This assumes that the rotation curve reaches the maximum velocity by $1.5 \times \mathrm{R_d}$ (Persic & Salucci 1991); otherwise $\mathrm{V_{max}}$ should be replaced by $\mathrm{V}(R)$.

There are a few possible approaches for determining total halo masses, some of which require the use of simulations to convert observed dynamical qualities, usually $\mathrm{V_{max}}$, into halo masses. We take a basic approach using eq. [6.1] to obtain the total

mass with a given radius and take a suitably large total radius of 100 kpc to measure the total halo mass. This is often the extent of disk HI rotation curves and similar to the sizes of dark matter halos (e.g., Sofue & Rubin 2001). Another approach now being used (e.g., Bohm et al. 2004) has been proposed by van den Bosch (2002). In this case, it is argued from analytic simulations of disk galaxy formation that the quantity $M_{\rm vdB} = 10.9 \times {\rm M_{vir}(R_d)}$ gives, on average, the best empirical representation of the virial mass for simulated disks. The zero-point of the relationship between $\rm R_d V^2_{max}/G$ and virial mass is claimed to be independent of feedback and independent of the mass of the halo (van den Bosch 2002).

Semi-analytic models based on ΛCDM (Cole et al. 2000; Benson et al. 2002; Baugh et al. 2005) suggest, however, that the ratio between $\rm V^2_{max} R_d/G$ and halo mass is not as simple as the above formalism implies. The latest *Galform* models from Baugh et al. (2005) and Lacey (priv. communication) show that equation [6.1] and van den Bosch (2002) underpredict the dark halo mass. These models show that the relationship between the virial mass at $\rm R_d$ and the total halo mass changes as a function of mass in the sense that the ratio is higher for lower mass halos. Physically this can be understood if high mass halos have a larger fraction of their baryonic mass in a hot gaseous phase that is not traced by the formed stellar mass. Using the *Galform* models to convert our observables into a total halo mass is potentially inaccurate, as these models cannot reproduce the Tully-Fisher relation to better than 30%. However, there are reasons to believe that the semi-analytic models put the correct amount of halo mass into their modeled galaxies (e.g., Benson et al. 2002). This, however, does not necessarily imply that the $\rm V_{max}$ values in these models are able to accurately match the halo masses. Independent determinations of total halo masses are necessary to perform this test. We note that the masses from this approach match within 0.5 dex the masses derived from using eq. [6.1] with a suitably large total radius.

With these caveats in mind, we have used the *Galform* model results to fit the relationship between the virial mass at $\rm R_d$ (eq. 6.1) and the total mass of the halo ($\rm M_{halo}$), a ratio which we call $\Re = {\rm M_{vir}(R_d)/M_{halo}}$. We fit $\Re$ as a linear function of

$M_{vir}(R_d)$, such that $\Re = \alpha \times \log(M_{vir}(R_d)) + \beta$. Using the *Galform* results we fit α and β at redshifts $z = 0, 0.4, 0.8, 1.2$. We find that the functional form of $\Re$ does not change significantly with redshift, with typical values $\alpha = -0.1$ and $\beta = 1.3$. The value of the halo mass M_{halo} is then given by

$$M_{halo} = M_{vir}(R_d)/\Re. \tag{6.2}$$

Observational and model uncertainties contribute to errors on these virial and halo mass estimates in two ways. Measured scale lengths given by the GIM2D and GALFIT fitting procedure (§6.2.1) give an average error of 0.12 kpc, although we add an extra error to this to account for systematics seen when performing fits of single-component models to disks/bulge systems (de Jong 1996). At the same time, systematic difficulties in the rotation curve analysis (§6.2.1) can arise. Vogt et al. (2005) discuss these issues in some detail and conclude that the average error is $\sim$27 km s^{-1} (typically $\simeq$10-20%). Following the discussion of rotation curve fitting in §6.2.1, it is possible thatwe do not measure the true V_{max} required for insertion in equations (6.1 & 6.2). Even a modest underestimate of V_{max} would lead to a significant error in M_{vir}. In combination, these measurement uncertainties imply virial and halo masses precise to no better than 30%. The semi-analytic method for computing total halo masses is likely limited, and thus we also investigate the total halo masses found through the van den Bosch (2002) formalism and through the use of equation [6.1] out to 100 kpc. We find that the total halo mass through eq. [6.1], eq. [6.2], and van den Bosch (2002) are all fairly similar. We account for these differences in our use of total halo masses in §6.4.3.

6.3.2 Stellar Masses

Our procedure for deriving stellar masses follows the multi-color method introduced by Brinchmann & Ellis (2000) and described in §2.4, but also includes some differences we discuss below. Combining HST V_{606}, I_{814}, and near-infrared K_s photometry for a galaxy of known redshift, we fit a range of template SEDs synthesized using software

by Bruzual & Charlot (2003). Our photometry is done in a matched aperture large enough to avoid seeing problems associated with the K_s-band. These fitted SEDs constrain the K_s-band mass/light ratio. Our code for computing stellar masses only uses models with ages less than the age of the universe at the redshift observed. A χ^2 analysis normalized by the near infrared K_s-band luminosity yields the stellar mass. The template SEDs were constructed sampling a range of exponentially-declining star formation rates, metallicities, and ages with a Salpeter IMF. Using other forms of the IMF such as Chabrier, Kennicutt or Kroupa would result in computed stellar masses that are smaller by < 0.3 dex. We further assumed a simple exponentially declining star formation history with τ values ranging from 0.001 - 15.0 Gyr and metallicities from Z=0.005-5 in solar units. Typical uncertainties in this method are a factor of three (Brinchmann & Ellis 2000; Papovich et al. 2001; Drory et al. 2004a; Bundy et al. 2005a).

The SED is constrained by the observed colors as measured in an aperture of radius $1.5 \times R_d$ in each band, which is optimal in terms of signal-to-noise (S/N). We assume that there are no color gradients and use the colors measured within this aperture as the global color. The total K_s-band light is measured by extrapolating the $1.5 \times R_d$ flux to infinity, assuming the same exponential fit as measured in the HST I_{814} image.

Errors on the stellar masses arising from photometric uncertainties can be determined in a Monte Carlo fashion. Simulated exponential disks of a known magnitude were inserted into the reduced HST and ground based images and photometrically recovered using the tools that were applied to the sample. The simulated disks were arranged to randomly sample the selected ranges of disk scale-length R_d and inclination. The derived photometric errors were then input into the stellar mass calculations from which a 1σ range was calculated. The average error in M_* is 0.47 dex.

The calculation of stellar masses through this technique is limited to a degree by systematics which are difficult to constrain with the current data set. The K_s-band photometry errors are only a small source of this uncertainty. The models of the spectral evolution of galaxies depend both on the observed stellar libraries

and underlying theory, and some fundamental uncertainties remain (c.f. Bruzual & Charlot 2003). We expect uncertainties of about 5-10% given the range of possible models (Charlot et al. 1996). This is not important for the conclusions in this study but might be an issue with larger and more accurate data sets in the future.

We also cannot constrain the amount of recent star formation produced in bursts (e.g., Kauffmann et al. 2003a; Bell & de Jong 2001), resulting in a slight systematic overestimate of the stellar mass. The latter effect only becomes important at large burst fractions and should be $< 10\%$ for our big spirals (c.f. Drory et al. 2004a). The final systematic uncertainty is the dust correction adopted. We use the Calzetti (1997) extinction law in our stellar mass calculations, although other extinction laws produce very small differences (at most 10-20%) in the resulting stellar mass (Papovich et al. 2001). Taken together we are likely to have systematic uncertainties in our stellar mass estimates amounting to ~ 0.15 dex, which is lower than our random uncertainty; thus they will not influence our results.

6.4 Results

6.4.1 K-band Tully-Fisher Relation

The Tully-Fisher (TF) relation has been the traditional method for investigating how dark halos and the stellar components of disk galaxies relate. The optical relation has been studied in disks galaxies out to redshifts $z \sim 1$ by Vogt et al. (1996, 1997, 2005); Ziegler et al. (2002); Böhm et al. (2004). These investigations have found between 0.4 and ~ 1 magnitudes of restframe B-band luminosity evolution in disks between $z \sim 0$ and $z > 0.5$. This luminosity evolution is derived by assuming that the slope of the TF relation at high redshift is the same as it is at $z \sim 0$. The question of differential evolution in the relation (Ziegler et al. 2002; Böhm et al. 2004)—for example that the faintest galaxies evolve more rapidly—remains an important unknown.

Although the purpose of this study is to move beyond the TF relation, we begin by plotting the K-band TF relation for our sample (Figure 6.1). One might expect

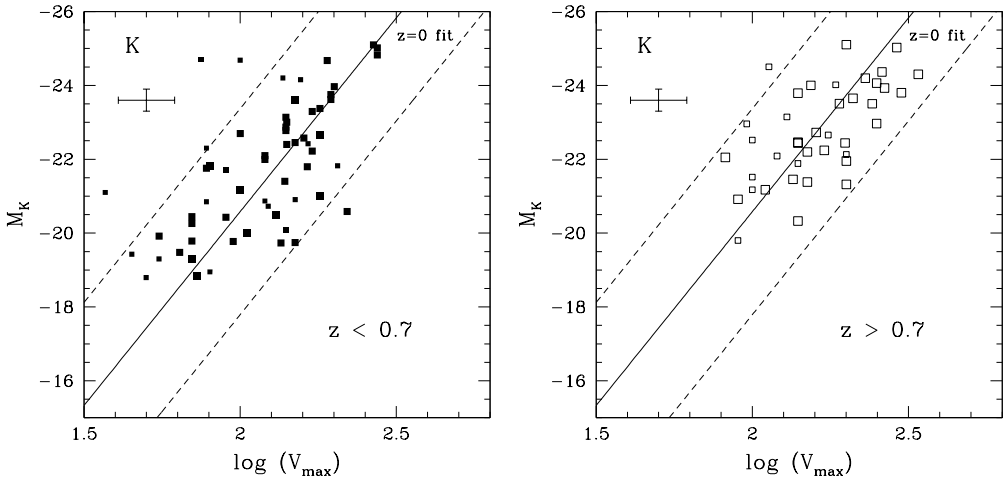

Figure 6.1 The restframe K-band Tully-Fisher relation for our sample of disks. The panels are divided into different redshift bins, higher and lower than $z = 0.7$. The solid and dashed lines are the $z \sim 0$ Tully-Fisher relation and its $\pm$ 3σ scatter found by Verheijen (2001). The average error is also plotted in each panel. The large points have errors lower than this average, while smaller points have errors larger than the average.

evolution of the TF relation in the K-band to display a clearer signal than the B-band since the effects of dust are mitigated, and passive evolution should be more uniform in its effect across the sample. When we assume that the slope of the K-band Tully-Fisher is the same as the local value from Verheijen (2001), we find no significant evolution, as is also found in the B-band (Vogt et al. 2005). We perform these fits using both a downhill simplex amoeba and Levenberg-Marquardt χ^2 minimization, both of which give the same results.

We find a fading of 0.04$\pm$0.24 magnitudes for systems at $z > 0.7$ compared with the $z \sim 0$ relationship and a brightening of 0.37$\pm$0.23 magnitudes for systems at $0.2 < z < 0.7$, consistent with no evolution. The scatter does not evolve significantly (1.13 magnitudes for the z <0.7 sample and 0.72 magnitudes for systems at $z > 0.7$). In all cases the observed slope and scatter change only slightly when we ignore internal extinction corrections.

Although our results are broadly consistent with earlier, smaller samples, the interpretation of any evolutionary signal is complicated in two ways. First, only a

limited range of luminosity and rotational velocity can be sampled at high redshift, leading to great uncertainties given the intrinsic scatter. Second, as luminosity and rotational velocity are indirect measures of the assembly state of the galaxy, both may be evolving in complex ways that mask actual evolutionary changes.

6.4.2 The Stellar Mass Tully-Fisher Relation

The first step beyond the TF relation is to compare the stellar mass to the measured maximum velocity - a relation we will call the *stellar mass - Tully Fisher relation*. The classical B-band TF relation scales such that $L \propto V^{3.5}$. This coupling becomes even steeper for the local stellar mass Tully-Fisher relation in nearby disks, $M \propto V^{4.5}$ (Bell & de Jong 2001).

Ideally, we seek to measure the all-inclusive baryonic TF relation, but measuring the gas content of high redshift disks is not yet feasible. We can estimate how much cold gas we are missing in our stellar mass inventory by investigating the gas mass fractions for nearby disk galaxies. Through examinations of the luminosities and HI masses for nearby disks, McGaugh & de Blok (1997) conclude that galaxies which are massive, bright, red, or have a high-surface brightness have very little gas in comparison to bluer, fainter, lower surface brightness systems. Systems which are brighter than $M_B = -21$ have gas mass fractions that are typically 0.1 or lower. Since our selection finds the most luminous, high surface brightness systems, which are also red, they are the least likely sub-class of disks to have a high gas content.

The stellar mass TF relation is shown in Figure 6.2 where, as before, we divide the sample into two redshift bins split at $z = 0.7$. Each panel contains a solid line giving the $z \sim 0$ best fit and a dashed line illustrating the $\pm$ 3 σ uncertainty in this fit (Bell & de Jong 2001). As was the case for the conventional TF relations, no significant evolution in the zero-point is observed. The Bell & de Jong (2001) $z = 0$ stellar mass Tully-Fisher relation can be written as $M_* = 0.52 + 4.49 \times \log(V_{max})$. By holding the slope of this relationship constant, we find that the zero point is best fit by 0.45$\pm$0.12 at $z < 0.7$ and 0.41$\pm$0.13 at $z > 0.7$. Neither of these, however, are

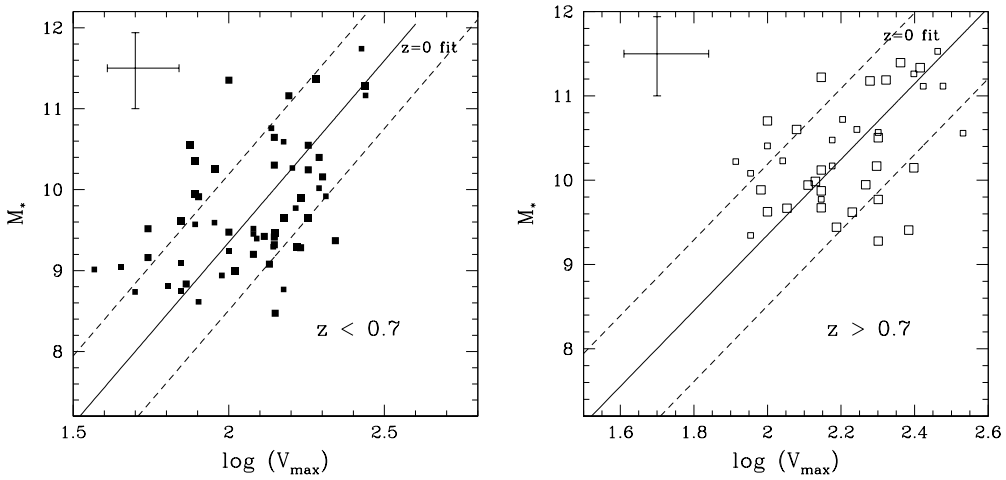

Figure 6.2 The stellar mass Tully-Fisher relation plotted as a relation between M_* and V_{max}. The solid and dashed line is the $z = 0$ relationship found by Bell & de Jong (2001) for nearly disks and its $\pm 3\sigma$ scatter. The error bar is the average with large points having errors lower than this average, and smaller points having errors larger than the average.

significantly different from the $z \sim 0$ relationship, and they are very similar to each other. This implies that, if growth continues, the stellar and dark components are growing together. For example, if disk assembly since $z \simeq 0.7$ proceeded only by the addition of stellar mass at a uniform rate of 4 $M_\odot$ year^{-1}, the local zero point would be discrepant at the 4σ level. This lack of evolution is important for understanding how disk galaxy formation is occurring (see §6.4.4).

Moreover, the scatter in the stellar mass Tully-Fisher relation is similar to that observed in the K-band Tully-Fisher after converting the K-band magnitude scatter into a luminosity and assuming an average stellar mass-to-light ratio. The typical scatter (in log M_* units) in stellar mass for these is 0.65 for disks at $z < 0.7$ and 0.48 for those at $z > 0.7$.

6.4.3 A Comparison of Stellar and Halo Masses

The final step in our analysis is an attempt to convert our measured quantities into a comparison of the stellar and halo masses as discussed in §6.3. Recognizing the considerable uncertainties involved, Figure 6.3 shows as a function of redshift the

ratio, $f_* = M_*/M_{vir}$, between the stellar masses and virial masses (eq. 6.1) within $3R_d$ for our sample. As expected, the stellar masses are nearly always less than the independently-derived virial masses, indicating that our methods for computing these values are not dominated by large systematic errors. It can also be seen from this figure that there is a wide range of M_*/M_{vir} values at every redshift from $z \sim 0.2-1.2$. The open pentagons show the median values of f_* as a function of redshift. The dotted horizontal line shows the global baryonic mass fraction $\Omega_b/\Omega_m = 0.171$ derived from WMAP results (Spergel et al. 2003). Within $3R_d$ it appears that many disks have M_*/M_{vir} values higher than this limit. It also appears that within $3R_d$ the stellar mass of the disk dominates the virial mass. This indicates that within the visual parts of some of our sample, the disk component accounts for roughly all the mass, which is consistent with a maximal disk interpretation. However, there are clear examples on Figure 6.3 where either the stellar mass is overestimated and/or the virial mass is underestimated. Both of these are possibilities, since our stellar masses are potentially too high from using a Salpeter IMF, and we might be underestimating the value of V_{max} due to seeing or a lack of depth in the LRIS observations. There is also a slight bias such that at higher redshifts nearly all galaxies sampled have high V_{max} values, which are likely maximal, while at lower redshifts we are sampling systems with lower V_{max} values that have not yet fully formed their stellar masses. This is likely part of the reason that the stellar mass to virial mass ratio increases slightly at higher redshifts.

However, we are also interested in constraining the relationship between the total halo mass, M_{halo}, and the total stellar mass, M_*. As we discuss in §6.3, it is very difficult to accurately obtain halo masses. We therefore show in Figure 6.4 total halo masses derived through eq. [6.1] at 100 kpc and through the semi-analytical approach (eq.6.2). Although we cannot accurately determine total halo masses for individual systems, our main goal is to compare how the ratio of stellar to halo mass changes with redshift. Figure 6.4 shows this relationship divided into the same redshift bins as in Figures 6.1 and 6.2. To first order, the halo masses and stellar masses of disk galaxies should correlate if star formation is regulated in the same manner in halos of

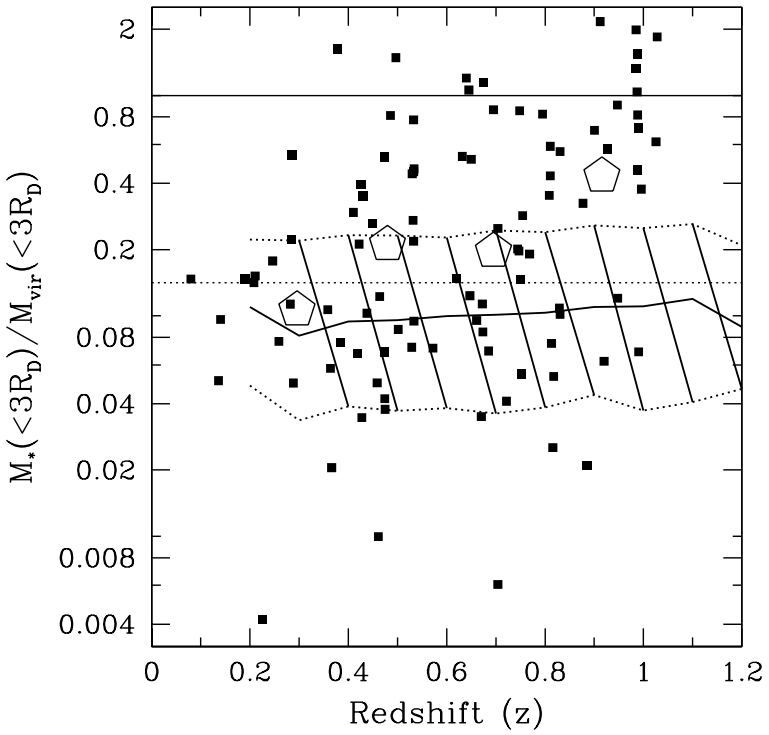

Figure 6.3 The relationship between the stellar mass and virial mass within $3R_D$ plotted as a function of redshift (z) for all galaxies in our sample. The pentagons show the average value of this ratio as a function of redshift. The solid horizontal line shows the location of $M_*(< R_d)$ / $M_{vir}(< R_d) = 1$, while the horizontal dotted line is the universal baryonic mass limit. The solid line surrounded by the hatched region shows the predictions of a hierarchical ΛCDM-based galaxy formation model (Baugh et al. 2005).

different masses (Steinmetz & Navarro 1999). Although there is no reason to expect any particular functional form between these two quantities, there is a reasonably well-fit linear relationship between them. We find that the zero point and slope of this relation do not change significantly between low and high redshift. There is also no obvious change in the scatter from high to low redshift (0.26 versus 0.32). The most significant outcome of Figures 6.3 and 6.4, however is the remarkable similarity in trends found at high and low redshift, suggesting that some disks had completed the bulk of their stellar assembly by $z \simeq 1$ or, more likely, that the stellar and dark masses of galaxies grow together.

Figure 6.5 shows the distribution of $f_* = M_*/M_{halo}$ for systems more massive than,

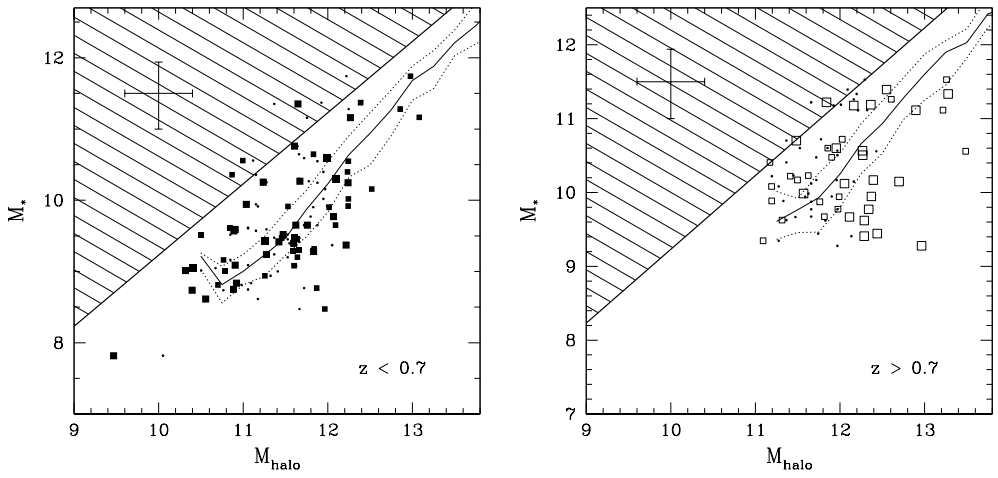

Figure 6.4 The relationship between stellar mass and halo mass in our two different redshift bins. The large symbols are for total masses derived from model relationships (eq. 6.2), and the small points are total halo masses derived using eq. [6.1] with $R =$ 100 kpc. The thin solid line is the relationship between stellar and virial masses from the semi-analytic models of Benson et al. (2002) at $z = 0.4$ for the $z < 0.7$ sample and at $z = 0.8$ for the $z > 0.7$ sample. The short dashed lines display the 80% range of where galaxies in these simulation are found. The thick solid line is the baryonic fraction limit, and the shaded region is the area where the stellar mass fraction is greater than the universal baryonic mass fraction.

and less massive than, the average halo mass, $M_{halo} = 10^{11.8}$ $M_{\odot}$. The solid line is the universal baryonic mass ratio. As mentioned earlier, most disk stellar mass fractions are lower than the cosmic ratio, which seems appropriate given that our stellar mass inventory is not intended to account for all associated baryons. Although some dispersion is expected, conceivably some fractions are overestimated or underestimated, for example by making incorrect assumptions about the IMF, or underestimating V_{max} (and hence M_{halo}) by insufficient sampling of the rotation curve.

Figure 6.5 also shows a tentative population of disk galaxies with remarkably low stellar fractions, the most extreme cases occurring in objects with halo masses $M_{vir} > 10^{11.8}$ $M_{\odot}$. These galaxies deviate from the $z = 0$ stellar mass TF relation by more than 4 σ. Investigation of the individual systems that lie in this category shows them to be undergoing vigorous star formation as inferred by bluer than average $(U - B)$ colors. A weak correlation was found between f_* and $(U - B)$. Because

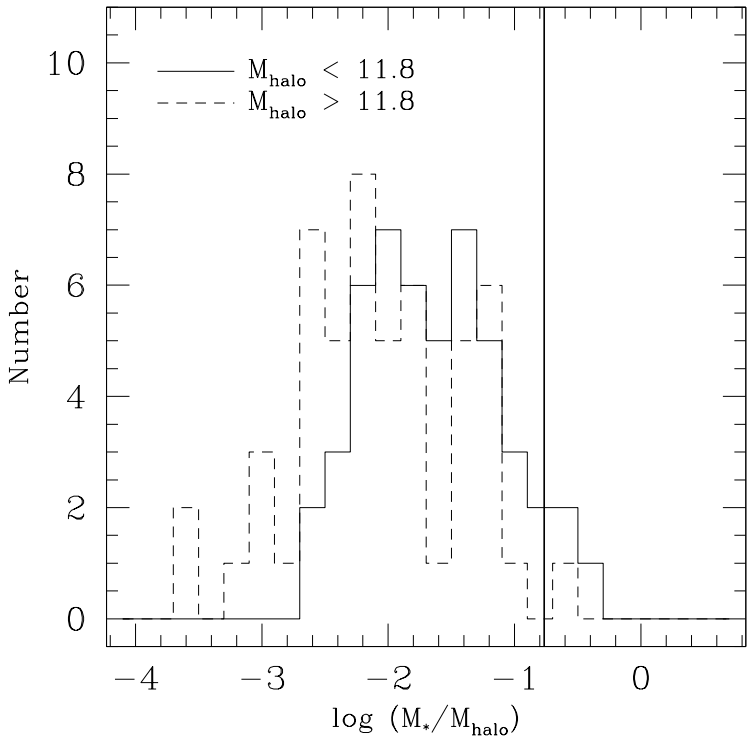

Figure 6.5 Histogram of M_*/M_{halo} values divided into disks of different virial masses. The solid line is the global baryonic mass fraction.

these systems are blue, they may have kinematic asymmetries in their rotation curves, which may raise their V_{max} values. However, this is unlikely to be the effect producing this slight correlation as most of the low f_* systems also have low V_{max} values. We investigated several other possible correlations involving f_* (for example with the bulge/disk ratio), but no significant trends were found.

6.4.4 Comparison with Models

To investigate the implications of our results for the assembly history of stellar mass in disk galaxies since $z \sim 1$, we return to the behavior of the stellar fraction $f_* = M_*(<3R_d)/M_{vir}(<3R_d)$ vs. redshift (Figure 6.3) and the relationship between total stellar mass (M_*) and halo mass (M_{halo}) at $z > 0.7$ and $z < 0.7$ (Figure 6.4). Trends in these relations may shed light on the physical processes regulating star formation in disk galaxies. This is only the case, however, if the value of R_d for disks does not

grow with time, which appears to be the case for the largest disks, based on our own limited data, and in statistical studies of $z > 0.8$ disks (Ravindranath et al. 2004; Conselice et al. 2004; Ferguson et al. 2004).

First, Figure 6.3 shows that the median stellar vs. virial mass value for our sample does not change significantly with redshift. We can compare two simple extreme models to this result to determine the likely method by which disk galaxies are forming at $z < 1$. In a "monolithic collapse" model, where the dark halo and baryons for a galaxy are in place at high redshift and there is no change in these mass components with time (e.g., Eggen et al. 1962), the average value of M_*/M_{vir} should increase with time. There is evolution in the monolithic model only in the sense that baryons are gradually converted to stars over time. This is the opposite to the observed trend in which the ratio of M_*/M_{vir} is roughly constant.

On the other hand, in a hierarchical picture the value of M_*/M_{vir} remains relatively constant with time. Shown in Figure 6.3 are model predictions from *Galform* that illustrate how the value of M_*/M_{vir} remains relatively constant with redshift. While we do not have a complete sample, we do find that the average and median values of M_*/M_{vir} for our sample remain constant with redshift within the errors, which is consistent with the hierarchical idea. The higher average M_*/M_{vir} value at $z > 0.8$ is likely produced by our selection of the brightest disks at these redshifts (Vogt et al. 2005). The *Galform* model, however, does not predict the full range of mass fractions that we find. At all redshifts there are systems dominated within R_d by their stellar masses, while some systems have low M_*/M_{vir} ratios. This is either produced by an observational bias (§6.4.3), or the simulations predict too much dark matter in the centers of disks.

Figure 6.4 shows the relationship between total stellar and total halo masses (see §6.3.1) for our sample, divided into our two redshift ranges. We also show on Figure 6.4 the *Galform* semi-analytic model values for this relationship for disk dominated galaxies with the 80% completeness indicated. No strong evolution in M_*/M_{halo} ratios is predicted. As galaxies in the semi-analytic models grow by accreting smaller systems, or intergalactic gas coupled with dark matter, and then quickly converting

the newly-obtained gas into stars, the relationship between M_* and M_{halo} remains constant. This is generally what we find, in addition to good agreement with the model predictions. In fact, the agreement between the total stellar and halo masses with the *Galform* models is slightly better than the comparison between the stellar and virial masses with $3\times R_d$, which further suggests that the luminous components of disk galaxies are dominated by the stellar mass (§6.4.3).

In summary, the fact that the ratio M_*/M_{halo} remains relatively constant in our sample with redshift, and that the stellar-mass TF relation does not evolve, are indications that disk galaxies are forming through the accretion of both dark and baryonic mass. Disk galaxies are undergoing star formation at $z < 1$ at a rate of a few solar masses per year. If disks at $z \sim 1$ contained all the baryonic or halo mass that they have at $z \sim 0$, we would see an increase in M_*/M_{halo} with time. Because we do not see this trend, it appears that new stars form out of gas accreted from the intergalactic medium which is coupled with dark matter at a constant ratio.

6.5 Conclusions

We present the results of a dynamical study of 101 disk galaxies drawn mostly from the DEEP1 survey with redshifts in the range $z \simeq$0.2-1.2. New infrared observations are presented which enable us to derive reliable stellar masses and thereby to construct the stellar mass Tully-Fisher relation and its redshift dependence. Using various formalisms drawn from analytic and semi-analytical models, we attempt to convert our dynamical data to make the first comparisons of the relative fractions of stellar and total mass in our sample. Notwithstanding the considerable uncertainties and sample incompleteness, the results are encouraging and suggest remarkably little evolution in the mix of baryons and dark matter since $z \simeq$1.

Although our sample is not formally complete in luminosity or mass, we explore the degree to which there may have been evolution in the relative distribution of stellar and virial masses and find the following:

1. Massive disk galaxies exist out to $z \sim 1$ with halo masses as large as 10^{13}

$M_\odot$, roughly as large as the most massive disks in the nearby universe. These systems also contain a large amount of stellar mass. At least some disk galaxies are nearly mature in their stellar content at $z \sim 1$.

2. We confirm earlier studies based on smaller samples and find no significant evolution in the zero-point or scatter of the restframe K-band Tully-Fisher relation out to $z \sim 1.2$.

3. The stellar mass Tully-Fisher relation out to $z \sim 1.2$ is likewise largely consistent with the relation found for nearby disks. We find no significant evolution in our sample after comparing systems at redshifts greater than and less than $z = 0.7$.

4. Although there are clearly great uncertainties in estimating total halo masses from our dynamical data, we find that the distribution of the ratio of stellar and halo masses remains relatively similar from $z \sim 0$ to $z \sim 1.2$. The stellar fraction observed can be understood if the bulk of the baryons associated with massive disk galaxies have already formed their stars. A modest number of massive galaxies have very low stellar fractions, consistent with continued star formation as revealed by their blue $U - B$ colors.

5. These results are in relatively good agreement with ΛCDM semi-analytical models (Benson et al. 2002; Baugh et al. 2005), suggesting that disk galaxy formation is hierarchical in nature.

Our primary conclusion from this study is that no significant evolution in the stellar mass fraction can be detected in the population of regular massive disks since $z \simeq 1$. Although biases and uncertain assumptions may affect detailed quantities at the $0.3 - 0.5$ dex level, the absence of gross trends is consistent with the conclusion that the bulk of these systems grow at $z < 1$ by the accretion of dark and baryonic material. This conclusion is, however, tempered by the fact that we are studying the brightest disks at high redshift.

Acknowledgments

We thank the DEEP team for generously enabling us to augment their optical sample and catalogs with near-infrared data in order to make this comparison. We also thank Dr. Cedric Lacey and Dr. Andrew Benson for access to their semi-analytical model simulation results, and Dr. Xavier Hernandez and Dr. Ken Freeman for comments regarding this work. CJC acknowledges support from a National Science Foundation Astronomy and Astrophysics Postdoctoral Fellowship. NPV is pleased to acknowledge support from NSF grants NSF-0349155 from the Career Awards program, NSF-0123690 via the Advance IT program at NMSU, and AST 95-29098 and 00-71198 administered at UCSC, and NASA STScI grants GO-07883.01-96A, AR-05801.01, AR-06402.01, and AR-07532.01.

Chapter 7

Conclusions

In this concluding chapter I synthesize the results presented in this thesis and place them in the context of our current understanding of how galaxies grow and evolve. I discuss the new questions that have been raised by this work and outline ongoing as well as future work that will help to address them.

7.1 Synthesis

Through the analysis of a large sample of distant galaxies with spectroscopic redshifts and near-IR photometry, the previous chapters in this thesis provide a broad and consistent picture of the final phase of assembly and evolution in field galaxies with stellar masses greater than $\sim 10^{10} M_{\odot}$. One of the key results is that such galaxies are largely established and have completed the bulk of their assembly by $z \sim 1$. This is evident in the lack of strong evolution in the total mass functions presented in Chapters 3 and 4 and is also suggested by the relatively low merger accretion rate discussed in Chapter 5. This conclusion was perhaps not unexpected given previous efforts (e.g., Dickinson et al. 2003; Fontana et al. 2003; Drory et al. 2004a; Fontana et al. 2004), but the large sample size, cosmic volume, and unique combination of spectroscopy and IR observations analyzed in this work establishes this result unequivocally.

If the stellar content of intermediate to high-mass galaxies is largely in place by $z \sim 1$, the formation epoch of such systems must have occurred earlier. Indeed, early results from observations at $z \gtrsim 1.5$ are beginning to confirm this. Juneau

et al. (2005), for example, find that galaxies with $M_* \gtrsim 10^{10}\mathrm{M}_\odot$ exhibit a burst mode of star formation before $z \approx 1.3$ but become largely quiescent after, and more massive galaxies seem to exit this burst mode at earlier times. This is consistent with the masses of star-forming Lyman break galaxies (Shapley et al. 2005) and sub-mm sources (Blain et al. 1999) at $z \sim 2$ and the existence of even more massive ($M_* > 10^{11}\mathrm{M}_\odot$), but often quiescent distant red galaxies (DRGs) at $z \gtrsim 2$ (e.g., Franx et al. 2003; van Dokkum et al. 2006).

The star formation characteristics of massive galaxies at $z \gtrsim 1$ combined with the small amount of growth in stellar mass since $z \sim 1$, as well as observations of the global SFR (Hopkins 2004) all suggest that massive galaxies form the bulk of their stellar populations at $z \sim 2$. The next question is why this peak of activity occurs when it does and what initiates the order of magnitude decline in the global SFR after $z \sim 1$. Naively, an obvious answer is that galaxies form stars rapidly after an initial collapse and then simply exhaust their fuel supply. Large numbers of galaxies are still forming stars at $z = 0$ (including our own), however, and observations demonstrate the existence of large gas reservoirs with relatively short cooling times (the "cooling flow" problem, see Fabian 1994). Instead, a specific mechanism capable of expelling or heating the gas in galaxy halos so that further star formation is inhibited seems to be required.

The second major contribution from this work is a series of observations that shed light on what this mechanism is and how it operates. Although there is little evolution in the total mass function since $z \sim 1$, significant changes in the make-up and characteristics of the galaxy population do occur. In large part, these changes result from a shift in the demographics of star-forming galaxies which is evident when the galaxy population is partitioned by diagnostics such as restframe color, star formation rate, and morphological type. These diagnostics reveal a pattern commonly referred to as "downsizing" in which the galaxies exhibiting late-type morphologies and ongoing star formation shift to systems with lower masses as a function of cosmic time. By detailing the behavior of downsizing and quantifying its effect on galaxies, it is possible to explore the physical process that is ultimately responsible for suppressing

the global SFR and driving galaxy evolution.

7.2 Physical Interpretation

There are three key observations presented in the previous chapters that reveal the nature of downsizing and provide insight on what quenches star formation in galaxies. First, the mass distribution of the galaxy population is bimodal out to $z \sim 1$. The more massive population exhibits red colors, low star formation rates, and early-type morphologies, while the less massive population exhibits blue colors, moderate to high star formation rates, and late-type morphologies. The well-defined red portion of the bimodal distribution suggests that star formation in this population is efficiently quenched—only a small amount of recent star formation is necessary to turn galaxy colors (e.g. $U - B$) blue. Second, the mass scale that defines the bimodality shifts downward with time, providing a useful way of characterizing downsizing. Because this evolution occurs while the total mass function remains static suggests that massive star-forming galaxies experience a quenching of star formation followed by a transformation into systems with early-type morphologies. Finally, for the majority of the field population, downsizing exhibits only a weak dependence on environmental density. This suggests that the mechanism that drives it is primarily internal and not related to cluster-like phenomena such as harassment or ram-pressure stripping.

In Chapters 3 and 4, two new diagnostics were introduced with the aim of quantifying the behavior of downsizing and providing constraints on its physical nature. The transition mass, M_{tr}, is defined as that stellar mass at which the red, spheroidal population has the same abundance as the blue, late-type population. While it is easy to define, M_{tr} is often near the completeness limit of current surveys and is difficult to interpret. A more physically meaningful quantity is the quenching mass, M_Q, above which star formation in galaxies is effectively suppressed. The quenching mass decreases by a factor of $\sim$5 over the interval $0.4 < z < 1.4$, offering a key constraint on possible mechanisms capable of driving this evolution.

A strong candidate has been recently emphasized in theoretical considerations

based on the ΛCDM framework. This mechanism is AGN feedback. Early results suggest this process is capable of providing the energy required to quench star formation in massive galaxies (e.g., Dekel & Birnboim 2004; Croton et al. 2005; Bower et al. 2005; Hopkins et al. 2005a; Scannapieco et al. 2005) and convert them into passive systems. Indeed, the latest semi-analytic models incorporating AGN feedback are able to produce massive quiescent galaxies (e.g., Croton et al. 2005; De Lucia et al. 2005) and match observations of the stellar mass function (Bower et al. 2005) for the first time. The mechanism works as follows: central black holes are ignited as AGN in major mergers. For halos in which the gas cooling time, t_{cool}, is longer than the dynamical time, t_{dyn}, the galaxy enters a "radio mode" in which low-level energy from the AGN is effectively coupled to the gas, keeping it from cooling and forming stars (see Dekel & Birnboim 2004; Croton et al. 2005).

Although AGN feedback satisfies the requirement for an internal process capable of quenching star formation, it is not yet clear if it is fully capable of driving the evolution described in this work. The current implementation of AGN feedback has not yet generated models that predict the correct evolution in the bimodal galaxy distribution (Croton, priv. communication) or the early assembly time of massive spheroidals (De Lucia et al. 2005). In principle, AGN-driven downsizing would result from the declining mass scale of halos in which $t_{cool} > t_{dyn}$ and the feedback energy can efficiently couple to the gas. Because the physical nature of this coupling is unknown, the prescriptions used by modelers to describe AGN feedback are probably too simplistic. Theorists are hopeful that future models informed by quantitative constraints—such as the behavior of M_Q presented in this work—will better match observations of downsizing.

A more difficult problem may be understanding the connection between AGN feedback, mergers, and morphological evolution. Based on numerical simulations, it is widely accepted that major mergers are responsible for the development of galaxies with spheroidal configurations (e.g., Barnes & Hernquist 1991). At the same time, AGN feedback is thought to be initiated by gas-rich mergers that funnel fuel to the central engine (e.g., Hopkins et al. 2005b). If these two ideas are correct, it is expected

that AGN-driven quenching would coincide with morphological transformation, and the evidence presented in Chapter 3 and 4 suggests this is qualitatively correct. In detail, however, the quenching of star formation and reddening appears to occur *before* galaxies acquire spheroidal morphologies; this is demonstrated by the higher mass scale that defines morphological downsizing. There are two apparent solutions. Either morphological evolution takes place on a longer timescale than quenching or mergers that trigger AGN do not always create spheroidals. In fact, while the discussion here has focused on the transformation of blue, late-types into red, early-types (mainly because it is the abundance the red, early-types that grows with time), it should be noted that episodes of new star formation in red sources could periodically transform galaxies in the opposite direction. This level of complexity has yet to be accounted for in semi-analytic models.

7.3 Ongoing and Future Work

7.3.1 AGN Feedback

As described in the previous section, the observations in this thesis point to an internal mechanism acting within galaxies that quenches star formation and drives downsizing, resulting in the decline of the global SFR. This is a timely result considering rapid theoretical progress in exploring whether AGN feedback satisfies the requirements for this mechanism. Clearly the next step in testing this solution is more direct observations that can tie AGN to the evolution seen in the galaxy population. Already such studies are beginning to appear.

In a paper with Phil Hopkins (Hopkins et al. 2006) we compare the results of Chapters 4 to previous measurements of the transition mass, M_{tr}, and find good agreement. Then, as shown in Figure 7.1, these measurements are compared to the inferred stellar mass of galaxies hosting quasars at the break in the quasar luminosity function. Using both direct observations of quasars as well as predictions from the merger-AGN model described in Hopkins et al. (2005a), we show that the transition

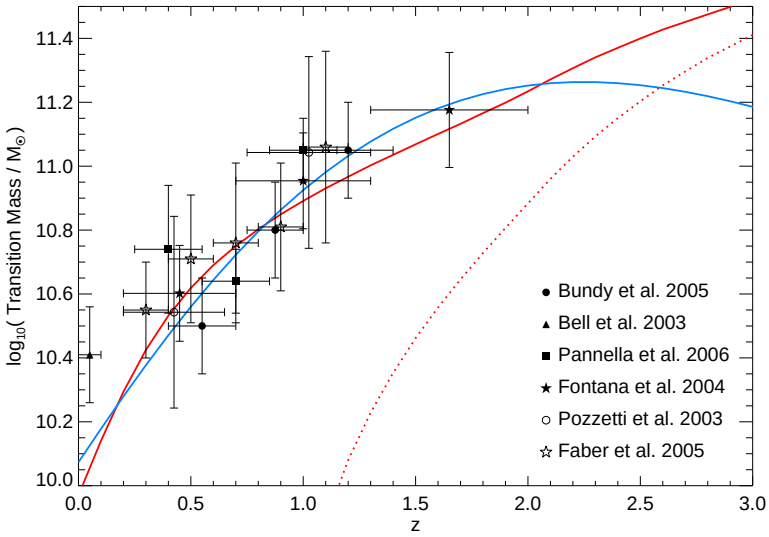

Figure 7.1 A comparison of measurements of M_{tr} compiled by Hopkins et al. (2006) to the mass scale inferred for galaxies hosting quasars at the break of the quasar luminosity function. The red curve comes from estimates based on the luminosity of host galaxies near the break. The blue curve illustrates the prediction from the Hopkins merger-AGN feedback model. The dotted curve shows the same prediction without AGN feedback.

mass agrees with the inferred AGN feedback mass scale. Finally, we show that the current best estimates of the typical stellar mass of galaxies undergoing merging, while very uncertain, also agree with M_{tr} and the mass scale associated with AGN feedback, suggestive of a link between merging, AGN, and galaxy evolution.

Ongoing work with Chandra X-ray observations in the EGS is providing a more direct test of the connection between galaxy evolution and the presence of AGN. Figure 7.2 shows a preliminary result from a study being led by Paul Nandra. Here, I have plotted as a function of redshift the stellar masses of galaxies (most with spectroscopic redshifts from DEEP2) that harbor AGN as determined by Chandra X-ray detections (with $L_X < 10^{44}$ ergs/s). The dotted line shows a simple linear fit to the data. Overplotted with asterisk symbols and connected by a solid line is the value of M_Q measured in Chapter 4. The agreement between M_Q and mass of AGN host galaxies is one of the first direct measurements of the association between the quenching of star-forming galaxies and the presence of AGN.

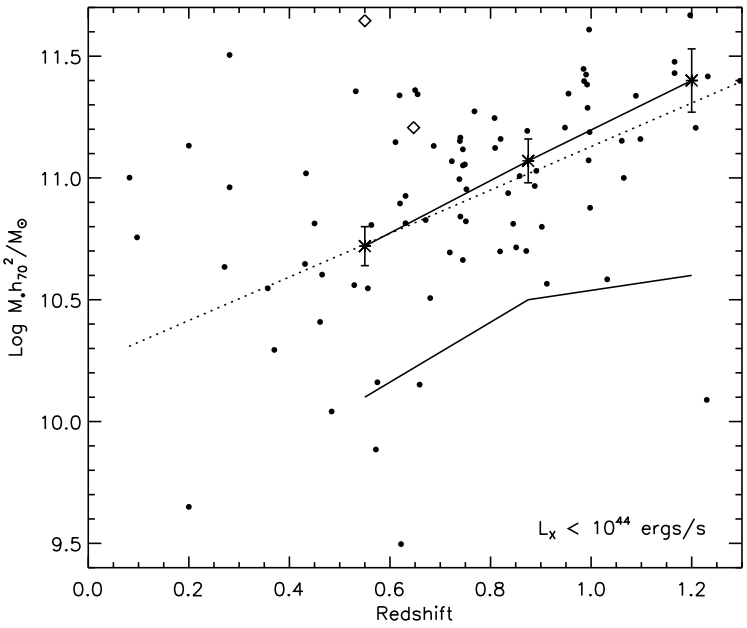

Figure 7.2 The stellar mass of galaxies hosting AGN as determined by Chandra X-ray observations as a function of redshift. The dotted line shows a linear fit to the data. Overplotted with asterisk symbols connected by a solid line are the values of M_Q determined in Chapter 4. The lower solid line illustrates the estimated mass completeness limit of the sample. The stellar mass estimates shown here have not been corrected for the AGN contribution to the host luminosity in the near-IR.

The two studies described above explore convincing but circumstantial evidence for the AGN feedback scenario. Verifying this picture conclusively, however, will require detailed observations of individual galaxies in the midst of transition so that the physical mechanism driving it can determined. In particular, it will be important to understand how energy liberated by the AGN couples with gas in the halo. One promising observational approach in this respect is adaptive optics imaging and integral field studies that have the potential to detail the small scale morphology and emission properties of gas near the central black hole. A key test will be to see if the energy output of AGN, as detected in winds for example, is enough to unbind or heat the gas in the halo and prevent further star formation.

7.3.2 Merging

While the paper by Hopkins et al. (2006) makes a first attempt to connect the mass scale of AGN feedback to the mass scale of merging, further insight is limited by our inability to place strong constraints on merging. This is unfortunate, especially because mergers play such an important role in the AGN feedback picture, as discussed previously, and in the hierarchical build-up predicted by ΛCDM models more generally.

Chapter 5 presented results that demonstrate the power of near-IR merger studies capable of tracing the stellar mass involved in merging directly. Thankfully, further progress is now possible with studies that make use of new IR instruments. In one such project, I am working with Masataka Fukugita to exploit the large field-of-view ($4'' \times 7''$) of the new MOIRCS IR camera on the Subaru Telescope to extend our previous work (Chapter 5) by a factor of 6–10 in sample size. Continuing the strategy of imaging HST fields to very deep limits in the K-band, the goals are to measure the merger rate as a function of morphological type and to constrain the shape of the stellar mass function of merging galaxies. Achieving these goals will test the role of merging in the evolution and assembly of galaxies since $z \sim 1$.

7.3.3 Disk Rotation Curves

Much of the interpretation of the observations described in this thesis as well as the theoretical motivation for AGN feedback has relied on the assumption of a ΛCDM framework as the basis for the growth of structure and formation of galaxies in the universe. While this framework—and galaxy models based on it—reproduces a large number of observations, it is important to test the assumptions it makes about the behavior of dark matter. As described in Chapter 6, the rotation curves of disk galaxies provide one method for doing this.

Such detailed spectroscopic studies at high redshift are very challenging, however and, as seen in Chapter 6, are limited by the quality of observations. To make progress, over the last two years, we have obtained deep DEIMOS spectra for a sample

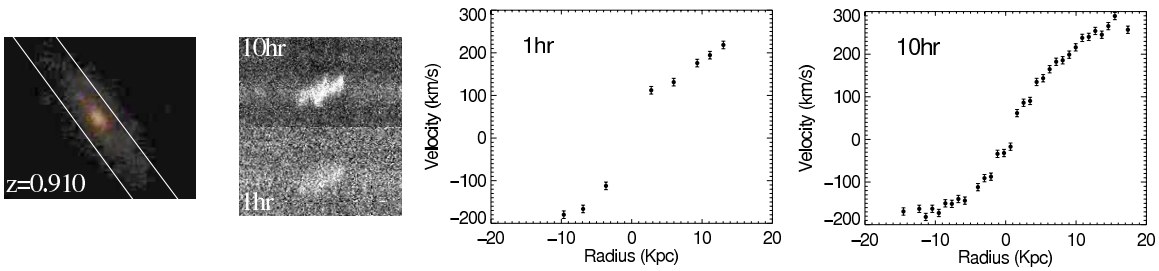

Figure 7.3 Example from a sample of disk galaxies in GOODS of the improvement in rotation curves obtained in 10-hour versus 1-hour integrations with DEIMOS. The HST image and the [OII] feature from the 2D spectra are also shown. Identifying the V_{max} turnover point in 10-hour rotation curves like the one showed here will greatly improve estimates of M_*/M_{halo} at $z \sim 1$

of ≈120 disk galaxies out to $z \sim 1$ at Keck Observatory. These 8-hour integrations promise a significant improvement over previous rotation curve studies at high redshift (e.g Vogt et al. 1996; Böhm et al. 2004) as shown in Figure 7.3. The goal is to achieve a fidelity in the data that approaches comparable studies at $z = 0$. By comparing the dynamical masses inferred from such rotation curves to near-IR stellar masses determined from Palomar K_s-band photometry it will be possible to vastly improve upon the work presented in Conselice et al. (2005). Such high quality observations will have the sensitivity to probe evolution in the stellar mass Tully-Fisher relation, providing valuable constraints on disk galaxy feedback processes and, more generally, the relationship between stellar and total mass in field galaxies.

Bibliography

Abadi, M. G., Navarro, J. F., Steinmetz, M., & Eke, V. R. 2003, ApJ, 591, 499

Abraham, R. G., van den Bergh, S., Glazebrook, K., Ellis, R. S., Santiago, B. X., Surma, P., & Griffiths, R. E. 1996, ApJS, 107, 1

Abraham, R. G. et al. 2004, AJ, 127, 2455

Baldry, I. K., Glazebrook, K., Brinkmann, J., Ivezić, Ž., Lupton, R. H., Nichol, R. C., & Szalay, A. S. 2004, ApJ, 600, 681

Bardeen, J. M., Bond, J. R., Kaiser, N., & Szalay, A. S. 1986, ApJ, 304, 15

Barnes, J. E. & Hernquist, L. E. 1991, ApJ, 370, L65

Bauer, A. E., Drory, N., Hill, G. J., & Feulner, G. 2005, ApJ, 621, L89

Baugh, C. M., Cole, S., & Frenk, C. S. 1996, MNRAS, 283, 1361

Baugh, C. M., Cole, S., Frenk, C. S., & Lacey, C. G. 1998, ApJ, 498, 504

Baugh, C. M., Lacey, C. G., Frenk, C. S., Granato, G. L., Silva, L., Bressan, A., Benson, A. J., & Cole, S. 2005, MNRAS, 356, 1191

Bell, E. F. & de Jong, R. S. 2001, ApJ, 550, 212

Bell, E. F., McIntosh, D. H., Katz, N., & Weinberg, M. D. 2003, ApJS, 149, 289

Bell, E. F., Wolf, C., Meisenheimer, K., Rix, H.-W., Borch, A., Dye, S., Kleinheinrich, M., Wisotzki, L., & McIntosh, D. H. 2004, ApJ, 608, 752

Bell, E. F. et al. 2005a, preprint (astro-ph/0506425)

—. 2005b, ApJ, 625, 23

Benítez, N. 2000, ApJ, 536, 571

Benson, A. J., Bower, R. G., Frenk, C. S., Lacey, C. G., Baugh, C. M., & Cole, S. 2003, ApJ, 599, 38

Benson, A. J., Lacey, C. G., Baugh, C. M., Cole, S., & Frenk, C. S. 2002, MNRAS, 333, 156

Bertin, E. & Arnouts, S. 1996, A&AS, 117, 393

Birnboim, Y. & Dekel, A. 2003, MNRAS, 345, 349

Blain, A. W., Smail, I., Ivison, R. J., & Kneib, J.-P. 1999, MNRAS, 302, 632

Blumenthal, G. R., Faber, S. M., Primack, J. R., & Rees, M. J. 1984, Nature, 311, 517

Böhm, A. et al. 2004, A&A, 420, 97

Bolton, A. S., Burles, S., Koopmans, L. V. E., Treu, T., & Moustakas, L. A. 2005, ArXiv Astrophysics e-prints

Bouwens, R. J. et al. 2003, ApJ, 595, 589

Bower, R. G. et al. 2005, ArXiv Astrophysics e-prints

Brinchmann, J. 1999, Ph.D. Thesis

Brinchmann, J. & Ellis, R. S. 2000, ApJ, 536, L77

Brinchmann, J. et al. 1998, ApJ, 499, 112

Broadhurst, T. J., Ellis, R. S., & Glazebrook, K. 1992, Nature, 355, 55

Broadhurst, T. J., Ellis, R. S., & Shanks, T. 1988, MNRAS, 235, 827

Bromley, B. C., Press, W. H., Lin, H., & Kirshner, R. P. 1998, ApJ, 505, 25

Bruzual, G. & Charlot, S. 2003, MNRAS, 344, 1000

Bundy, K., Ellis, R. S., & Conselice, C. J. 2005a, ApJ, 625, 621

Bundy, K., Fukugita, M., Ellis, R. S., Kodama, T., & Conselice, C. J. 2004, ApJ, 601, L123

Bundy, K. et al. 2005b, submitted to ApJ, astro-ph/0512465

Bunker, A. J., Stanway, E. R., Ellis, R. S., & McMahon, R. G. 2004, MNRAS, 355, 374

Burkey, J. M., Keel, W. C., Windhorst, R. A., & Franklin, B. E. 1994, ApJ, 429, L13

Butcher, H. & Oemler, A. 1978, ApJ, 219, 18

Calzetti, D. 1997, AJ, 113, 162

Carlberg, R. G. 1992, ApJ, 399, L31

Carlberg, R. G. & Charlot, S. 1992, ApJ, 397, 5

Carlberg, R. G., Pritchet, C. J., & Infante, L. 1994, ApJ, 435, 540

Chabrier, G. 2003, PASP, 115, 763

Chapman, S. C., Blain, A. W., Ivison, R. J., & Smail, I. R. 2003, Nature, 422, 695

Chapman, S. C., Blain, A. W., Smail, I., & Ivison, R. J. 2005, ApJ, 622, 772

Charlot, S., Worthey, G., & Bressan, A. 1996, ApJ, 457, 625

Chen, H.-W. et al. 2002, ApJ, 570, 54

Cimatti, A. et al. 2002, A&A, 392, 395

Cohen, J. G. 2002, ApJ, 567, 672

Coil, A. L., Newman, J. A., Kaiser, N., Davis, M., Ma, C.-P., Kocevski, D. D., & Koo, D. C. 2004, ApJ, 617, 765

Cole, S., Lacey, C. G., Baugh, C. M., & Frenk, C. S. 2000, MNRAS, 319, 168

Cole, S. et al. 2001, MNRAS, 326, 255

Colless, M., Ellis, R. S., Taylor, K., & Hook, R. N. 1990, MNRAS, 244, 408

Collister, A. A. & Lahav, O. 2004, PASP, 116, 345

Conselice, C. J. 2003, ApJS, 147, 1

Conselice, C. J., Bershady, M. A., Dickinson, M., & Papovich, C. 2003, AJ, 126, 1183

Conselice, C. J., Bundy, K., Ellis, R. S., Brichmann, J., Vogt, N. P., & Phillips, A. C. 2005, ApJ, 628, 160

Conselice, C. J. et al. 2004, ApJ, 600, L139

Cooper, M. C., Newman, J. A., Madgwick, D. S., Gerke, B. F., Yan, R., & Davis, M. 2005, preprint (astro-ph/0506518)

Cooper, M. C. et al. 2006, MNRAS, submitted

Cooray, A. & Milosavljević, M. 2005a, ApJ, 627, L85

—. 2005b, ApJ, 627, L89

Cowie, L. L., Gardner, J. P., Hu, E. M., Songaila, A., Hodapp, K.-W., & Wainscoat, R. J. 1994, ApJ, 434, 114

Cowie, L. L., Songaila, A., & Barger, A. J. 1999, AJ, 118, 603

Cowie, L. L., Songaila, A., Hu, E. M., & Cohen, J. G. 1996, AJ, 112, 839

Cross, N. et al. 2001, MNRAS, 324, 825

Croton, D. J. et al. 2005, preprint (astro-ph/0508046)

Cuillandre, J.-C., Luppino, G., Starr, B., & Isani, S. 2001, in SF2A-2001: Semaine de l'Astrophysique Francaise, 605–+

Davis, M., Efstathiou, G., Frenk, C. S., & White, S. D. M. 1985, ApJ, 292, 371

Davis, M. & Peebles, P. J. E. 1983, ApJ, 267, 465

Davis, M. et al. 2003, in Discoveries and Research Prospects from 6- to 10-Meter-Class Telescopes II. Edited by Guhathakurta, Puragra. Proceedings of the SPIE, Volume 4834, pp. 161-172 (2003)., 161–172

de Jong, R. S. 1996, A&A, 313, 377

De Lucia, G., Springel, V., White, S. D. M., Croton, D., & Kauffmann, G. 2005, preprint (astro-ph/0509725)

De Lucia, G. et al. 2004, ApJ, 610, L77

Dekel, A. & Birnboim, Y. 2004, preprint (astro-ph/0412300)

Dickinson, M., Papovich, C., Ferguson, H. C., & Budavári, T. 2003, ApJ, 587, 25

Djorgovski, S. et al. 1995, ApJ, 438, L13

Dressler, A. 1980, ApJ, 236, 351

Driver, S. P., Fernandez-Soto, A., Couch, W. J., Odewahn, S. C., Windhorst, R. A., Phillips, S., Lanzetta, K., & Yahil, A. 1998, ApJ, 496, L93+

Driver, S. P., Windhorst, R. A., & Griffiths, R. E. 1995a, ApJ, 453, 48

Driver, S. P., Windhorst, R. A., Ostrander, E. J., Keel, W. C., Griffiths, R. E., & Ratnatunga, K. U. 1995b, ApJ, 449, L23+

Drory, N., Bender, R., Feulner, G., Hopp, U., Maraston, C., Snigula, J., & Hill, G. J. 2004a, ApJ, 608, 742

Drory, N., Bender, R., & Hopp, U. 2004b, ApJ, 616, L103

Drory, N., Feulner, G., Bender, R., Botzler, C. S., Hopp, U., Maraston, C., Mendes de Oliveira, C., & Snigula, J. 2001, MNRAS, 325, 550

Eggen, O. J., Lynden-Bell, D., & Sandage, A. R. 1962, ApJ, 136, 748

Ellis, R. S. 1997, ARA&A, 35, 389

Ellis, R. S., Colless, M., Broadhurst, T., Heyl, J., & Glazebrook, K. 1996, MNRAS, 280, 235

Faber, S. M. & Jackson, R. E. 1976, ApJ, 204, 668

Faber, S. M. et al. 2003, in Instrument Design and Performance for Optical/Infrared Ground-based Telescopes. Edited by Iye, Masanori; Moorwood, Alan F. M. Proceedings of the SPIE, Volume 4841, pp. 1657-1669 (2003)., 1657–1669

Faber, S. M. et al. 2005, preprint (astro-ph/0506044)

Fabian, A. C. 1994, ARA&A, 32, 277

Fall, S. M., Charlot, S., & Pei, Y. C. 1996, ApJ, 464, L43+

Ferguson, H. C. et al. 2004, ApJ, 600, L107

Flores, H. et al. 1999, ApJ, 517, 148

Fontana, A. et al. 2003, ApJ, 594, L9

—. 2004, A&A, 424, 23

Franceschini, A., Silva, L., Fasano, G., Granato, G. L., Bressan, A., Arnouts, S., & Danese, L. 1998, ApJ, 506, 600

Franx, M. et al. 2003, ApJ, 587, L79

Fukugita, M., Hogan, C. J., & Peebles, P. J. E. 1998, ApJ, 503, 518

Fukugita, M., Yamashita, K., Takahara, F., & Yoshii, Y. 1990, ApJ, 361, L1

Gardner, J. P., Cowie, L. L., & Wainscoat, R. J. 1993, ApJ, 415, L9

Gebhardt, K. et al. 2003, ApJ, 597, 239

Giavalisco, M., Livio, M., Bohlin, R. C., Macchetto, F. D., & Stecher, T. P. 1996, AJ, 112, 369

Giavalisco, M. et al. 2004, ApJ, 600, L93

Glazebrook, K., Ellis, R., Santiago, B., & Griffiths, R. 1995, MNRAS, 275, L19

Glazebrook, K., Peacock, J. A., Collins, C. A., & Miller, L. 1994, MNRAS, 266, 65

Glazebrook, K., Peacock, J. A., Miller, L., & Collins, C. A. 1991, Advances in Space Research, 11, 337

Gottlöber, S., Klypin, A., & Kravtsov, A. V. 2001, ApJ, 546, 223

Granato, G. L., De Zotti, G., Silva, L., Bressan, A., & Danese, L. 2004, ApJ, 600, 580

Gronwall, C. & Koo, D. C. 1995, ApJ, 440, L1

Groth, E. J., Kristian, J. A., Lynds, R., O'Neil, E. J., Balsano, R., Rhodes, J., & WFPC-1 IDT. 1994, Bulletin of the American Astronomical Society, 26, 1403

Gunn, J. E. 1982, in Astrophysical Cosmology Proceedings, 233–259

Guzman, R., Gallego, J., Koo, D. C., Phillips, A. C., Lowenthal, J. D., Faber, S. M., Illingworth, G. D., & Vogt, N. P. 1997, ApJ, 489, 559

Gwyn, S., Hartwick, F. D. A., Kanwar, A., Schade, D., & Simard, L. 2005, preprint (astro-ph/0510149)

Hammer, F., Flores, H., Elbaz, D., Zheng, X. Z., Liang, Y. C., & Cesarsky, C. 2005, A&A, 430, 115

Haynes, M. P., Giovanelli, R., Chamaraux, P., da Costa, L. N., Freudling, W., Salzer, J. J., & Wegner, G. 1999, AJ, 117, 2039

Heavens, A., Panter, B., Jimenez, R., & Dunlop, J. 2004, Nature, 428, 625

Heyl, J., Colless, M., Ellis, R. S., & Broadhurst, T. 1997, MNRAS, 285, 613

Hogg, D. W. et al. 2000, ApJS, 127, 1

Hopkins, A. M. 2004, ApJ, 615, 209

Hopkins, P. F., Bundy, K., Hernquist, L., & Ellis, R. S. 2006, ArXiv Astrophysics e-prints

Hopkins, P. F., Hernquist, L., Cox, T. J., Robertson, B., & Springel, V. 2005a, preprint (astro-ph/0508167)

Hopkins, P. F. et al. 2005b, ApJ, 630, 705

Huang, J.-S. et al. 2001, A&A, 368, 787

Hubble, E. P. 1925, ApJ, 62, 409

Ilbert, O. et al. 2005, A&A, 439, 863

Jimenez, R., Panter, B., Heavens, A. F., & Verde, L. 2005, MNRAS, 356, 495

Jorgensen, I., Franx, M., & Kjaergaard, P. 1996, MNRAS, 280, 167

Juneau, S. et al. 2005, ApJ, 619, L135

Kaiser, N., Squires, G., & Broadhurst, T. 1995, ApJ, 449, 460

Kant, I. orig. 1755, Universal History and Theory of the Heavens (University of Michigan Press, 1969, trans. W. Hastie Glasgow)

Kashikawa, N. et al. 2003, AJ, 125, 53

Kauffmann, G. 1996, MNRAS, 281, 487

Kauffmann, G. & Charlot, S. 1998, MNRAS, 297, L23+

Kauffmann, G. et al. 2003a, MNRAS, 341, 33

—. 2003b, MNRAS, 341, 54

Kewley, L. J., Geller, M. J., & Jansen, R. A. 2004, AJ, 127, 2002

Kinney, A. L., Calzetti, D., Bohlin, R. C., McQuade, K., Storchi-Bergmann, T., & Schmitt, H. R. 1996, ApJ, 467, 38

Kirshner, R. P., Oemler, A., Schechter, P. L., & Shectman, S. A. 1983, AJ, 88, 1285

Koo, D. C. & Kron, R. G. 1992, ARA&A, 30, 613

Kormendy, J. 1977, ApJ, 218, 333

Kron, R. G. 1993, in The Deep Universe: Saas-Fee Advanced Course 23, ed. B. Binggeli & R. Buser

Kuchinski, L. E., Madore, B. F., Freedman, W. L., & Trewhella, M. 2001, AJ, 122, 729

Kuchinski, L. E. et al. 2000, ApJS, 131, 441

Labbé, I. et al. 2003, AJ, 125, 1107

Lacey, C. & Cole, S. 1993, MNRAS, 262, 627

Le Fèvre, O. et al. 2000, MNRAS, 311, 565

Le Fèvre, O. et al. 2004, A&A, 428, 1043

Lilly, S. J., Le Fevre, O., Crampton, D., Hammer, F., & Tresse, L. 1995a, ApJ, 455, 50

Lilly, S. J., Le Fevre, O., Hammer, F., & Crampton, D. 1996, ApJ, 460, L1+

Lilly, S. J., Tresse, L., Hammer, F., Crampton, D., & Le Fevre, O. 1995b, ApJ, 455, 108

Lin, H., Kirshner, R. P., Shectman, S. A., Landy, S. D., Oemler, A., Tucker, D. L., & Schechter, P. L. 1996, ApJ, 464, 60

Lin, H., Yee, H. K. C., Carlberg, R. G., Morris, S. L., Sawicki, M., Patton, D. R., Wirth, G., & Shepherd, C. W. 1999, ApJ, 518, 533

Lin, L. et al. 2004, ApJ, 617, L9

Lotz, J. M. et al. 2006, ArXiv Astrophysics e-prints

Loveday, J., Peterson, B. A., Efstathiou, G., & Maddox, S. J. 1992, ApJ, 390, 338

Madau, P., Ferguson, H. C., Dickinson, M. E., Giavalisco, M., Steidel, C. C., & Fruchter, A. 1996, MNRAS, 283, 1388

Madau, P., Pozzetti, L., & Dickinson, M. 1998, ApJ, 498, 106

Marzke, R. O. & da Costa, L. N. 1997, AJ, 113, 185

Matthews, K. & Soifer, B. T. 1994, Experimental Astronomy, 3, 77

McCracken, H. J., Metcalfe, N., Shanks, T., Campos, A., Gardner, J. P., & Fong, R. 2000, MNRAS, 311, 707

McGaugh, S. & de Blok, E. 1997, in American Institute of Physics Conference Series, 510–+

McLeod, B. A., Bernstein, G. M., Rieke, M. J., Tollestrup, E. V., & Fazio, G. G. 1995, ApJS, 96, 117

Menci, N., Cavaliere, A., Fontana, A., Giallongo, E., Poli, F., & Vittorini, V. 2004, ApJ, 604, 12

Menci, N., Fontana, A., Giallongo, E., & Salimbeni, S. 2005, preprint (astro-ph/0506387)

Metcalfe, N., Shanks, T., Campos, A., Fong, R., & Gardner, J. P. 1996, Nature, 383, 236

Mobasher, B., Sharples, R. M., & Ellis, R. S. 1993, MNRAS, 263, 560

Mobasher, B. et al. 2004, ApJ, 600, L167

Motohara, K. et al. 2002, PASJ, 54, 315

Moustakas, L. A., Davis, M., Graham, J. R., Silk, J., Peterson, B. A., & Yoshii, Y. 1997, ApJ, 475, 445

Nagamine, K., Cen, R., Hernquist, L., Ostriker, J. P., & Springel, V. 2004, ApJ, 610, 45

Nagashima, M. & Yoshii, Y. 2004, ApJ, 610, 23

Oke, J. B. et al. 1995, PASP, 107, 375

Papovich, C., Dickinson, M., & Ferguson, H. C. 2001, ApJ, 559, 620

Papovich, C., Giavalisco, M., Dickinson, M., Conselice, C. J., & Ferguson, H. C. 2003, ApJ, 598, 827

Papovich, C. et al. 2005, preprint (astro-ph/0511289)

Patton, D. R., Carlberg, R. G., Marzke, R. O., Pritchet, C. J., da Costa, L. N., & Pellegrini, P. S. 2000, ApJ, 536, 153

Patton, D. R., Pritchet, C. J., Yee, H. K. C., Ellingson, E., & Carlberg, R. G. 1997, ApJ, 475, 29

Patton, D. R. et al. 2002, ApJ, 565, 208

Pei, Y. C. & Fall, S. M. 1995, ApJ, 454, 69

Peng, C. Y., Ho, L. C., Impey, C. D., & Rix, H.-W. 2002, AJ, 124, 266

Persic, M. & Salucci, P. 1991, ApJ, 368, 60

Persson, S. E., Murphy, D. C., Krzeminski, W., Roth, M., & Rieke, M. J. 1998, AJ, 116, 2475

Peterson, B. A., Ellis, R. S., Efstathiou, G., Shanks, T., Bean, A. J., Fong, R., & Zen-Long, Z. 1986, MNRAS, 221, 233

Peterson, B. A., Ellis, R. S., Kibblewhite, E. J., Bridgeland, M. T., Hooley, T., & Horne, D. 1979, ApJ, 233, L109

Poggianti, B. M. 1997, A&AS, 122, 399

Press, W. H. & Schechter, P. 1974, ApJ, 187, 425

Ravindranath, S. et al. 2004, ApJ, 604, L9

Reddy, N. A. et al. 2005, preprint (astro-ph/0507264)

Rees, M. J. & Ostriker, J. P. 1977, MNRAS, 179, 541

Riess, A. G. et al. 1998, AJ, 116, 1009

Rix, H.-W. et al. 2004, ApJS, 152, 163

Roche, P. F. et al. 2003, in Instrument Design and Performance for Optical/Infrared Ground-based Telescopes. Edited by Iye, Masanori; Moorwood, Alan F. M. Proceedings of the SPIE, Volume 4841, pp. 901-912 (2003)., 901–912

Rudnick, G. et al. 2003, ApJ, 599, 847

Sandage, A. 1961, ApJ, 134, 916

Saracco, P., D'Odorico, S., Moorwood, A., Buzzoni, A., Cuby, J.-G., & Lidman, C. 1999, A&A, 349, 751

Saracco, P., Iovino, A., Garilli, B., Maccagni, D., & Chincarini, G. 1997, AJ, 114, 887

Sawicki, M. J., Lin, H., & Yee, H. K. C. 1997, AJ, 113, 1

Scannapieco, E., Silk, J., & Bouwens, R. 2005, preprint (astro-ph/0511116)

Schlegel, D. J., Finkbeiner, D. P., & Davis, M. 1998, ApJ, 500, 525

Schmidt, M. 1968, ApJ, 151, 393

Shapley, A. E., Steidel, C. C., Erb, D. K., Reddy, N. A., Adelberger, K. L., Pettini, M., Barmby, P., & Huang, J. 2005, ApJ, 626, 698

Silk, J. 1977, ApJ, 211, 638

Silk, J. & Rees, M. J. 1998, A&A, 331, L1

Simard, L. et al. 2002, ApJS, 142, 1

Sivia, D. S. 1996, Data Analysis: a Bayesian Tutorial (Oxford University Press)

Smith, R. 1982, The Expanding Universe (London: Cambridge University Press)

Sofue, Y. & Rubin, V. 2001, ARA&A, 39, 137

Somerville, R. S., Lee, K., Ferguson, H. C., Gardner, J. P., Moustakas, L. A., & Giavalisco, M. 2004, ApJ, 600, L171

Somerville, R. S., Primack, J. R., & Faber, S. M. 2001, MNRAS, 320, 504

Spergel, D. N. et al. 2003, ApJS, 148, 175

Springel, V., Di Matteo, T., & Hernquist, L. 2005a, ApJ, 620, L79

—. 2005b, MNRAS, 361, 776

Springel, V. et al. 2005c, Nature, 435, 629

Steidel, C. C., Adelberger, K. L., Giavalisco, M., Dickinson, M., & Pettini, M. 1999, ApJ, 519, 1

Steidel, C. C., Giavalisco, M., Pettini, M., Dickinson, M., & Adelberger, K. L. 1996, ApJ, 462, L17+

Steinmetz, M. & Navarro, J. F. 1999, ApJ, 513, 555

Sullivan, M., Treyer, M. A., Ellis, R. S., & Mobasher, B. 2004, MNRAS, 350, 21

Tinsley, B. M. 1972, A&A, 20, 383

Tonry, J. & Davis, M. 1979, AJ, 84, 1511

Toomre, A. 1977, in Evolution of Galaxies and Stellar Populations, 401–+

Tran, K.-V. H., van Dokkum, P., Franx, M., Illingworth, G. D., Kelson, D. D., & Schreiber, N. M. F. 2005, ApJ, 627, L25

Treu, T., Ellis, R. S., Liao, T. X., & van Dokkum, P. G. 2005a, ApJ, 622, L5

Treu, T., Ellis, R. S., Liao, T. X., van Dokkum, P. G., Tozzi, P., Coil, A., Newman, J., Cooper, M. C., & Davis, M. 2005b, ApJ, 633, 174

Tully, R. B. & Fisher, J. R. 1977, A&A, 54, 661

Tully, R. B., Pierce, M. J., Huang, J.-S., Saunders, W., Verheijen, M. A. W., & Witchalls, P. L. 1998, AJ, 115, 2264

Turner, E. L. 1980, in IAU Symp. 92: Objects of High Redshift, 71–+

Tyson, J. A. 1988, AJ, 96, 1

Tyson, J. A. & Jarvis, J. F. 1979, ApJ, 230, L153

van den Bosch, F. C. 2002, MNRAS, 332, 456

van der Wel, A., Franx, M., van Dokkum, P. G., Rix, H. ., Illingworth, G. D., & Rosati, P. 2005, preprint (astro-ph/0502228)

van Dokkum, P. G. 2005, preprint (astro-ph/0506661)

van Dokkum, P. G., Franx, M., Fabricant, D., Illingworth, G. D., & Kelson, D. D. 2000, ApJ, 541, 95

van Dokkum, P. G. et al. 2006, ApJ, 638, L59

Vandame, B. et al. 2001, preprint (astro-ph/0102300)

Verheijen, M. A. W. 2001, ApJ, 563, 694

Vogt, N. P., Forbes, D. A., Phillips, A. C., Gronwall, C., Faber, S. M., Illingworth, G. D., & Koo, D. C. 1996, ApJ, 465, L15+

Vogt, N. P. et al. 1997, ApJ, 479, L121+

—. 2005, ApJS, 159, 41

Weiner, B. J. et al. 2005, ApJ, 620, 595

White, R. E., Keel, W. C., & Conselice, C. J. 2000, ApJ, 542, 761

White, S. D. M. & Frenk, C. S. 1991, ApJ, 379, 52

White, S. D. M. & Rees, M. J. 1978, MNRAS, 183, 341

Williams, R. E. et al. 1996, AJ, 112, 1335

Willmer, C. N. A. 1997, AJ, 114, 898

Willmer, C. N. A. et al. 2005, preprint (astro-ph/0506041)

Wilson, G., Cowie, L. L., Barger, A. J., & Burke, D. J. 2002, AJ, 124, 1258

Wilson, J. C. et al. 2003, in Instrument Design and Performance for Optical/Infrared Ground-based Telescopes. Edited by Iye, Masanori; Moorwood, Alan F. M. Proceedings of the SPIE, Volume 4841, pp. 451-458 (2003)., 451–458

Windhorst, R. A. et al. 2002, ApJS, 143, 113

Wirth, G. D. et al. 2004, AJ, 127, 3121

Wolf, C., Meisenheimer, K., Rix, H.-W., Borch, A., Dye, S., & Kleinheinrich, M. 2003, A&A, 401, 73

Wolf, C. et al. 2004, A&A, 421, 913

Yang, X., Mo, H. J., & van den Bosch, F. C. 2003, MNRAS, 339, 1057

Yee, H. K. C. & Ellingson, E. 1995, ApJ, 445, 37

Ziegler, B. L. et al. 2002, ApJ, 564, L69